UNIVERSITY OF CALIFORNIA

Los Angeles

Fluid-Particle and Fluid-Structure Interactions in Inertial Microfluidics

A dissertation submitted in partial satisfaction of the

requirements for the degree Doctor of Philosophy

in Biomedical Engineering

by

Hamed Amini

2012

ABSTRACT OF THE DISSERTATION

Fluid-Particle and Fluid-Structure Interactions in Inertial Microfluidics

by

Hamed Amini

Doctor of Philosophy in Biomedical Engineering

University of California, Los Angeles, 2012

Professor Dino Di Carlo, Chair

Due to the potential to miniaturize, integrate and automate sample preparation and analysis, lab-on-chips have witnessed a massive growth in research and development in the past two decades. The ability to accurately control and manipulate particles and fluid flow in microsystems is one of the main challenges of microfluidics to reach these goals. Inertial microfluidics, which exploits the flow non-linearities induced in finite Reynolds number flow regime, has been studied and employed as a platform for passive and high-throughput control of particles in microchannels in recent years. However, due to the complexity of the fluid dynamics associated with these systems much of the rich underlying physics is yet to be understood. This dissertation unravels parts of the unexplored physical phenomena occurring in inertial flow regime and reports new strategies for controlling and manipulating fluid flow and microparticles. We first provide a theoretical background of the underlying physics of non-linear microfluidic systems,

especially inertial microfluidics. We then discuss the effects of particles on fluid in an inertial flow regime. The novel phenomenon of "*particle-induced convection*" is introduced where moving particles act as dynamic sites to induce net secondary flows inside microchannels which can be used for heat and mass transfer. Finally, we introduce a novel technique to induce strong net secondary flows by positioning simple microstructures (i.e. cylindrical pillars) inside straight microchannels. We make use of the *inertial flow deformations* associated with the flow around a library of single cylindrical pillars at eight positions within a microfluidic channel as fundamental operations for more complex fluid manipulations. Since transformations for each basic pillar location provide a deterministic mapping of fluid elements from upstream to downstream of a pillar, we can sequentially arrange pillars to apply the associated nested maps and therefore program complex fluid structures without additional numerical simulation, inducing order rather than chaos in microflows. Consequently, functions composed of multiple pillars can be hierarchically assembled to execute practical programs. To show the range of capabilities we demonstrate programs to sculpt the cross-sectional shape of a stream into complex geometries (such as various concavity polygons, closed rings, and inclined lines), move and split a fluid stream, transfer particles from a stream, and separate particles by size.

This dissertation of Hamed Amini is approved.

Benjamin M. Wu

Jeffrey D. Eldredge

Eric Pei-Yu Chiou

Dean Ho

Dino Di Carlo, Committee Chair

University of California, Los Angeles

2012

DEDICATION

Humbly dedicated to:

Sadraddin and Forough

Ali, Hamid, Mahmoud and Yeganeh

TABLE OF CONTENTS

ACKNOWLEDGEMENTS

Chapter 1

Inertial microfluidics physics is a version of work in progress for publication by Hamed Amini, Wonhee Lee and Dino Di Carlo. Professor Dino Di Carlo is the principal investigator of this work.

Chapter 2

Intrinsic particle-induced lateral transport in microchannels has been reprinted with minor adaptations with permission from (Amini H, Sollier E, Weaver WM, Di Carlo D (2012) Intrinsic particle-induced lateral transport in microchannels. *Proceedings of National Academy of Sciences USA* 109 (29): 11593-11598.) Copyright (2012) National Academy of Sciences, USA. H.A. and D.D. designed research; H.A., E.S., and W.M.W. performed research; H.A., E.S., and D.D. analyzed data; and H.A., E.S., and D.D. wrote the paper. Professor Dino Di Carlo is the principal investigator of this work. This project received funds from National Science Foundation.

Chapter 3

Programming fluid flow using sequenced microstructures is a version of work in progress for publication by Hamed Amini, Mahdokht Masaeli, Elodie Sollier, Yu Xie, Baskar Ganapathysubramanian, Howard A. Stone and Dino Di Carlo. Professor Dino Di Carlo is the principal investigator of this work.

VITA

Education

M.Sc. in Mechanical Engineering **2008-2009**
University of California, Los Angeles
Specialization: Fluid Mechanics

B.Sc. in Mechanical Engineering **2004-2008**
Sharif University of Technology, Tehran, Iran
Project: Design and fabrication of a micro heat-pipe

Awards and Honors

- Recipient of the *Dean of Engineering Fellowship*, UCLA, 2009-2010
- Recipient of the travel grant for USNCTAM 2010
- Recipient of the *MAE Departmental Fellowship*, UCLA, 2008-2009
- Ranked 52nd in the National University Entrance Exam (***top 0.01%*** amongst more than half a million participants), Iran, 2004
- ***Bronze Medal*** in Iran's National Mathematical Olympiad, Iran, 2003

Publications

Journal Papers:

- **Amini H**, Masaeli M, Sollier E, Xie Y, Ganapathysubramanian B, Stone HA, Di Carlo D, Programming fluid flow using sequenced microstructures. *(in preparation)*

- **Amini H**, Lee W, Di Carlo D. Review: Inertial Microfluidics Physics *(in preparation)*

- **Amini H**, Sollier E, Weaver WM, Di Carlo D. Spinning convection: intrinsic particle-induced transport in microchannels. ***Proceedings of the National Academy of Sciences USA*** 2012

- Masaeli M and Sollier E, **Amini H**, Mao W, Camacho K, Doshi N, Mitragotri S, Alexeev A, Di Carlo D. Continuous inertial focusing and separation of particles by shape. *(to be published in Physical Review X)*

- Lee W, **Amini H**, Stone HA, Di Carlo D. Dynamic self-assembly and control of microfluidic particle crystals. ***Proceedings of the National Academy of Sciences USA*** 2010

- Gossett DR, Weaver WM, Mach AJ, Hur SC, Tse HTK, Lee W, **Amini H**, Di Carlo D. Review: Label-free Cell Separation and Sorting in Microfluidic Systems. ***Analytical and Bioanalytical Chemistry*** 2010

Conference Proceedings:

- Amini H, Masaeli M, Di Carlo D. Programming Fluid Flow with Microstructures. **Podium Presentation. APS-DFD 2011**. Baltimore, MD

- Amini H, Masaeli M, Di Carlo D. Pillar-induced Mixing in Microchannels. **Poster Presentation. BMES 2011**. Hartford, CT

- Amini H, Masaeli M, Di Carlo D. Controlling Flow In Microchannels Using Programmed Pillars. **Poster Presentation. MicroTAS 2011**. Seattle, WA

- Amini H, Sollier E, Di Carlo D. Spinning Convection: Particle-induced Secondary Flow in Straight Microchannels. **Podium Presentation. APS-DFD 2010**. Long Beach, CA

- Sollier E, Amini H, Achard JL, Di Carlo D. Modification of inertial focusing position by the restriction effect. **Podium Presentation. APS-DFD 2010.** Long Beach, CA

- Lee W, Amini H, Stone HA, Di Carlo D. Inertially Stabilized Microfluidic Crystals: Self-assembly and Spatial Frequency Tuning. **Podium Presentation. APS DFD 2010**. Long Beach, CA

- Amini H, Sollier E, Di Carlo D. Simple particle-induced transverse mass transport at high flow rates. **Podium Presentation. BMES 2010**. Austin, TX

- Amini H, Sollier E, Di Carlo D. Intrinsic bioparticle-induced solution transfer for on-chip mixing and sample preparation. **Poster Presentation. MicroTAS 2010.** Groningen, The Netherlands. October, 2010.

- Amini H, Di Carlo D. Enhancement of micro-mixing utilizing inertial flows around microspheres in channel flow. **Podium Presentation. USNCTAM 2010, State College, PA**

Patents

- **Amini H**, Sollier E, Di Carlo D. Enhancement of Mass Transfer in Channel Flow (Provisional Patent, No. 61/540,990)

- **Amini H**, Sollier E, Di Carlo D. Programming Fluid Flow with Microstructures (Provisional Patent, No. 61/541,953)

Chapter 1

Inertial microfluidics physics

Abstract

Microfluidics has experienced massive growth in the past two decades, and especially with advances in rapid prototyping researchers have explored a multitude of channel structures, fluid and particle mixtures, and integration with electrical and optical systems towards solving problems in healthcare, biological and chemical analysis, materials synthesis, and other emerging areas that can benefit from the scale, automation, or the unique physics of these systems. Inertial microfluidics, which relies on the unconventional use of fluid inertia in microfluidic platforms, is one of the emerging fields that makes use of unique physical phenomena that are accessible in microscale patterned channels. Channel shapes that focus, concentrate, order, separate, transfer, and mix particles and fluids have been demonstrated, however physical underpinnings guiding these channel designs have been limited and much of the development has been based on experimentally-derived intuition. Here we aim to provide a deeper understanding of mechanisms and underlying physics in these systems which can lead to more effective and reliable designs with less iteration. To place the inertial effects into context we also discuss related fluid-induced forces present in particulate flows including forces due to non-Newtonian fluids, particle asymmetry, and particle deformability. We then highlight the inverse situation and describe the effect of the suspended particles acting on the fluid in a channel flow. Finally, we discuss the importance of structured channels, i.e. channels with boundary conditions that vary in the streamwise direction, and their potential as a means to achieve unprecedented three-dimensional

control over fluid and particles in microchannels. Ultimately, we hope that an improved fundamental and quantitative understanding of inertial fluid dynamic effects can lead to unprecedented capabilities to program fluid and particle flow towards automation of biomedicine, materials synthesis, and chemical process control.

Introduction

The belief that all practically achievable and useful flows in microfluidic systems operate not only in the laminar flow regime but also in a Stokes flow regime ($Re \rightarrow 0$, $Re=\rho UH/\mu$ where U is the average velocity, H is the channel dimension and ρ and μ are fluid density and viscosity, respectively) was widespread in the microfluidic community until recent years (1). Following this belief, the inertia of the fluid is completely ignored in microfluidic platforms and contributions of fluid momentum are omitted from the Navier-Stokes equations resulting in a linear, and thus time-reversible, equation of motion for Newtonian fluids. However, the importance of intermediate range flow ($1 \lesssim Re \lesssim 100$) was emphasized recently (2, 3) in which nonlinear and irreversible motions are observed for fluid and particles in microchannels. This regime, in which both the inertia and viscosity of the fluid are finite, still lies within the realm of laminar flow ($Re \ll 2300$) which has a deterministic nature. It should be noted that the necessity for large velocity gradients to manipulate particles and fluids in inertial microfluidic platforms has prevented observation of similar behaviors in larger channels filled with fluids with viscosity similar to water at room temperature and pressure. We show this with an example: in a typical microchannel with a size of 100 μm with water as a working fluid ($\rho \sim 1000$ kg/m^3 and $\mu \sim 0.001$ Pa.s) a flow rate of 150 μL/min results in a maximum velocity of ~0.375 m/s, which is achieved at the channel center only 50 μm away from the wall, and corresponds to $Re \sim 25$ (a common set of easily achievable conditions in inertial microfluidics). If one were to scale up all the elements to achieve a similar velocity gradient in a channel that is only 1 cm in diameter (i.e. 100x wider) the required maximum velocity would be ~37.5 m/s, which corresponds to $Re \sim 250{,}000$! Even though such a flow rate is achievable since the pressure to drive such a flow actually decreases,

the flow would be highly chaotic and turbulent ($Re \gg 2300$) not allowing the precise quantitative control achievable with laminar flow.

In this chapter we aim to revisit the fluid physics in such microscale systems operating in a laminar but finite *Re* regime and demonstrate how integration of the physical phenomena occurring in this scale introduces a quantitative framework to passively control and manipulate fluid and particles in channels, similar to the framework semiconductor physics provided for controlling the flow of electrons that revolutionized electronics.

In chapter 1 we first discuss straight microchannels and introduce the different mechanisms that can be used to cause lateral migration and control of particles due to fluid inertia, fluid viscoelasticity, particle shape and particle deformability. We also review the inter-particle interactions in these systems (which connect with chapter 2 where we will discuss how particles can interestingly be used as "dynamic/moving structures" to manipulate fluid in straight microchannels). We then argue how channels can be modified to control the fluid and particles flowing inside. A straight channel with no irregularities can only be used to manipulate particles, but not fluid. However, "structured" channels (i.e. channels with irregular geometry in a streamwise direction) can be used to manipulate both particles and fluid. Any deviation from a straight channel can be considered a structured channel, for instance the presence of curvature in a channel, or grooves on the walls of the channel or introduction of pillars and obstacles in the channel (latter is discussed in chapter 3). We discuss how any geometrical deviation can induce *net* secondary flows (i.e. net recirculation perpendicular to the main flow direction) and present the different types of fluid/particle manipulation that can be achieved by engineering channel

irregularities and structures. We discuss the importance of inertia in each of these cases and show how the two regimes, namely Stokes and inertial flow, can be used to achieve unprecedented control over fluid and particles in a completely passive manner. Throughout, we emphasize the differences between inertial and Stokes flow and connect the reversibility associated with Stokes flow to the "mirror symmetry time reversal" theorem (4), which leads to the conclusions that with fore-aft asymmetries even Stokes flow can cause net twisting of fluid streamlines while inertial flow can inherently lead to such flow deformations even in symmetric geometries.

i. PARTICLES IN A STRAIGHT CHANNEL

A straight channel with a square/rectangular cross-section is the simplest form of conduit that can be used in microfluidics (although the concepts introduced in this section can be generalized to other cross-sections and geometry scales as well). Introduction of different forms of nonlinearity into these simple systems can produce lift forces (forces directed perpendicular to the main flow) that can be used to manipulate flowing particles.

a) Inertial migration and focusing

In order to achieve spatial control of particles in microchannels, a mechanism of lateral migration is required; a manipulation tool that can be used to introduce order into an otherwise randomly distributed set of particles in a microflow. Such a behavior was first reported by Segre and Silberberg (5) where they observed that randomly distributed millimeter-sized particles migrated laterally to unexpectedly focus on an annulus with a radius ~0.6 times the radius from the center of the one-centimeter-diameter pipe. The lateral motion was unexpected at the time and proved the existence of some form of lift force acting on these particles. Additionally, since

the particles reach a stable dynamic equilibrium at the annulus, there are possibly two (or more) types of opposing lift forces acting on the particles in the Poiseuille flow. Later theoretical analyses suggested (6, 7) that there are two opposing forces present: 1) the wall induced lift force (or "wall effect" lift force), due to the interaction between the particle and the adjacent wall, which directs the particle away from the wall and 2) the shear gradient induced lift force, due to the curvature of the velocity profile, which directs the particle away from the channel center (Figure 1-1.A). Note that the inherently present gradient of the shear rate (second derivative of velocity) in Poiseuille flow (which is due to its natural parabolic shape) plays an important role as the origin of the shear gradient lift force in forming stable dynamic equilibrium positions. An account of the development of the theory describing the lift forces is presented in a review on the topic (3). The current understanding suggests that, for a finite-size particle of diameter a (i.e. a/H is of the order of 1), the net lift acting on the particle scales as $F_L \propto \rho U^2 a^3/H$ near the channel center and as $F_L \propto \rho U^2 a^6/H^4$ near the channel wall, with a dimensionless lift coefficient f_L that is a function of Re and x/H (8). As a result of these lift forces, for a particle Reynolds number, R_p of order of equal or larger than 1 (where $R_p = Re(a/H)^2 = \rho U a^2/\mu H$) the randomly dispersed particles in a square microchannel inertially focus to four symmetric equilibrium positions near the center of each channel wall and, in agreement with Segre and Silberberg's observation, ~0.6H away from the channel center (Figure 1-1.B) as confirmed experimentally (2). Here R_p is the particle Reynolds number, a measure of the ratio of inertial to viscous forces of the velocity difference across the particle length scale and contrasts with a particle Reynolds number dependent only on length dimensions of the particle in an unbounded flow. Note that the velocity scale is therefore dependent on the shear rate, an important parameter in achieving appreciable lift as discussed previously. The finite element solutions also provide a clear map of the lift

imposed on the particle in these channels which is in agreement with experimental and theoretical work (Figure 1-1.B).

Interestingly, when particles are introduced into a channel with rectangular cross-section (without the four-fold symmetry of a square) the number of favored dynamic equilibrium positions is decreased to two, located near the wider faces of the channel (Figure 1-1.C). Numerical solutions show that the force field present in the channel results in a set of stable equilibrium positions and saddle points in the channel (9). To understand how this can lead to two dominant equilibriums, we can think of releasing a particle at a point in a quadrant of the channel and assessing the probability of it approaching either of the two reachable equilibrium positions (i.e. on the long and the short face). In such a cross-section (Figure 1-1.C) the shear gradient lift force, which is dominant anywhere away from the walls, is stronger in the z-direction but much weaker in the y-direction (due to the blunted velocity profile in the y-direction). Therefore, a particle that is randomly released in this channel has a greater chance of being pushed away from channel's y-centerline (blue). Consequently, the particle will approach the long channel face (green line) in the z-direction first and then due to dominant wall-effect lift is directed towards the centerline (red line) in the y-direction until it settles at its stable equilibrium position (Figure 1-1.C). Overall, for a moderate *Re* the lift forces in this cross-section lead to limited particle paths that arrive at the other equilibrium position at the short channel face. Significant biasing to two focusing positions can be observed for even slight deviations from square geometries, for example, aspect ratios of 3:2.

At higher *Re* the equilibrium positions in square and rectangular channels tend to shift slightly towards the walls (Figure 1-1.D). This also can be explained by taking the two competing lift forces into account. It is clear that both the wall effect lift and the shear gradient lift increase with increasing velocity or *Re*. However, the increase in shear gradient lift is relatively larger for a given increase in *Re* (6, 9). Therefore, increasing *Re* causes the shear gradient lift to become more dominant and, consequently, the particle equilibrium positions shift closer to the wall. A similar behavior occurs in rectangular channels, in which the two previously unstable positions on the short faces now collect additional particles, as the wall effect becomes less dominant in directing particles away along the long face, leading to an increase in the total number of focusing positions to four (Figure 1-1.D). Therefore, the distribution of lift forces within the channel is altered such that the competing y-directed shear gradient lift force can direct particles into the previously unstable/unreachable equilibrium position.

It has also been shown that both the location and the number of focusing positions depend on the number of particles per unit length along the channel (10), such that at high length fractions, i.e. $\varphi > \sim 75\%$ (number of particle diameters per channel length) (3) multiple streams are observed across the channel. At these increased concentrations, if the particles are to occupy two to four focused streams they are forced to stay in close proximity to each other. In this case, there will be a large increase in particle-particle hydrodynamic interactions which have been shown to be important once particles are within a short distance of one another (11). As a result, a portion of the particles are pushed out of the lift-specified focusing streams, and form new nearby focusing streams. These particle-particle interactions act as one limit on achieving precision focusing of all particles in a channel.

Despite multiple works discussing the lift forces on particles in channel flow (6, 7, 12), there is no simple intuitive explanation for the origins of inertial lift. In their theoretical work on the lift forces exerted on infinitely small particles, Leal and Ho (7) describe that the direction of this force depends on the direction of both the shear rate and its gradient, and arises from the interaction of the local disturbance velocity field with both the shear rate and its gradient. For instance, in a Poiseuille flow in a rectangular channel the shear rate is always positive and its gradient negative as an inherent characteristic of the velocity profile (Figure 1-1.E). Therefore, the shear gradient induced lift always is directed towards the wall. However, if the suspension was to flow through a channel with a more complex cross-sectional shape, such as the one shown in Figure 1-1.E (bottom), the velocity profile correspondingly becomes more complex and even possesses an inflection point. In this case, the direction of shear rate and shear rate gradient could alter across the channel width which, based on Leal and Ho's analysis, leads to shear gradient lift forces that change signs across the channel. Numerical predictions and experimental results with additional channel shapes will likely clarify the importance of this effect, and have the potential to open up a whole new set of design tools for particle manipulation and control based on velocity field sculpting.

Considering shear-gradient lift alone we have previously presented an expression based on the cross-streamline motion of particles (3) that proscribes a channel length required for particles to reach lateral equilibrium positions (L_f) in rectangular channels $L_f = \frac{\pi \mu H^2}{\rho U_m a^2 f_L}$, where μ and ρ are the fluid viscosity and density, U_m is the maximum channel velocity (~$1.5U_{avg}$) and a is the

particle diameter. The average f_L is about 0.02-0.05 for aspect ratios (*H/W*) from 2 to 0.5 where *H* is the channel size in the direction of particle migration.

Applications of inertial focusing. The simplicity of the phenomenon suggests its ability to impact many applications. For instance, since there are no extra force fields or devices required (only the channel itself is needed for alignment of particles), this method can be easily parallelized by branching off many channels from a single inlet and arraying them in close proximity. This leads to extremely high throughput particle focusing (Figure 1-2.A) which has been used for high-throughput sheath-less flow cytometry (13). This may be particularly useful in reducing the size and cost of operation of flow cytometers, which normally require a large bulk of aqueous sheath fluid to pinch cell streams prior to optical interrogation. Remaining challenges to overcome to speed adoption for this application include focusing of cell sized particles in channels with larger channel dimensions (currently precise focusing requires channels with dimensions approximately less than 5-7 times particle diameters). Achieving this would require less frequent replacement of the focusing chip and lower pressure pumping systems. Going beyond the use of straight rectangular channels, as discussed below, can aid in this direction.

Inertial focusing in straight channels has also been used to separate pathogenic bacteria cells from diluted blood (Figure 1-2.B) (14). In this simple design, the larger blood cells become focused in a shorter channel length (following the aforementioned equation), while the smaller bacteria are less affected by the inertial lift forces and remain dispersed throughout the channel (due to their smaller sizes). Through a gradual expansion of the channel width, the focused cells

are then moved to a position closer to the side walls (while maintaining their focused state), leaving a large portion of the channel cross-section free of blood cells. The focused streams are then captured with side outlets while the remaining fluid that contains most of the bacteria is captured separately. The straight channel design allows for radial parallelization of the system which can process up to 240 mL/h with a throughput of 400 million cells/min with >80% bacteria removal from blood after two passes. As with focusing, interparticle interactions at high blood cell concentrations can prevent precise focusing and reduce the accuracy of separation, such that separations using inertial lift forces operate best in semi-dilute solutions with length fractions below ~ 50%.

Lateral inertial migration across laminar co-flowing streams has also been used to achieve fast fluid exchange around cells and particles (9). This technique relies on the intelligent use of the presence of two (rather than four) stable equilibrium positions in high aspect ratio channels. Here, the particle suspension is co-flowed with an exchange solution that has a higher flow rate (~2x) into a high aspect ratio channel (i.e. *W/H* greater than 1). Once in this main channel, particles start to migrate towards new *stable* equilibrium positions in the center of the new channel, which due to the asymmetry in the rates of the co-flows is located along streamlines occupied by the exchange solution (Figure 1-2.C). Consequently, with an appropriate outlet design the particles can be captured in the exchange solution with high purity, high yield and at a high rate (which is a general characteristic of inertial microfluidic platforms). The high rate necessary for operation is not ideal for exchanging solution around one or a few cells from a rare sample, which would require much more delicate instrumentation, but is ideal for applications

requiring millisecond solution exchange around hundreds to thousands of cells or particles/second, with the capability of downstream inline analysis.

High throughput is a primary advantage of inertial microfluidic platforms which makes them highly compatible with other high-speed platforms. For instance, in a recent development, inertially focused cancer and blood cells were analyzed by a novel line scan-base high-speed imaging technology (serial time-encoded amplified microscopy - STEAM) and achieved nearly 100,000 particle/s real-time image-based screening (compared to the state of the art ~1,000 particle/s) (15) (Figure 1-2.D). In this system, particles, including blood cells and budding yeast, are first ordered and focused in a straight inertial microfluidic channel fabricated in thermosetting polyester (TPE) (16), to prevent fluctuations in channel dimensions in softer polymer channels that affect the optical signal quality, and achieve higher pressure flows without device failure.

Inertial focusing can be used in combination with channel structures that induce net secondary flows in a channel. In the multi-orifice flow fractionation (MOFF) technology, inertial focusing is combined with the presence of multiple sudden expansion-contraction regions that lead to hydrodynamic cross-stream motion of particles (17). Jung *et al.* further developed multistage MOFF devices for continuous size-based separation of spherical particles (Figure 1-2.E) (18) and used the technique combined with dielectrophoresis to separate rare breast cancer cells from blood (19). Han *et al.* combined inertial focusing with a pinched flow to separate larger rare cells in blood at a high throughput (Figure 1-2.F) (20). Limitations of this approach, like other inertial focusing-based approaches, are that high cell concentrations prevent accurate separations.

Inertial focusing in concentrated particulate solutions is a useful frontier to study potentially providing solutions to address the challenge of focusing and separation of cell populations present in whole blood. Development of novel techniques and evaluation approaches that are better compatible with high cell concentrations has aided in this endeavor. For instance, conventional imaging techniques used for studying inertial focusing - including high-speed bright-field imaging and long exposure fluorescence imaging - are generally limited in complex fluids such as whole blood due to interference from the large numbers of red blood cells. In a recent study, Toner *et al.* applied particle trajectory analysis (PTA) as a means to observe inertial migration of particles in dilute and whole blood which led to uncovering a radical shift in focusing behavior of PC-3 prostate cancer cells in whole blood (21). As another example, a lot of the inertial microfluidics platforms operate at extremely high flow rates, which leads to very high pressure drops in these channels. In practice, the inability of Polydimethylsiloxane (PDMS)-based devices, which are the gold standard for rapid and cheap device fabrication, to withhold such high pressure drops acts as one of the limiting factors, especially in prototyping and research development. Therefore, the development of stiff material that can withstand higher pressure drops for rapid prototyping of microfluidic devices is important and could push the limits on both research and application fronts (16).

An understanding of inertial focusing of rigid spherical particles in straight rectangular channels provides a solid foundation for applications in focusing, separation, enrichment, and ordering of cells and particles. A more complete understanding of migration behavior for real-world

particles and applications requires additional knowledge of how fluid properties, particle shape and deformability, and channel structures contribute to overall motion.

b) Non-Newtonian fluids

In addition to finite-*Re* flow conditions, non-Newtonian fluids have long been known to cause lateral migration of single particles in a pressure-driven channel flow. The focusing positions for particles in a non-Newtonian flow depend on the rheological properties of the fluid. We will briefly touch upon the visco-elastic lift force that can be used (or must be taken into account for some fluids) to manipulate particles in inertial microfluidic systems.

Particles migrate typically towards the center or the wall of a pressure driven channel flow, depending on rheological properties of fluid (i.e. shear thinning or shear thickening) and the channel blockage ratio (α=*a/H*) (22, 23). Ho and Leal predicted that a non-uniform normal stress distribution in a second-order fluid results in lateral particle migration (24). A second order fluid is defined to have stresses in the fluid that are not linearly dependent on the shear rate – as in a Newtonian fluid. Particles migrate in the direction of decreasing absolute shear rate, which is towards the center for a Poiseuille flow.

The non-dimensional Weissenberg number (*Wi*) is often used to characterize the visco-elasticity of a fluid and is the ratio of fluid/polymer relaxation time (λ) to shear rate time which is the characteristic time of the channel flow (τ_c) (1):

$$Wi = \frac{\lambda}{\tau_c} = \lambda \frac{2U_{avg}}{w} = \frac{2\lambda Q}{hw^2}$$

τ_c is approximately equal to the inverse of the average (or characteristic) shear rate (γ_c). Average shear rate in a rectangular channel is $\frac{U_{avg}}{w/2}$ where U_{avg} is the average velocity and w is the channel width.

The Elasticity number, *El* is the ratio between *Wi* and *Re*, and indicates the relative strength of elastic forces to inertial effects.

$$El = \frac{Wi}{Re} = \frac{\lambda \mu_c (W + H)}{\rho W^2 H}$$

μ_c is characteristic viscosity or average viscosity of the fluid.

As both *Wi* and *Re* are proportional to the flow rate, *El* becomes independent of the flow rate. This assumption would be valid if the viscosity is constant. However in many cases viscosity is not constant due to shear thinning and thickening.

In recent years, experimental and numerical studies have demonstrated the ability to apply visco-elasticity-induced forces for particle focusing and separation (25–30). These forces have also been combined with inertial lift forces to enable higher throughput manipulations of particles.

In a circular tube, (e.g. glass capillary (29)) particles in visco-elastic flow migrate toward the center of the tube for a wide range of *Wi* and α, these parameters can be tuned to achieve a bi-stable condition where particles migrate both towards the channel center and the walls depending on initial position of the particle. In this study, *Re* was sufficiently small that inertial

effects could be ignored, which also limits applications to small volume operations. With typical microfluidic channels of rectangular cross-section, elastic force focuses particles to the center and the four corners instead (28, 30). The addition of inertial lift forces that focus particles near the walls (Figure 1-3. A) can lead to a reduction in the number of focusing positions. By controlling flow rate, inertial lift forces and visco-elastic lift forces can be carefully balanced to achieve an Elasticity number that yields a single line of focusing along the channel center-line (Figure 1-3.A and B) (28). Single line focusing without external field or sheath fluid has great advantages in application areas such as miniaturization of flow cytometers. It is also possible to separate particles of different sizes using the fact that lift forces (inertial and visco-elastic) are proportional to the particle size (25). The small particles (2.4 μm) are relatively less focused and the larger particles are tightly focused at the center of the channel. Similarly, 1 μm and 5 μm particles were separated in a microfluidic channel by introducing particles (Figure 1-3.B and C) in a side channel and relying on differences in the migration rate towards the center of the channel (a kinetic separation (31)).

c) <u>Shaped particles (with or without fluid inertia)</u>

A sphere is the ideal shape for a particle in many cases and studies owing to its ultimate symmetry and lack of singularities, which lead to mathematical simplicity. Therefore, in a large portion of the work describing particulate flows (theoretical, numerical and experimental), a sphere has been used as a simplified case, an approximation. However, in a large portion of real systems non-spherical particles exist. For instance, a human red blood cell (RBC) adopts a discoid shape in the body, far away from being a sphere. Shape represents an important factor to specifically identify a bioparticle (32), including bacteria, viral particles, budding yeast, and

marine micro-organisms. Synthesized barcoded particles represent another example of particles that would be helpful to operate on and manipulate (33–35). Therefore, it is important to improve our understanding of systems that contain shaped particles and the corresponding lift forces and dynamics of these particles. One of the classic works in this area was the investigation of the motion of ellipsoidal particles in unbounded shear flow in a Stokes flow regime by Jeffery (36) which led to the discovery of the so-called "Jeffery orbit" in which a particle rotates in a closed repeating cycle around any of an infinite set of axes that depend on its initial orientation (37). Here we discuss how particle shape and fluid inertia combined can affect particle motion, focusing and separation dynamics in microchannel systems.

An interesting point about shaped particles is that they can be subject to lift forces even in the absence of inertia (i.e. Stokes flow) which can be intuitively described via an exception to Bretherton's "mirror symmetry time reversal" theorem (MSTR theorem) (4). Simply put, the theorem indicates that if a sufficiently symmetric particle moves in a uni-directional viscous shear flow without inertia and we momentarily reverse time, the resulting configuration (in terms of the flow field, pressure field, forces, etc.) is mirror symmetric to another configuration of the particle that is 90 degrees rotated around the rotational axis defined by its Jeffery orbit. We will define what a "sufficiently symmetric" particle entails in the following discussion. This is due to the linearity of the Stokes equations, and a full proof can be found in Bretherton's paper (4). The MSTR theorem, can also apply to a channel flow in which a velocity gradient is also present leading to particle rotation (11).

For a rigid spherical particle, the MSTR theorem provides a proof that there can be no lift forces acting on the particle in Stokes flow for a simple channel (Figure 1-4.A). If we assume there is a net lift on the particle ($\overrightarrow{F_L}$), then due to the linearity of the equations of motion there is an opposite directed force ($\overrightarrow{F_L}' = -\overrightarrow{F_L}$) if we reverse the time. However, the initial and time-reserved configurations are exactly the same in every way (due to the fore-aft symmetry of the system). Therefore the two forces need to be equal ($\overrightarrow{F_L} = -\overrightarrow{F_L}$) which is only satisfied for $\overrightarrow{F_L} = 0$ Hence, there can be no lift on a spherical particle in Stokes flow through a channel.

If the particle has an ellipsoidal shape, the scenario is slightly different (Figure 1-4.B): an ellipsoidal particle follows an orbit similar to a Jeffery orbit (Figure 1-4.B.i). If time is reversed, the direction of the instantaneous lift force is also reversed (Figure 1-4.B.ii). The configuration that is mirror symmetric (Figure 1-4.B.iii), however, is in fact the 90° rotation of the original configuration. Therefore, instantaneous lift can possibly exist during the particle's rotational cycle. However, the lift force at any point has a complete counterpart during the cycle with opposite directed lift, thus there can be no *net* lift on the particle during a full orbit. This result requires that the particle is sufficiently symmetric, that is, the particle is mirror symmetric to a rotation around its rotational axis. Classes of shapes that can satisfy this condition include disks, cylinders, rectangular prisms, triangular prisms, and cones.

For a rotationally asymmetric particle, the MSTR theorem cannot be applied (Figure 1-4.C) and a net lift force is possible for a rotating particle. For example if we have an h-shaped particle in the channel (i) and we reverse time (ii), the mirror-symmetric configuration is impossible to achieve by any degree of rotation. Therefore, the MSTR theorem does not apply to such

asymmetric particles, and cannot be used to eliminate the possibility of a *net* lift force acting on the particle throughout its rotational cycle, even in Stokes flow.

Clearly, the rotational axis of the particle is important in defining the lift forces and subsequent motion of a particle, and this preferred rotational axis can be set due to the presence of fluid inertia. In Stokes flow we know that particles can occupy an infinite set of rotational axes that depend on initial conditions. This situation changes due to the presence of fluid inertia (38). The addition of inertia and channel confinement leads to the precession of particle orbits to a stable rotational axis in the parabolic flow. In a recent work, Hur *et al.* and Masaeli *et al.* used straight microchannels (Figure 1-4.D.i) to experimentally study the focusing behavior of multiple types of particles such as symmetric disks (Figure 1-4.D.ii), cylinders (Figure 1-4.Diii), ellipsoids, and asymmetric disks (Figure 1-4.D.iv) (39). Above a critical Reynolds number (Re~50) particles predominantly adopted preferred equilibrium positions and "tumbling" rotational axes. For particles symmetric about this rotational axis focusing position was found to be independent of cross-sectional shape and mainly depends on rotational diameter (D_{max}). During the tumbling motion, when the major axis rotates to be perpendicular to the wall, wall effect lift increases substantially due to the closer distance. As a result, the integrated wall effect (over time) on these particles is higher than that of spheres of the same volume. Interestingly, only the highly asymmetric h-shaped disk did not follow this trend and focused closer to the walls than expected for its D_{max}, in agreement with the MSTR theorem allowing an additional lift force acting on this rotationally asymmetric particle (Figure 1-4.E).

Shape-based differential focusing has potential applications, and has already been used to sort and separate budding yeast at the high rate of 1500 cells/s, an order of magnitude improvement from previous methods.

d) Deformable particles

In many studies of particulate systems, solid rigid particles are used as simple components to study system behavior. However, bioparticles such as cells and vesicles, or two-phase emulsion droplets are not rigid, but deformable. Importantly, deformability of particles can create nonlinearity in these systems which can lead to additional lift forces on these particles (40).

Different models are used to approximate complex bioparticles or more simple emulsions when studying their motion in flow. Three general models for approximating a deformable particle that is shown in this case to be in a shear flow include (Figure 1-5.A): i. An elastic solid particle (41): the whole particle is considered as a single solid body which can deform with a particular elastic constant. In this case, for the flowing particle to retain a steady-state shape it needs to constantly deform or "tank-tread" as it is rotating under the shear flow. ii. A deformable drop (40, 42): the particle is assumed to be a drop with fluid on the inside and a boundary that can slip under the driving flow. In this case, recirculation of fluid can occur inside the droplet due to the outer flow and the elasticity of the droplet is defined by its surface tension. iii. A deformable capsule (43–45): the inner fluid is covered by a deformable but solid shell with a specified elastic constant. The solid shell undergoes a tank-treading motion to maintain a steady-state deformed shape while fluid recirculation can occur inside the capsule.

These studies suggest that in a shear or Poiseuille flow, regardless of the approach to approximate deformability, there is a component of force perpendicular to the free-stream direction that causes the particle to migrate across undisturbed streamlines. This lateral migration is argued to be due to the shape-change of the particle and can occur even in the absence of inertia (41). This links with our discussion of shaped particles in which instantaneous lift can act on a particle in Stokes flow (Figure 1-4.B). The difference in this case is that the deformable particle in many cases does not tumble to occupy mirror symmetric configurations but rather can perform a tank-treading motion such that it maintains a steady-state shape as it flows downstream. Therefore, in contrast with a rigid elongated rotational symmetric particle, a deformable particle can have a *net* lift leading to its lateral migration.

Lateral migration of deformable particles is reported to be due to a nonlinearity caused by the matching of velocities and stresses at the deformable particle/droplet interface (46) – that is the velocity field impacts the deformed shape which in turn impacts the velocity field. In general this means that the magnitude of lateral drift is related to the deformed shape of the particle. For droplets with a surface tension, σ, the Weber number, $We = \frac{\rho_{ex} U_{max}^2 \, a}{\sigma}$ (inertial stress *vs.* surface tension), or capillary number, $Ca = \frac{\mu_{ex} U_{max} \, a}{\sigma W}$ (viscous stress *vs.* surface tension) provides a dimensionless parameter that characterizes the relative deformation for a droplet. Viscosity ratio, $\lambda = \mu_{in}/\mu_{ex}$, is another important parameter in defining the shape of the deformed drop. By measuring the shifting balance between deformability-induced lift and inertial lift, Hur *et al.* experimentally demonstrated that deformability-induced lift increased with increasing drop deformation. Droplets shifted towards the channel center as lambda decreases from 1000 to 5 cSt (i.e. more deformable particle). Counter-intuitively, as the viscosity ratio decreased below 5

cSt, the focusing position shifted back towards the wall (Figure 1-5.C), in agreement with theoretical predictions (46) that may also implicate strong internal circulations within a drop affecting lift. Similar to droplets, numerical studies on deformable capsules in inertial flows (45) suggest that particle equilibrium position depends on the shell compliance and particles with more flexible shells move closer to the channel center.

In Poiseuille flow, the direction of this extra deformability-induced lift force is towards the center of the channel under most operating conditions, owing to the parabolic velocity profile (41). This lift force is attributed as a factor responsible for the cell-free layer in channel flow of red blood cells even with negligible fluid inertia (47). In inertial flow, due to this other lift force focused deformable particles tend to have equilibrium positions closer to the channel center in comparison with rigid particles (40) (Figure 1-5.B). If the force balance is calibrated precisely this effect can be used to measure the mechanical properties of the suspended cells as it correlates with equilibrium position in a microchannel (40).

Furthermore, particle deformability can also affect the focusing dynamics and the velocity of lateral migration in inertial flows. Center-directed deformability-induced lift combined with wall-directed shear-gradient lift leads to an overall wall-directed lift that is lower in magnitude. This would lead to slower migration to equilibrium positions which was reported in recent studies which found that the migration of cancer cells (which are deformable) required a longer channel length than for rigid beads of the same size (48).

e) Density mismatch (inertia of particles)

Another mechanism that can lead to cross-stream migration in particulate systems is the density mismatch between the particle and fluid. If the fluid suddenly changes direction due to changing channel curvature or structures, the particle may continue for a time on a straight trajectory due to its inertia. The Stokes number, $Stk = (2\rho_p + \rho_{fl})d^2U/36\mu L$ (where ρ_p and ρ_{fl} are densities of particle and fluid, d is particle size, U is velocity change and L is length scale of change), is a dimensionless parameter that compares the flow timescale – a distance divided by velocity difference – to the particle acceleration time scale, and provides a measure of the fidelity of the particle to fluid streamlines which is especially important in particle image velocimetry. However, this number is usually quite small ($Stk < 0.01$) in microfluidic flows and even inertial microfluidic flows (unless there is an extremely large density mismatch or abrupt changes in velocity). As a result, fluid inertia, particle shape, or particle deformability most often dominate effects from particle inertia (2).

ii. EFFECTS OF PARTICLES ON FLOW

The two main elements of particle-laden fluidic systems are the fluid and the particles with several possible interactions between them. There have been multiple studies on the effect of fluid on particles, and we also discussed the interactions between particles. The other important interaction is the effect of particle on the fluid flow which we discuss here. In general, particles significantly perturb the fluid around them and cannot be considered passive components of a channel system.

Reversing streamlines are one of the distinguishing features of the flow field around a freely-rotating particle placed in a shear flow with finite Reynolds number. The reversing streamlines

can lead to repulsive particle-particle interactions (11, 49, 50). Acrivos *et al.* showed that streamlines near a cylinder in a simple 2D shear flow differs in the case of inertial flow and Stokes flow (51). The region of closed (Figure 1-6.A) streamlines diminishes with increasing Reynolds number and reversing streamlines appear due to fluid inertia. Later they experimentally confirmed the presence of reversing streamlines around a cylinder and a sphere (52). Similar reversing streamline formation for finite Reynolds number flows were also found in later studies (38, 50, 53, 54). Fluid inertia leading to reversing streamlines also resulted in breaking down of closed stream lines (Figure 1-6.A, B). The spiraling streamlines are expected to enhance mass and heat transfer (54).

Zurita-Gotor et al suggested another mechanism of reversing stream line formation that does not require fluid inertia (49). Numerical studies in a confined geometry revealed that the presence of a wall near a particle leads to breaking of closed streamlines and the generation of open and reversing streamlines. Reflection of the stresslet flow at the near wall leads to this disturbance and lateral forces that can act on another nearby particle. In Stokes flow, this results in two particles moving along stream lines with swapping trajectories. Note that the stresslet disturbance flow decays with $1/r^2$, such that this is expected to be a short range interaction.

Reversing streamlines can also be found in inertial microfluidic systems in which both fluid inertia and confining walls are present (11). Microfluidic channels typically have rectangular cross-sections and the reversing streamlines are almost identical to those in a simple shear flow, except the symmetry in the vertical direction is broken due to the parabolic base flow (Figure 1-6.C, D). As in linear shear flow, reversing streamlines appear in a channel flow for Stokes flow

conditions. This formation of reversing streamlines at both finite-Reynolds numbers and zero-Reynolds number was confirmed with numerical simulation and experiments in microchannel flows (Figure 1-6.C, D, E). The reversing streamlines act to create repulsive particle-particle interactions in the process of inertial ordering (Figure 1-6.F). These particle-induced reversing streamlines initiate the self-assembly of ordered structures in combination with inertial lift forces.

In chapter 2, we will discuss the effects of particles on flow in straight microchannels more deeply and introduce particle-induced convection, a novel phenomenon that occurs in these systems.

iii. EFFECTS OF MICROSTRUCTURES ON FLOW AND PARTICLES

Thus far, we have focused on how different forms of nonlinearities or particle asymmetry in straight channel flows lead to lift forces and unique flow disturbances. In this section, we discuss the effects of channel geometric changes on the flow and how these changes of boundary conditions induce a range of secondary flows that can be utilized to control fluid and particles. The deviations from a straight channel can be imposed in different forms such as through channel curvature, grooves channel walls. Theoretical analysis of the perturbations introduced by channel geometry is generally difficult due to the complex set of varying boundary conditions imposed on the already complex and nonlinear Navier-Stokes equations. However, we provide some insight into the physics of these systems, as well as present their applications.

a) Curving channels - Dean flow

Dean flow – the secondary flow induced in curving channels is a well-known inertial effect which is due to the momentum mismatch of fluid parcels at different cross-sections of a channel as these parcels pass around a curve (Figure 1-7.A). In this case, fluid parcels near the center flow faster and have a larger inertia directed outwards compared to the fluid parcels near the walls. In order to conserve mass, the fluid near the top and bottom walls move inwards, resulting in a set of secondary flows. The magnitude of the secondary flow is characterized by the dimensionless Dean number $De=Re(H/2R)^{0.5}$ (3, 55), where H is the channel dimension and R is the radius of channel curvature. The strength of the secondary flow depends both on the strength of the underlying downstream flow (Re), as well as the geometrical ratio $H/2R$ which, intuitively, means that a faster turn in the channel (i.e. smaller radius of curvature R) leads to a stronger Dean flow. As an inertial effect the secondary flow velocity is expected to scale with downstream velocity squared as $U_D \sim De^2 \mu/(\rho H)$ (1). Berger *et al.* also noted that increases in Dean number are associated with changes in shape of the secondary flow, with centers of the symmetric vortices moving towards the outer wall and development of boundary layers and additional vortices within the cross-section with increasing De (55).

Traditionally, secondary flows in microfluidic systems have been utilized to achieve mixing. Ugaz *et al.* employed Dean flow to control the interface of two fluids and perform fast mixing via split-and-recombine arrangement (Figure 1-7.B) (56). The ability to control fluid streams with Dean flow has also been used for 3D hydrodynamic focusing (57), and for creating a variable inertially modulated focal length lens (58). More recently, there has been an increasing interest in using curving channels to control particles in microchannels, as the developed

secondary flow enhances the lateral motion of particles across the channel and alters inertial focusing equilibrium positions by imposing a drag force (Figure 1-7.A) (59).

The two major classes of curving channels used to enhance inertial focusing are spiraling channels, with one direction of curvature (Figure 1-7.C) (59–62), and sigmoidal channels with alternating curvature (Figure 1-7.D) (2, 63, 64). A comprehensive study of inertial focusing in spiral microchannels of varying widths by Martel and Toner has provided many of the missing pieces to the overall inertial focusing parameter space (59). The flow profiles in the spiraling channel (Figure 1-7.A) are representative of the competing mechanisms that affect inertial focusing behavior in curved channels and how each mechanism depends on the channel width. As the velocity profile becomes flattened for wider channels, the shear gradient induced lift in this wide direction decreases (Figure 1-7.A.i), and as discussed previously. Simultaneously, the Dean drag on the particle increases with channel size and becomes stronger in wider channels (Figure 1-7.A.iii). Therefore, at a critical channel width, Dean drag will become the dominant mechanism for lateral migration of the particles (Figure 1-7.C). Note that unlike for spirally channels which approach a steady-state Dean flow, incorporation of alternating curvature may prevent the secondary flow from reaching steady state and leads to more complex inertial focusing behavior as a function of Reynolds number (59). In using the alternating curvature design it is important to note that opposing channel segments should be asymmetric, for if they have the exact same geometry and curvature the induced secondary flows will act counter to each other and reduce the mixing action (Figure 1-7.D).

Dean flow in spiraling channels can be employed for differential focusing of microparticles (Figure 1-7.E) (60) which has been used for high-throughput cell cycle synchronization (61). It has also been used for ordering and deterministic cell-in-droplet encapsulation (62). The alternating curvature channels were initially introduced to reduce the number of focused streams (2) and have also been found to enhance inertial focusing (tighter focusing at shorter downstream distances) compared to straight channels (63). This simple focusing mechanism has been used to achieve accurate localization of cells in microchannels to enable uniform hydrodynamic stretching in order to characterize single cells at high rates using "deformability cytometry" (Figure 1-7.F) (64).

b) <u>Grooves and herringbones on channel walls</u>

Addition of grooves and herringbones onto the wall surfaces of straight microchannels has also been known as a simple means for inducing strong secondary flows which was introduced in the seminal work of Stroock *et al.* (Figure 1-8.A) (65). These secondary flows may be used instead of Dean flows to modify inertial focusing behavior, however, most of such systems have been operated in a low-*Re* flow regime, where inertia is typically negligible. Operation with finite inertia compatible with inertial focusing appears to be less efficient. In Stokes flow, in order for the phenomenon to be effective, the grooves/herringbones must lack fore-aft symmetry otherwise, based on the MSTR theorem, there should be no *net* deformation to the fluid flow as it passes the groove which explains the need for slanted structures in these systems.

Applications in which herringbone-induced flow deformations are used provide a good starting point for identifying applications of inertia-induced secondary flows and flow deformations. The

herringbone structure has been used to create hydrodynamically focused sheath flow (66) to perform flow cytometry (67) (Figure 1-8.B). Numerical simulations also suggest that these systems can be used for size-based sorting of microparticles in combination with inertial lift forces (68). Stott *et al.* have also employed the microvortices created with these structures to mix blood, allow cells to better sample and interact with surfaces, and effectively isolate circulating tumor cells (69). However, similar to most other secondary flow inducing mechanisms, this technique has most widely been utilized to achieve fast mixing (65, 70).

In chapter 3, we will discuss the effect of simple microstructures (i.e. cylindrical pillars) on the flow. We will introduce the concept of inertial flow deformation and explain how by positioning engineered sequences of pillars we are able to control the cross-sectional shape of fluid streams accurately, at a low cost and fast.

iv. CONCLUSIONS AND PERSPECTIVES

In this chapter we introduced a variety of mechanisms by which system nonlinearity (mainly inertia) and asymmetry in channel or particle geometry can be used to control particles and flows in microfluidic platforms. Importantly, based on accumulating evidence we conclude that generation of lift or secondary flows is not the exception, but the rule for any perturbation in channel geometry or particle properties beyond the simplest cases especially in the inertial flow regime. In other words, any type of irregularity will give rise to some form of lift or secondary flow. Although most of the applications of such secondary flows in microsystems to date have focused on “mixing” and creating chaos, in the following chapters we suggest that due to their deterministic nature in laminar flow these techniques can be exploited to move in the opposite

direction: to induce order into an otherwise random system by utilizing flows transverse to downstream fluid streamlines to offer a strong tool for controllably positioning fluid parcels and particles inside microchannels.

Inertial focusing combines the benefits of a passive technique with extremely high throughput (milliliters per minute), which distinguishes it from other hydrodynamic mechanisms for cell manipulation (59). The overall understanding of inertial microfluidics has increased immensely in the past 5 years, however, there are still many areas left unexplored, from the most basic level where the nature of the lift forces is still not fully understood, to the practical level where new applications of inertial microfluidics continue to emerge at an accelerated pace, in biotechnology and diagnostics as well as other areas. Overall, inertial microfluidics is still a nascent field despite the increasing number of research articles published each year. Even though a basic tool kit of operations that can be performed on particles and fluids exists, the underlying nonlinear fluid physics is extremely rich with a multitude of fundamental directions that are still unexplored. Emerging applications of this field are being discovered at a fast pace and are only recently finding their way to translate from academic research settings into real-world and commercial devices. Still a better fundamental understanding of these systems will be necessary to enable the integration of the existing systems into more sophisticated and useful platforms towards a range of novel applications.

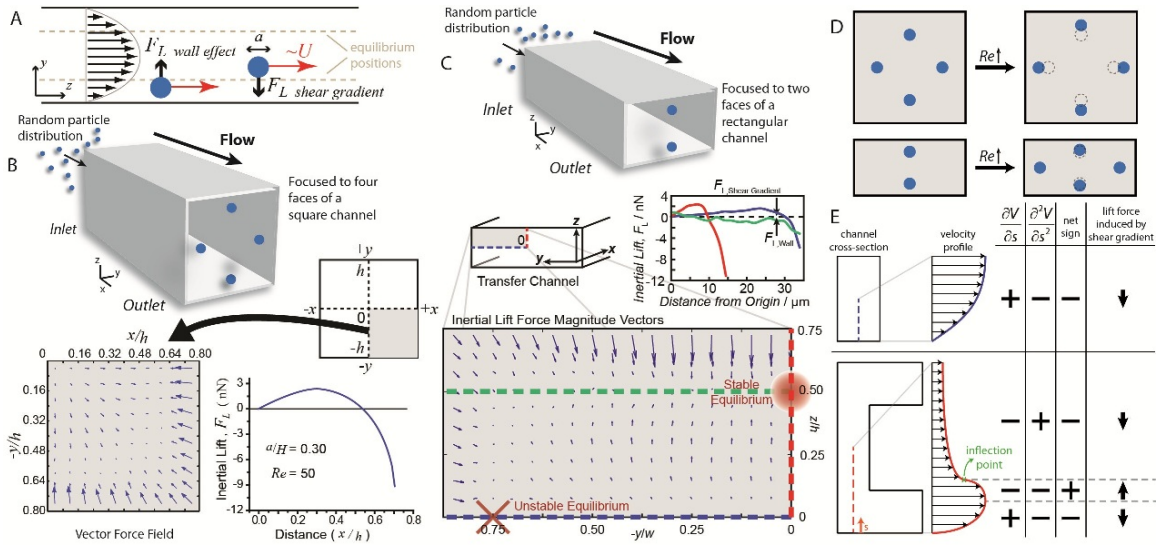

Figure 1-1. Inertial lift in straight channels. (A) Two lift forces act on a particle at finite *Re* (R_p>~1) in Poiseuille flow, (i) a wall effect that pushes the particle away from the wall, and (ii) a shear gradient lift which pushes the particle away from the center. The balance between the two forces defines the equilibrium position for the particles. This phenomenon is called inertial focusing (3). (B) In square channels, inertial focusing creates four symmetric equilibrium positions. The force map on a particle in a channel cross-section obtained by finite elements solutions also confirms that the equilibrium position is approximately at ~0.6 of the distance from center to channel wall (3, 8). (C) If the channel cross-section is rectangular, there are usually two preferred equilibrium positions. This can be explained by the force distribution across the channel, which almost always leads a randomly distributed particle to the stable equilibrium positions near the wider channel sides (9). (D) Increasing *Re* causes the focusing position to slightly shift away from the channel center, which is due to the larger increase in shift gradient lift compared to the increase in wall lift. This also could lead to stabilization of the two previously unstable equilibrium positions in rectangular channels. (E) Based on the theory proposed by Ho and Leal (7) the direction of the *shear gradient induced* lift depends on the shear rate and its gradient. As the Poiseuille flow always has a parabolic velocity profile, this force always points away from the channel center. However, should this theory be correct, in an arbitrary velocity profile with an infliction point, the direction of the force could change across the channel.

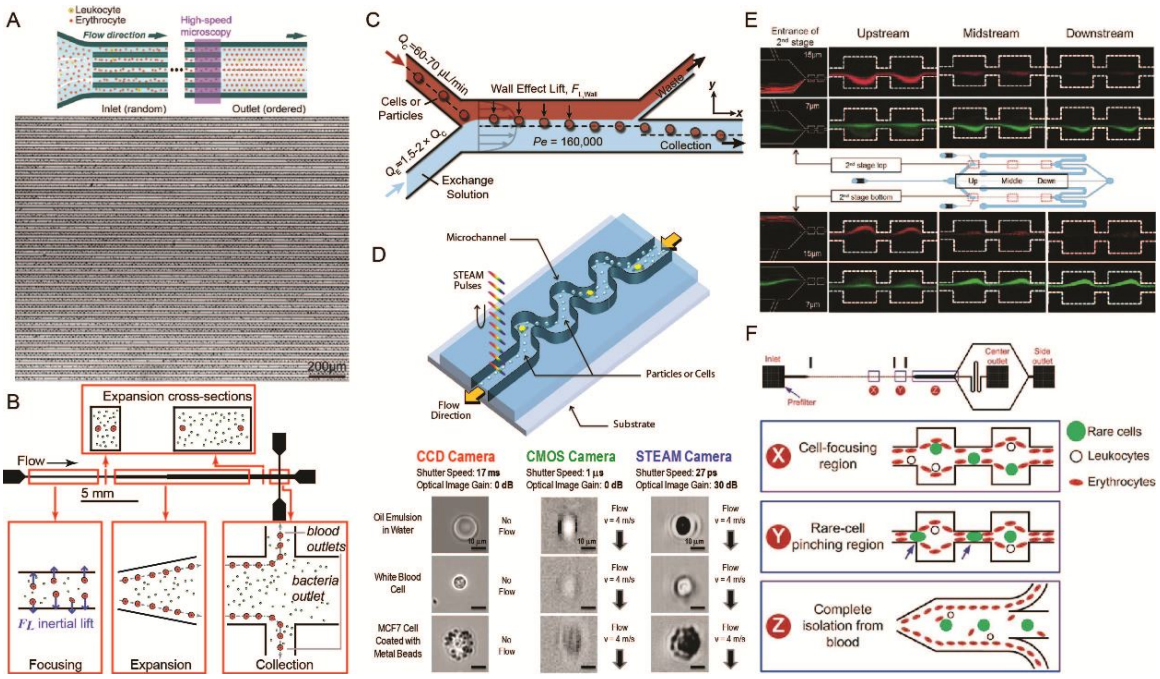

Figure 1-2. Applications of inertial microfluidics. (A) Massively parallelization of particle focusing channels is possible due to the passive nature of inertial focusing, which enables extremely high-throughput flow cytometry (13). (B) Differential inertial focusing is used for sized-based separation of smaller pathogenic bacteria from larger blood cells (14). (C) Lateral migration of particles to reach stable equilibrium positions in low aspect ratio channels is used for high purity and high yield fluid exchange (9). (D) Inertial focusing platforms can be integrated to other high-speed platform. Ordered particles are flown at a rate corresponding to STEAM camera for extremely high-throughput screening of cells an particles. STEAM technology enables imaging rates that are orders of magnitude faster than conventional CMOS cameras (15). (E) Multi-stage multi-orifice system is also used for size-based separation of particles (18). (F) Pinched flow can be employed for high-throughput separation of larger rare blood cells from blood cells (20).

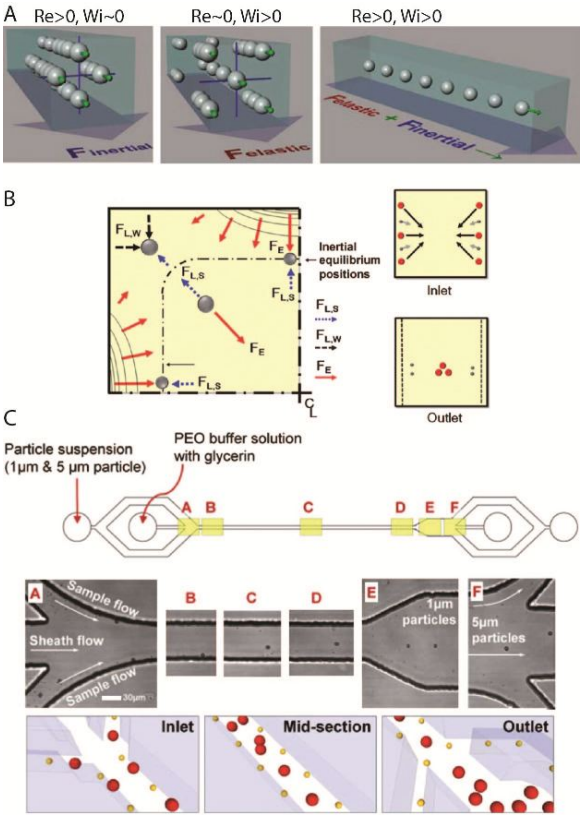

Figure 1-3. Elasto-inertial flows. (A) While inertial effects are proved to create four focusing positions near the center of channel walls (left), elastic properties of non-Newtonian fluids are shown to cause focusing neat the corners as well as the center of the channel (middle). The combined effect of the two, called elasto-inertial flow (i.e. presence of inertial effects in non-Newtonian fluids), can lead to single stream focusing of particles (right) (28). (B) Balance of inertial and visco-elastic lift forces on particles of different sizes induce different focusing positions (30). (C) This combined effect has been used for size-based separation of microparticles (30).

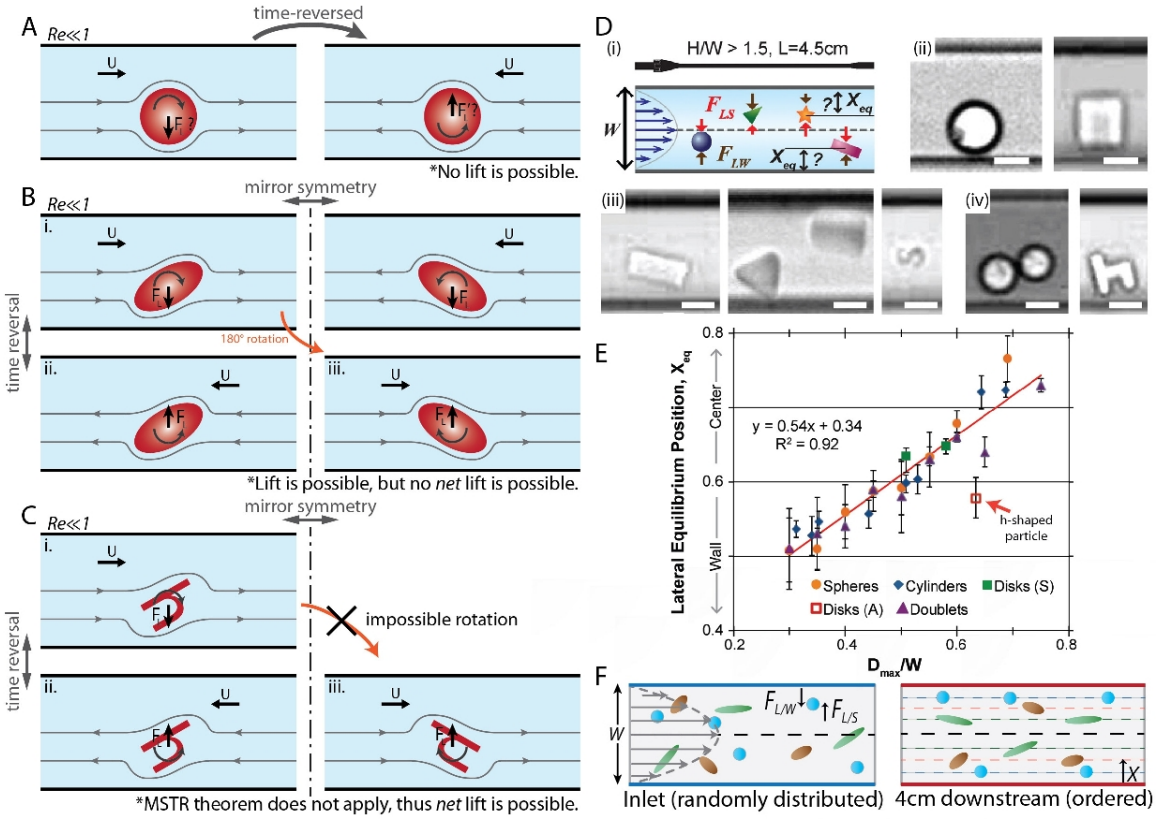

Figure 1-4. Lift forces on shaped particles. (A) MSTR theorem proves that there is no lift possible on a spherical particle in Stokes flow. (B) MSTR theorem also applies for ellipsoidal particles that are rotationally symmetric. In this case, while instantaneous lift is possible, not *net* lift can be induced on the shaped particle. (C) However, MSRT theorem does not apply to highly asymmetric shaped particles such as h-shaped, since the mirror symmetry of their time-reversed configuration cannot be achieved through rotation of the original particle. Therefore, there might exist a *net* lift in this case. (D) Lift forces and the focusing behavior of various shapes of rigid particles such as symmetric disks (ii), cylinders (iii) and asymmetric disks (iv) have been experimentally studied (39). (E) These studies reveal that most shaped particles follow the focusing behavior of a spherical particle of the similar rotational diameter, with the exception of the highly asymmetric h-shaped particle (39). (F) Ellipsoidal particles with higher aspect ratio focus closer to the center line compared to spheres of the same volume. The dependence of focusing position of the shape and aspect ratio of particles has been used for shape-based separation of bussing yeasts.

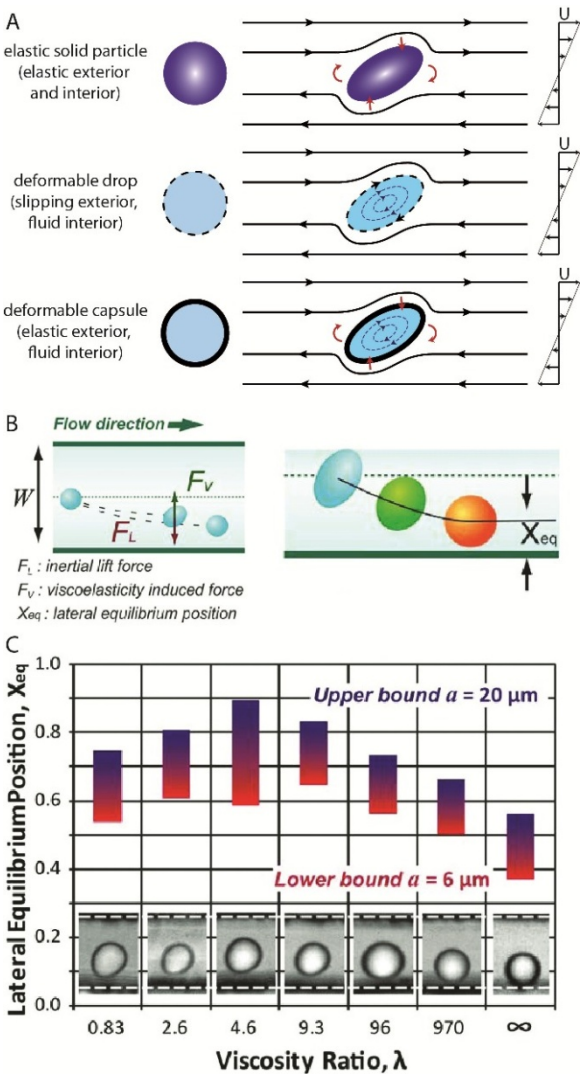

Figure 1-5. Deformable particles. (A) Three models for deformable particles include solid elastic particles, deformable droplets (with fluid interior and boundary) and deformable capsules (with fluid interior but elastic solid boundary). (B) Deformability of the particle in Poiseuille flow generally leads to induction of an extra lift force (due to particle deformation only) which directs the particle away from the wall. Balance of these forces creates a focusing position closer to the channel center, compared to rigid solid spherical particles (40). (C) Experimental data shows that, in general, increasing deformability corresponds with focusing position closer to the center (for λ from ∞ to ~4.6). There is a shift of trend at for extremely deformable particle though (λ~<4.6) (40).

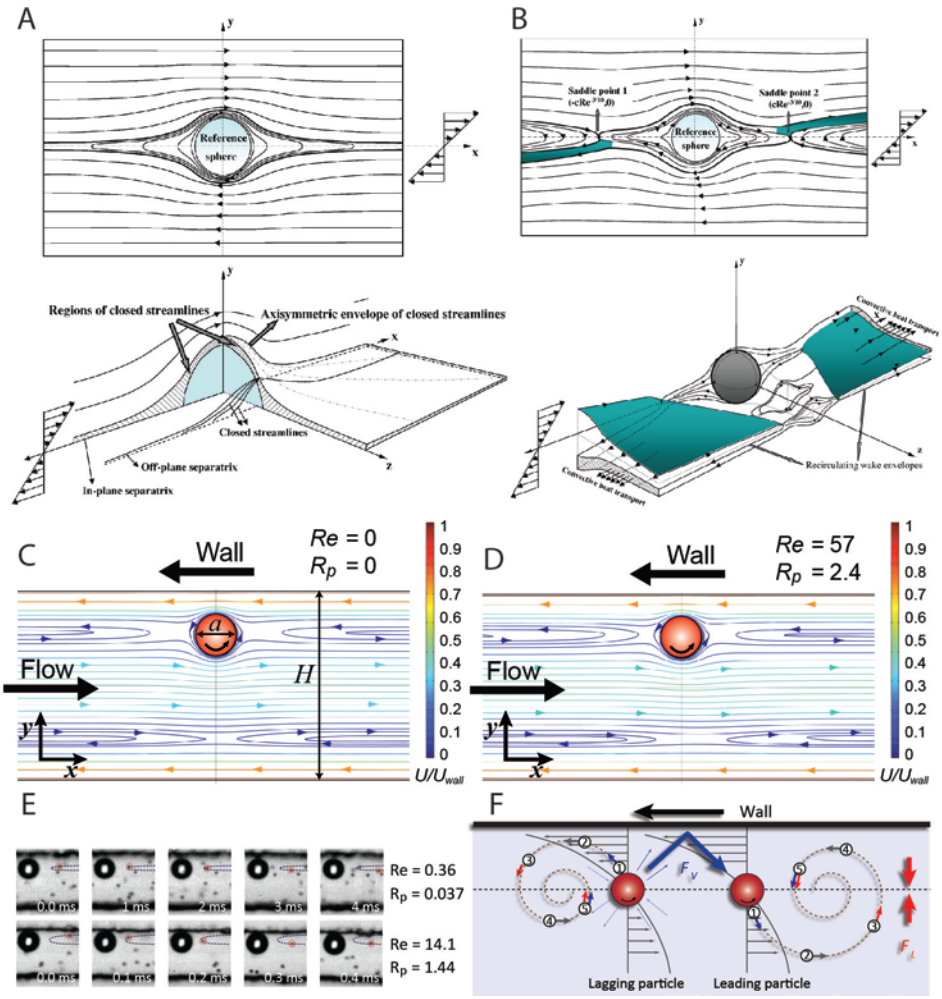

Figure 1-6. Effect of particles on flow. (A) There will be only closed streamlines near a particle in a Stokes shear flow with no confinement (no reversing streamlines) (38, 54). (B) However, it is proved that the addition of fluid inertia to the system (without confinement, unbounded flow) leads to creation of reversing streamlines and saddle points near the particle (38, 54). (C) Channel confinement, without fluid inertia, also leads to the similar creation of reversing streamlines. Interestingly, the reversing flow fore and aft of the particle are somewhat mirrored on the other half of the channel (11). (D) Real systems usually include both inertia and confinement, which inevitably create the reversing streamlines as well (11). (E) Presence of reversing streamlines has been experimentally demonstrated for very low *Re* as well as finite *Re* flows (11). (F) The reversing streamlines act as repulsive mechanism between particle pairs and contribute to their inertial ordering (11).

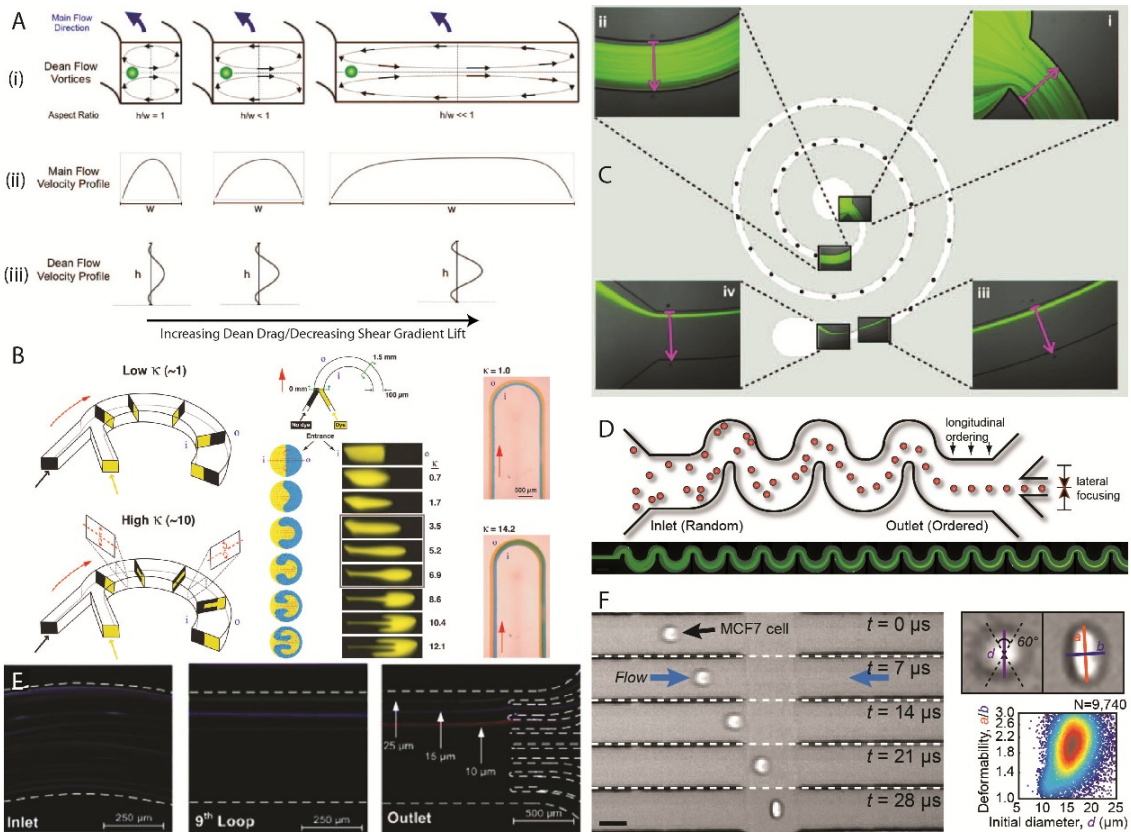

Figure 1-7. Dean flow and its applications. (A) Dean flow, an inertially-induced secondary flow, is created due to the velocity mismatch of fluid parcels in the curving channel (59). (B) It was employed to increase the interfacial surface of fluid streams to enhance microscale mixing (56). Two major classes of curving channels are generally employed in microfluidic platforms: spiraling channel (C) and alternating channel (D) (2, 59). (E) Spiraling channels have been used for differential focusing and separation of particles (61). (F) Alternating channels have been employed for accurate positioning of cells for deformability cytometry (64).

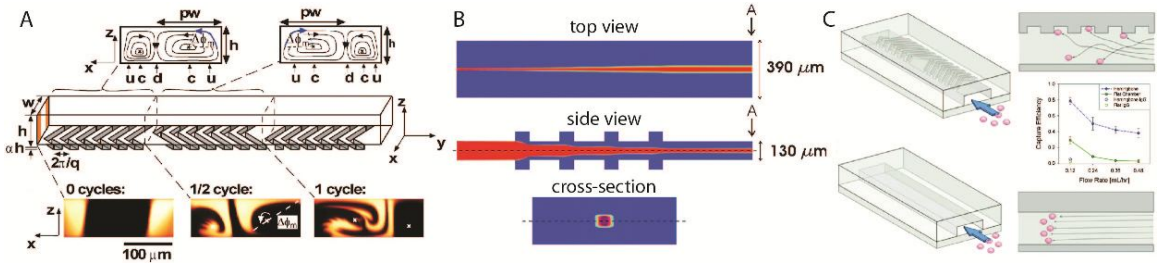

Figure 1-8. Herringbone structures. (A) Herringbones are known to induce strong secondary flows even near Stokes flow regime, and have been utilized to induce chaotic mixing in microchannels (65). (B) This phenomenon can be used to manipulate the fluid, for instance for creation of hydrodynamically focused sheath flow for flow cytometry (67). (C) The secondary flow created by this structure can also be used to manipulate particles, for instance for isolation of CTCs (69).

Bibliography

1. Squires TM, Quake SR (2005) Microfluidics: Fluid physics at the nanoliter scale. *Rev Mod Phys* 77:977–1026.

2. Di Carlo D, Irimia D, Tompkins RG, Toner M (2007) Continuous inertial focusing, ordering, and separation of particles in microchannels. *PNAS* 104:18892–18897.

3. Di Carlo D (2009) Inertial microfluidics. *Lab on a Chip* 9:3038.

4. Bretherton FP (1962) The motion of rigid particles in a shear flow at low Reynolds number. *Journal of Fluid Mechanics* 14:284–304.

5. Segré G, Silberberg A (1961) Radial Particle Displacements in Poiseuille Flow of Suspensions. , *Published online: 21 January 1961; | doi:101038/189209a0* 189:209–210.

6. Asmolov ES (1999) The inertial lift on a spherical particle in a plane Poiseuille flow at large channel Reynolds number. *Journal of Fluid Mechanics* 381:63–87.

7. Ho BP, Leal LG (1974) Inertial migration of rigid spheres in two-dimensional unidirectional flows. *Journal of Fluid Mechanics* 65:365–400.

8. Di Carlo D, Edd JF, Humphry KJ, Stone HA, Toner M (2009) Particle Segregation and Dynamics in Confined Flows. *Phys Rev Lett* 102:094503.

9. Gossett DR et al. (2012) Inertial Manipulation and Transfer of Microparticles Across Laminar Fluid Streams. *Small*:n/a–n/a.

10. Humphry KJ, Kulkarni PM, Weitz DA, Morris JF, Stone HA (2010) Axial and lateral particle ordering in finite Reynolds number channel flows. *Physics of Fluids* 22:081703–081703–4.

11. Lee W, Amini H, Stone HA, Carlo DD (2010) Dynamic self-assembly and control of microfluidic particle crystals. *PNAS* 107:22413–22418.

12. Matas J-P, Morris JF, Guazzelli É (2009) Lateral force on a rigid sphere in large-inertia laminar pipe flow. *Journal of Fluid Mechanics* 621:59–67.

13. Hur SC, Tse HTK, Di Carlo D (2010) Sheathless inertial cell ordering for extreme throughput flow cytometry. *Lab on a Chip* 10:274.

14. Mach AJ, Di Carlo D (2010) Continuous scalable blood filtration device using inertial microfluidics. *Biotechnology and Bioengineering* 107:302–311.

15. Goda K et al. (2012) High-throughput single-microparticle imaging flow analyzer. *PNAS* 109:11630–11635.

16. Sollier E, Murray C, Maoddi P, Di Carlo D (2011) Rapid prototyping polymers for microfluidic devices and high pressure injections. *Lab on a Chip* 11:3752.

17. Park J-S, Song S-H, Jung H-I (2009) Continuous focusing of microparticles using inertial lift force and vorticity via multi-orifice microfluidic channels. *Lab on a Chip* 9:939.

18. Sim TS, Kwon K, Park JC, Lee J-G, Jung H-I (2011) Multistage-multiorifice flow fractionation (MS-MOFF): continuous size-based separation of microspheres using multiple series of contraction/expansion microchannels. *Lab on a Chip* 11:93.

19. Moon H-S et al. (2011) Continuous separation of breast cancer cells from blood samples using multi-orifice flow fractionation (MOFF) and dielectrophoresis (DEP). *Lab on a Chip* 11:1118.

20. Bhagat AAS, Hou HW, Li LD, Lim CT, Han J (2011) Pinched flow coupled shear-modulated inertial microfluidics for high-throughput rare blood cell separation. *Lab on a Chip* 11:1870.

21. Lim EJ, Ober TJ, Edd JF, McKinley GH, Toner M (2012) Visualization of microscale particle focusing in diluted and whole blood using particle trajectory analysis. *Lab on a Chip* 12:2199.

22. Gao S., Hartnett J. (1993) Steady flow of non-Newtonian fluids through rectangular ducts. *International Communications in Heat and Mass Transfer* 20:197–210.

23. Matas J, Morris J, Guazzelli E (2004) Lateral Forces on a Sphere. *Oil & Gas Science and Technology* 59:59–70.

24. Ho BP, Leal LG (1976) Migration of rigid spheres in a two-dimensional unidirectional shear flow of a second-order fluid. *Journal of Fluid Mechanics* 76:783–799.

25. Leshansky AM, Bransky A, Korin N, Dinnar U (2007) Tunable Nonlinear Viscoelastic "Focusing" in a Microfluidic Device. *Phys Rev Lett* 98:234501.

26. D'Avino G, Maffettone PL, Greco F, Hulsen MA (2010) Viscoelasticity-induced migration of a rigid sphere in confined shear flow. *Journal of Non-Newtonian Fluid Mechanics* 165:466–474.

27. Villone MM, D'Avino G, Hulsen MA, Greco F, Maffettone PL (2011) Simulations of viscoelasticity-induced focusing of particles in pressure-driven micro-slit flow. *Journal of Non-Newtonian Fluid Mechanics* 166:1396–1405.

28. Yang S, Kim JY, Lee SJ, Lee SS, Kim JM (2011) Sheathless elasto-inertial particle focusing and continuous separation in a straight rectangular microchannel. *Lab on a Chip* 11:266.

29. D'Avino G et al. (2012) Single line particle focusing induced by viscoelasticity of the suspending liquid: theory, experiments and simulations to design a micropipe flow-focuser. *Lab Chip* 12:1638–1645.

30. Nam J, Lim H, Kim D, Jung H, Shin S (2012) Continuous separation of microparticles in a microfluidic channel via the elasto-inertial effect of non-Newtonian fluid. *Lab on a Chip* 12:1347.

31. Gossett D et al. (2010) Label-free cell separation and sorting in microfluidic systems. *Analytical and Bioanalytical Chemistry* 397:3249–3267.

32. Mitragotri S, Lahann J (2009) Physical approaches to biomaterial design. *Nature Materials* 8:15–23.

33. Bong KW, Pregibon DC, Doyle PS (2009) Lock release lithography for 3D and composite microparticles. *Lab on a Chip* 9:863.

34. Pregibon DC, Toner M, Doyle PS (2007) Multifunctional Encoded Particles for High-Throughput Biomolecule Analysis. *Science* 315:1393–1396.

35. Lee H, Kim J, Kim H, Kim J, Kwon S (2010) Colour-barcoded magnetic microparticles for multiplexed bioassays. *Nature Materials* 9:745–749.

36. Jeffery GB (1922) The Motion of Ellipsoidal Particles Immersed in a Viscous Fluid. *Proceedings of the Royal Society of London Series A, Containing Papers of a Mathematical and Physical Character* 102:161–179.

37. Joung C (2006) Dynamic simulation of arbitrarily shaped particles in shear flow. *Rheologica Acta* 46:143–152.

38. Subramanian G, Koch DL (2006) Centrifugal Forces Alter Streamline Topology and Greatly Enhance the Rate of Heat and Mass Transfer from Neutrally Buoyant Particles to a Shear Flow. *Phys Rev Lett* 96:134503.

39. Hur SC, Choi S-E, Kwon S, Carlo DD (2011) Inertial focusing of non-spherical microparticles. *Applied Physics Letters* 99:044101–044101–3.

40. Hur SC, Henderson-MacLennan NK, McCabe ERB, Di Carlo D (2011) Deformability-based cell classification and enrichment using inertial microfluidics. *Lab on a Chip* 11:912.

41. Tam CKW, Hyman WA (1973) Transverse motion of an elastic sphere in a shear field. *Journal of Fluid Mechanics* 59:177–185.

42. Stan CA et al. (2011) Sheathless hydrodynamic positioning of buoyant drops and bubbles inside microchannels. *Phys Rev E* 84:036302.

43. Doddi SK, Bagchi P (2008) Lateral migration of a capsule in a plane Poiseuille flow in a channel. *International Journal of Multiphase Flow* 34:966–986.

44. Shin SJ, Sung HJ (2011) Inertial migration of an elastic capsule in a Poiseuille flow. *Phys Rev E* 83:046321.

45. Kilimnik A, Mao W, Alexeev A (2011) Inertial migration of deformable capsules in channel flow. *Physics of Fluids* 23:123302–123302–6.

46. Magnaudet J, Takagi S, Legendre D (2003) Drag, deformation and lateral migration of a buoyant drop moving near a wall. *Journal of Fluid Mechanics* 476:115–157.

47. Abkarian M, Viallat A (2005) Dynamics of Vesicles in a Wall-Bounded Shear Flow. *Biophysical Journal* 89:1055–1066.

48. Tanaka T et al. (2012) Inertial migration of cancer cells in blood flow in microchannels. *Biomedical Microdevices* 14:25–33.

49. Zurita-Gotor M, Bławzdziewicz J, Wajnryb E (2007) Swapping trajectories: a new wall-induced cross-streamline particle migration mechanism in a dilute suspension of spheres. *Journal of Fluid Mechanics* 592:447–469.

50. Kulkarni PM, Morris JF (2008) Pair-sphere trajectories in finite-Reynolds-number shear flow. *Journal of Fluid Mechanics* 596:413–435.

51. Kossack CA, Acrivos A (1974) Steady simple shear flow past a circular cylinder at moderate Reynolds numbers - A numerical solution. Available at: http://ntrs.nasa.gov/search.jsp?R=19750030620 [Accessed August 13, 2012].

52. Poe GG, Acrivos A (1975) Closed-streamline flows past rotating single cylinders and spheres: inertia effects. *Journal of Fluid Mechanics* 72:605–623.

53. Mikulencak DR, Morris JF (2004) Stationary shear flow around fixed and free bodies at finite Reynolds number. *Journal of Fluid Mechanics* 520:215–242.

54. Subramanian G, Koch DL (2006) Inertial effects on the transfer of heat or mass from neutrally buoyant spheres in a steady linear velocity field. *Physics of Fluids* 18:073302–073302–18.

55. Berger SA, Talbot L, Yao LS (1983) Flow in Curved Pipes. *Annual Review of Fluid Mechanics* 15:461–512.

56. Sudarsan AP, Ugaz VM (2006) Multivortex micromixing. *PNAS* 103:7228–7233.

57. Mao X, Waldeisen JR, Huang TJ (2007) “Microfluidic drifting”—implementing three-dimensional hydrodynamic focusing with a single-layer planar microfluidic device. *Lab on a Chip* 7:1260.

58. Mao X, Waldeisen JR, Juluri BK, Huang TJ (2007) Hydrodynamically tunable optofluidic cylindrical microlens. *Lab on a Chip* 7:1303.

59. Martel JM, Toner M (2012) Inertial focusing dynamics in spiral microchannels. *Physics of Fluids* 24:032001–032001–13.

60. Russom A et al. (2009) Differential inertial focusing of particles in curved low-aspect-ratio microchannels. *New Journal of Physics* 11:075025.

61. Lee WC et al. (2011) High-throughput cell cycle synchronization using inertial forces in spiral microchannels. *Lab Chip* 11:1359–1367.

62. Kemna EWM et al. (2012) High-yield cell ordering and deterministic cell-in-droplet encapsulation using Dean flow in a curved microchannel. *Lab on a Chip* 12:2881.

63. Gossett DR, Carlo DD (2009) Particle Focusing Mechanisms in Curving Confined Flows. *Anal Chem* 81:8459–8465.

64. Gossett DR et al. (2012) Hydrodynamic stretching of single cells for large population mechanical phenotyping. *PNAS*. Available at: http://www.pnas.org/content/early/2012/04/23/1200107109 [Accessed August 13, 2012].

65. Stroock AD et al. (2002) Chaotic Mixer for Microchannels. *Science* 295:647–651.

66. Howell PB Jr et al. (2008) Two simple and rugged designs for creating microfluidic sheath flow. *Lab Chip* 8:1097–1103.

67. Golden JP et al. (2009) Multi-wavelength microflow cytometer using groove-generated sheath flow. *Lab Chip* 9:1942–1950.

68. Mao W, Alexeev A (2011) Hydrodynamic sorting of microparticles by size in ridged microchannels. *Physics of Fluids* 23:051704–051704–4.

69. Stott SL et al. (2010) Isolation of circulating tumor cells using a microvortex-generating herringbone-chip. *Proc Natl Acad Sci USA* 107:18392–18397.

70. Williams MS, Longmuir KJ, Yager P (2008) A practical guide to the staggered herringbone mixer. *Lab on a Chip* 8:1121.

Chapter 2

Intrinsic particle-induced lateral transport in microchannels

Abstract

In microfluidic systems at low Reynolds number, the flow field around a particle is assumed to maintain fore-aft symmetry, with fluid diverted by the presence of a particle, returning to its original streamline downstream. This current model considers particles as passive components of the system. However, we demonstrate that at finite Reynolds number, when inertia is taken into consideration, particles are not passive elements in the flow but significantly disturb and modify it. In response to the flow field, particles translate downstream while rotating. The combined effect of the flow of fluid around particles, particle rotation, channel confinement (i.e. particle dimensions approaching those of the channel), and finite fluid inertia creates a net recirculating flow perpendicular to the primary flow direction within straight channels which resembles the well-known Dean flow in curved channels. Significantly, the particle generating this flow remains laterally fixed as it translates downstream and only the fluid is laterally transferred. Therefore, as the particles remain inertially focused, operations can be performed around the particles in a way that is compatible with downstream assays such as flow cytometry. We apply this particle-induced transfer to perform fluid switching and mixing around rigid microparticles as well as deformable cells. This transport phenomenon, requiring only a simple channel geometry with no external forces to operate, offers a practical approach for fluid transfer at high flow rates with a wide range of applications including sample preparation, flow reaction and heat transfer.

Introduction

Microfluidic systems have shown great promise in controlling suspended cells or microparticles for applications including cell/particle separation and flow cytometry. Systems that take advantage of intrinsic microscale fluid physics are particularly practical since they require limited external instrumentation (1). Particle-laden inertial microfluidic systems, i.e. microfluidic platforms with suspended particles that operate at moderate to high particle Reynolds number, R_p (R_p>1, $R_p = \rho U a^2/\mu H$, where a is the particle diameter, H the channel width, and U is the mean downstream velocity of a fluid with density ρ and viscosity μ.), occupy a rich regime of fluid physics because: (i) suspended microparticles can occupy a significant fraction of the fluid channel in which they are traveling, interact with boundaries, and are expected to greatly perturb the surrounding flow, and (ii) the effect of fluid inertia based on the velocity difference across a particle increases with decreasing channel dimensions (H) when maintaining the same mean downstream velocity (U). The mean velocity gradient (U/H) increases with decreasing channel dimensions and, therefore, the particle Reynolds number R_p based on the velocity gradient across the particle length scale can be significant. This range of conditions allows for nonlinear effects even for a main channel flow that remains laminar (Reynolds number, $Re << 2300$, $Re = \rho UH/\mu$).

The two main elements of these systems are (i) the fluid and (ii) the particles, with several possible interactions between these elements. There have been numerous studies describing the effect of the *fluid on particles* leading to inertial lift and particle focusing that is dependent on channel geometry (2-7). Recently, we and others have also studied the *particle-particle interactions* mediated by particle-induced hydrodynamic disturbances that can lead to the dynamic self-assembly of ordered particle lattices (8-10). Here we study the less

explored effect of the *particles on the fluid* uncovering useful flow dynamics in this rich regime of fluid physics.

Flow behavior in microfluidic systems has been widely equated with Stokes flow. Assuming Stokes flow, a spherical particle stationary in a shear flow will rotate (force- and torque-free) and a series of axi-symmetric (about the vorticity axis) closed streamlines will be formed around the particle. The linearity of the Stokes flow equations leads to the property of time reversibility, further constraining the flow field around a spherical particle to have fore-aft symmetry (11).

The presence of confinement *or* fluid inertia has been shown to be associated with flow fields around particles more complex than Stokes flow-based intuition. For instance, for a cylinder or a particle in a shear flow with inertia but without confinement recirculating streamlines are observed to develop up- and down-stream of the body (12-15) with more complexity associated with increasing spatial dimensions (16). Similar behavior was also numerically confirmed near viscous drops, which resemble deformable cells, in inertial shear flow (17). Interestingly, when confinement (a wall) is theoretically added to the shear flow, inertia was found not to be required to obtain reversing streamlines, which in this case still maintain fore-aft symmetry (18). We have also experimentally demonstrated the presence of these reversing streamlines in microchannels (8). Here we aim to uncover what additional complexity arose when finite inertia was present in confined flow around a freely suspended particle. It is clear that a particle influences the surrounding flow in the presence of confinement or finite-Re, however, of particular interest is whether and how these disturbances may result in a net change in fluid streamline topology fore and aft of the particle, and methods to exploit these modifications in microfluidic systems. It is important to note that with the introduction of

various applications for inertial microfluidic systems in diagnostics (e.g. in cell separation (19, 20), solution exchange for sample preparation (21), and focusing for next generation flow cytometry (6, 22)), the effort to address the underlying physics in these systems is of both intellectual and practical importance.

Here we show that in addition to disturbances that form upstream and downstream of an inertially focused flowing particle, a net motion of fluid is induced perpendicular to the downstream flow direction. That is, fluid streamlines approaching a particle are diverted and return to a new cross-sectional position after passing the particle. This *net* secondary flow, which we refer to as "particle-induced convection" with similar characteristics to Dean flow in a curved channel (23), allows for intrinsic and high-throughput transport of solutions around particles and cells. This ability is expected to provide cost-effective solution exchange induced by the presence of the analyzed particles themselves, for applications such as sample preparation prior to flow cytometry.

Results and Discussion

Suspended particle in channel flow and creation of net secondary flow.

We study the disturbance flow of a focused and translating rotating particle in confined channel flow with and without inertia, using finite element method simulations of the 3D incompressible Navier-Stokes equations. Simulations are conducted in the frame of reference of a focused rotating particle using an iterative code that updates the wall velocity (i.e. particle velocity) and particle rotational rate until the particle is force- and torque-free (8, 24). For a single spherical particle with diameter a at its focusing position (Supplementary Information), the velocity field in the x-y plane for the inertia-less Stokes flow (Figure 2-1.a)

and the inertial flow (Figure 2-1.b) appear similar, with reversing streamlines around the rotating particle. Therefore, inertia is not required for reversing streamlines in pressure-driven channel flow in agreement with wall-bounded shear flow (18) and reversal of streamlines is due to confinement of the flow alone.

Despite the similarities, a unique *net* secondary flow is present considering finite inertia (Figure 2-1.c), while no such pattern is observed for Stokes flow (Figure S-2-1). We obtain the *net* secondary flow field ($\vec{V}$) by integrating the in-plane flow over a distance of 20*a* in the x-direction, 10*a* on each side of the particle (see the mathematical description of this operation in Materials and Methods), effectively cancelling any reversing components of the lateral flow. The integration length of 10*a* near the particle is obtained after examining the decay of the lateral motion in channel sub-regions up- and down-stream of the particle (Figure S-2-2). This is an Eulerian view of the flow as we are essentially investigating the mean lateral velocity of fluid parcels at a given plane in the channel as particles move past the plane. This approach is relevant for our system as our experiments consist of time-averaged confocal imaging of channel cross-sections (i.e. a fixed plane in space) as particles flow through the cross-section. The time-averaged lateral motion measured by microscopy in the reference frame of the channel as particles translate downstream is equivalent to the axial space-averaged lateral motion in the reference frame of the particle used to analyze the numerical results.

This net recirculating flow resembles Dean Flow (23) in curved channels with the difference that, in this case, the inertial effect is presumably created by the fluid turning around the rotating particle instead of turning around a channel bend. A recent numerical study of the flow around a particle at high *Re* ($O(1000)$), corresponding to R_p ($O(10)$), predicted local

secondary flows near a particle, but these flows were assumed to completely reverse leading to no net transfer (25) while, in contrast, we demonstrate that full reversal of the flow does not occur.

The *net* secondary flow is largely created by flow differences upstream of the particle for inertial flow. By integrating the y-direction velocity across the central plane (y=0) over intervals of particle diameter along the channel, we observe that, upstream of the particle the transverse flow is pushed closer to the particle than in Stokes flow, while downstream of the particle the transverse flow lags behind that of the symmetric transport in Stokes flow (Figure 2-1.e). Integrating over a larger 10*a* distance on each side of the particle (Figure 2-1.f) shows that surprisingly, the net transport downstream is very similar while the main difference in transport results from upstream differences. By integrating over the whole regime (from -10*a* to +10*a*), we observe that no net mass transport occurs in Stokes flow although reversing streamlines are present, whereas inertial effects generate a significant transverse flow, across the central plane. At the $z = 0$ plane, this irreversible fluid motion associated with the presence of the rotating particle creates an overall transfer of fluid from the opposite side of the channel to the particle side. However, due to conservation of mass, a corresponding amount of fluid is transferred back to the other side of the channel in regions of the cross-section that are further away from the particle, i.e. the top and bottom of the channel.

The intensity of the *net* secondary flow (V_{max}, as defined in Materials and Methods) and transverse transport scales strongly with particle size ($\sim a^3$) and exhibits an inertial ($\sim U^2$) scaling with flow velocity (Figure S-2-3, Figure S-2-4), while it scales linearly with fluid density. Furthermore, V_{max} displays a complex dependence on channel geometry: it increases with decreasing width (and increasing velocity gradient) and increasing height (for $w \leq h$,

Figure S-2-4). Reducing confinement in the height (*h*) direction perpendicular to the main velocity gradient would allow for increased transport, since the mass conserving return flow is spread further from the center cross-sectional positions near the main particle-driven flow (Figure S-2-4).

Transverse transport is dependent on the ability of particles to translate and rotate in response to the channel flow. In order to understand how different components of particle motion affect the transverse transport, we numerically constrained the physics by imposing fixed velocity and rotation rates on the particle, in turn creating a net drag and torque on the particle. Although these are not physically achievable conditions, they produce interesting insights: σ (a non-dimensional measure of the *net* secondary flow strength, as defined in Materials and Methods) increases with increasing drag force on the particle (i.e. increasing slip of the particle relative to the fluid velocity) and also with decreasing torque (i.e. increasing particle rotational rate), with the former having a more significant effect (Figure 2-1.d, Figure S-2-5). Both effects are observed to act synergistically (Figure 2-1.d) with maximum σ for particles moving backwards in the channel frame and rotating faster than expected if solely rotating according to the local fluid vorticity. Moreover, both the intensity and the direction of the *net* secondary flow depend on particle location within the channel (Figure 2-2). The lowest magnitudes and a reversal in direction are observed for positions near the channel centerline, corresponding to the smallest local velocity differences across the particle from the bulk flow.

If a particle only rotates in a confined channel in quiescent fluid (i.e. no bulk fluid motion or associated velocity gradients), there still exists a *net* secondary flow near the particle which is directed outwards from the particle at the channel centerline. The direction of net lateral

motion is in agreement with results reported by Liu and Prosperetti for a sphere rotating near a plane (26). The intensity of this flow is an order of magnitude smaller than for the case of a bulk flow driving the rotation of a particle at its inertial focusing equilibrium position (Figure S-2-6). The intensity is rather similar in magnitude and direction to that of a particle positioned off-equilibrium near the channel centerline. This suggests that in the full channel flow, a superposition of two effects is present: (i) the local velocity gradient across the particle leads to an increase in the *net* secondary flow directed towards the particle, and (ii) particle rotation in the absence of the bulk flow also generates a competing secondary flow in the opposite direction. The first effect appears to dominate near the inertial focusing position and regions of higher shear rate near the wall, while the second effect is dominant when the particle rotates in a weaker velocity gradient near the channel centerline. This suggests that the curvature of the velocity field is responsible for the variation in direction of the net secondary flow that depends on particle position in the channel cross-section. Therefore, inertial focusing plays a crucial role in positioning particles at a specific experimentally and numerically observed distance from the channel center (y_{eq}~0.6(w/2)) (24), that leads to a constructive and uniform *net* secondary flow near all focused particles.

Based on our findings, the creation of the inertial secondary flow around rotating particles in a channel is the combined result of fluid inertia, channel confinement and translation and rotation of the particle.

Experimental observation of particle-induced convection.

We next investigated the presence of the numerically predicted secondary flow and the anticipated particle-induced mass transport experimentally. We used a simple two-inlet

microchannel that allowed co-flowing a dye stream and an unlabeled water stream with suspended particles into a single rectangular main channel (Figure 2-3.a, Figure S-2-7). Using high-speed microscopy, we qualitatively observed the transverse motion of streamlines (Figure 2-3.b) for 30-50 μm polydimethylsiloxane (PDMS) particles co-injected with food dye in a 122×70 μm channel (SI Movies 1-5). The images clearly show the presence of the expected disturbance and propagation of the disturbance wave downstream with fluid moving faster than the particle. Particle rotation was confirmed by observing the rotation of intrinsic defects in the PDMS particles (24). Furthermore, the particles are observed to maintain their lateral position as they induce the disturbance in the channel.

To quantitatively characterize the effect of particles on the flow, we conducted experiments using monodisperse 10 μm particles (CV < 5%) in a 38 × 60 μm channel co-flowed with fluorescent dye. Fluorescence images were captured 2.5 cm after the interfacial contact of the two streams to examine the transport of dye. This distance is long enough to assume 10 μm particles are laterally focused (Supplementary Information). Based on the cross-sectional intensity profile, a Transport Factor (*TF*, defined in Materials and Methods) was calculated which ranges from 0 to 1 (Figure S-2-8), where 0 and 1 respectively correspond to no and full transport (i.e. homogenous distribution of the fluorescent dye over the cross-section of the channel). To identify the effect of particle concentration, various Length Fractions, φ, were considered: φ=0% (i.e. without particles), 10%, 25%, 40% or 55%. φ is defined as the fraction of the channel length covered by particles or, equivalently, as the number of particle diameters per channel length provided that the particles are focused to a single stream (Figure S-2-8) (7). As mentioned previously, in these experiments we essentially observe the cumulative effect of numerous convection sites (i.e. particles) at a fixed position in the

channel (Eulerian view) rather than following a single particle and investigating its surrounding flow (Lagrangian view).

The presence of particles enhances transport in microchannel co-flow. Without particles ($\varphi=0$) (Figure 2-4.a), extremely low Peclet numbers (or flow rates) are needed to obtain a reasonable transverse dye transport which is limited to diffusion alone. Here Peclet number, $Pe=UH/D$, is the ratio of convective to diffusive transport for fluorescent dye with a molecular diffusion constant D. As flow rate and Pe increases, the extent of transverse transport of fluorescent fluid drops considerably because dye is convected downstream faster than it can diffuse across the channel. However, when particles are present in one of the flows ($\varphi >0$) unique transport behavior is observed that is consistent with our numerical results on particle-induced convection. The extent of transport is still observed to be high at low Pe. As Pe increases, the extent of transport starts to decrease once more. However, as flow rates are reached where inertia becomes important (as seen with a higher R_p), a reversal in the trend occurs and transport starts to increase with increasing Pe. Quantifying transport with TF confirms these qualitative results (Figure 2-4.b). TF increases with increasing distance along the channel and decreases with Pe or R_p, a trend that reverses at R_p >~2. This shift of transport mode from diffusion-dominated to convection-dominated is marked in the graph. Also, increasing φ intensifies the extent of transfer: while for φ=10%, TF grows no higher than ~0.6, it approaches 1 for φ=55%, which corresponds to complete cross-stream transfer (Figure 2-4.b). This effect is quite intuitive, since increasing concentration corresponds with increasing the number of particle-induced lateral convective sites per length of the channel. The constructive effect of these sites on increasing transport is dependent on focusing to a single stream, since otherwise particles would draw fluid in different directions

and work against each other (Figure S-2-9). Importantly, even after cross-stream transport occurs, particles remain in their dynamic equilibrium positions (Figure 2-4.c and 4.d).

Cross-sectional images of the cross stream transport further support its origins in particle-induced convection (Figure 2-4.e). Using confocal fluorescence microscopy, dye is observed to be present in approximately half of the z cross-section of the channel at high flow rates. However, for φ=35% as the flow rate or particle Reynolds number increases, the fluorescent dye is stretched from right to left across the channel. This occurs in the center of the cross section near where particles are focused. Increasing flow rate intensifies this deformation and finally, at R_p=4.5, a fluorescent H-shape is easily discernible within the channel. This type of deformed dye shape is consistent with a secondary flow in which fluid is directed toward the particle stream near the channel centerline but away near the walls. Thus, confocal microscopy results (Figure 2-4.e) are in agreement with transverse convection through a *net* secondary flow that is predicted by our numerical simulations (Figure 2-1.c). Note that the dependence of the transport on R_p indicates that inertia of the fluid at the particle scale is important in creating this secondary flow.

Application to integrated fluid switching and mixing around rigid beads and cells.

Fluid switching around beads. Rigid beads can be introduced into microchannels as a simple means of enhancing convection. Fluid transfer can assist with mass transport, similar to how magnetic beads have been used for stirring of chemical reactions (27, 28), or to enhance convective heat transfer at the micro-scale. Additionally, the suspended beads can also act as functional materials, effectively increasing the available surface area for biochemical reactions or concentration of rare analytes while mixing with various reagent

streams (29). As an example, functionalized beads can be introduced into plasma to bind and remove toxins; the beads are co-flowed with the contaminated plasma to allow its faster purification, then focused and easily separated downstream to finally obtain pure plasma. The main advantages of this fluid transfer approach, compared to conventional methods include a simple and passive design (i.e. a straight channel with no active elements or complex multi-layer 3D structures), ease of use, and high throughput. That is (i) particle presence can be taken advantage of to enhance transport to and from the solid phase reaction site without the need for other system components, and (ii) particles remain in their dynamic equilibrium positions passively. Such advantages allow the unique integration of fluid switching and mixing with downstream inertial focusing applications, such as separation or interrogation, without any particle loss (Figure S-2-10.a). Further, particle-induced convection becomes more efficient at higher throughput when particles are more numerous.

Beyond transverse transport within the channel, we show fluid exchange around 10 μm rigid beads in a 46×50 μm microchannel, with practical off-chip collection of the exchanged fluid and particle streams (Figure 2-5.a). Note that diffusive mixing yields a maximum of 50% exchange. The transfer obtained for φ=0% is shown as a baseline for diffusive exchange alone. As emphasized before, an increased particle concentration means more transfer sites present along the channel (φ=35%) and increased exchange, while for higher concentrated suspensions (φ=50%), secondary effects are in play, including interparticle interactions that defocus particles and lead to transfer that is out-of-phase and destructive (Figure 2-5.e, Figure S-2-9). The exposure time, which depends on the application, can be extended by increasing the channel length. However depending on how long the flow experiences particle-induced convection, fluid elements may transfer in the channel cross-section over more than one cycle and return to an initial location, as observed for L=4.5 cm (Figure 2-5.a), reducing exchange.

Cell washing. Fluids can also be exchanged around cancer cells and leukocytes, demonstrating the relevance of the approach to biological particles (Figure 2-5.b). These cells are deformable, which compared to solid particles, causes the cells to focus slightly closer to the channel centerline (30). However, a very similar transport behavior is measured in these systems, since *TF* grows to 0.95 for HeLa cells at *Re* ~55 and to 0.7 for leukocytes. In comparison with 10 μm beads, *TF* approaches a maximum of 1 at lower *Re* for larger ~ 15 μm HeLa cells, but is delayed for smaller 7-12 μm leukocytes. Although both cell populations are expected to focus closer to the channel centerline due to their deformability and have reduced transport, this effect is apparently offset by increased transport accompanying the larger size of HeLa cells (Figure S-2-4). Such fast and simple fluid switching around cells that remain inertially focused for further downstream interrogation/separation, could potentially enable various biological applications, such as (i) washing unbound dyes from cells immediately prior to flow cytometry or removal of cryopreservation solutions before transplantation (31, 32), and (ii) mixing cells with reactants or dyes. In other words, we envision that important sample preparation steps can be integrated upstream of cell analysis or flow cytometry, eliminating the need for manual mixing and washing of samples which in a miniaturized format still remains a challenge (33-35), and enabling point-of-care diagnostics.

We were able to switch solutions around suspended cancer cells (HeLa, ~15 μm average size), flowing in a 46×50 μm channel and collect the washed cells and solution in cell and fluid outlets for analysis (Figure 2-5.c). As predicted, increasing concentrations of cells improves washing at higher flow rates that are dominated by cell-induced convection. We also observe multiple local peaks in fluid exchange for higher concentrations, which could be

due to the recirculating nature of the secondary flow. A preferred range of operation was identified below φ=25%, since cells remained focused and were only collected in the washed cell outlet, while for φ=33%, a considerable portion of cells migrated to the washing buffer stream likely due to increased crowding and inter-cell hydrodynamic interactions (8).

Blood mixing. High concentrations of blood cells also induce fluid exchange. In this application, we focus on two quantitative parameters: the amount of fluid transfered from the buffer outlet to the blood outlet (Exchange %), and the amount of cells transferred into the buffer outlet (Contamination %). Channel *Re* is calculated assuming the blood sample is diluted enough to use the viscosity of water. Despite their small size (a disc of ~2 μm in height and ~8 μm in diameter), RBCs induce a considerable amount of fluid transfer at proper concentrations (Figure S-2-10.b left). Experiments with different blood dilutions (Figure 2-5.d) confirm that the more concentrated samples generally have higher transfer. This is an especially important feature for assays involving blood since it means that this approach can work with and even benefits from less-diluted blood. Measuring the contamination for different channel lengths reveals a high Contamination % (>40%), even for short travel lengths (Figure S-2-10.b right). This means that while there is efficient fluid mixing, there exists a large cross-channel migration of the smaller and more concentrated blood cells. Importantly, fluid transfer can be considerably increased by decreasing channel width (Figure S-2-10.c) as predicted by our scaling analysis with a trade-off being lower throughput. The capability to quickly and efficiently mix blood with reactants, followed by enlarging the channel for time-controlled reaction with reactants transferred to the blood, could enable sample preparation steps such as selective lysis of RBCs before extraction of focused white blood cells (21).

There are also implications of this mixing flow beyond engineering diagnostic systems. The flow parameters in arterioles (R_p ~ 0.01, Re ~ 0.1, diameter ~ 20 μm) reveal that such cell-induced fluid transport may contribute along with other poorly understood particle-induced transport mechanisms (36-38) in these blood vessels, given the extreme length of "channel" cells travel through as they continuously circulate.

Conclusion

Here we show that fluid inertia acting in the presence of rotating particles in confined microchannels creates a *net* secondary flow, resembling the recirculating Dean flow in curved channels. This inertial effect becomes important enough to create local disturbances in the fluid flow and enhancement in cross-channel transport of the fluid that depends strongly on particle size, channel geometry, particle location in the channel, and flow conditions. As a key feature of this mechanism, we experimentally demonstrate that, for particles occupying lateral equilibrium focusing positions, only the fluid undergoes the lateral transfer, while focused particles largely remain unaffected. This approach leads to simplified deterministic fluid transfer at high flow rates, especially in systems where particles are already present in the flow. These characteristics suggest numerous applications in biological sample preparation and heat and mass transport. Applications include: high-throughput mixing at flow rates where conventional microfluidic mixers based on Stokes flow concepts fail to function, for biochemical analysis or investigation of protein folding; a simple implementation to enhance transport in micro-cooling systems; and deterministic solution exchange (without dilution) around cells for cell staining, cell washing, or selective blood lysis. We demonstrate the feasibility of the suggested applications in view of the different integrated functions required (washing of beads as mobile supports, cell washing, and blood

mixing with reactants). Systems utilizing this technique operate at extremely high throughput, require no external forces and employ simple design and fabrication methods, meeting all the requirements for being easily integrated within high-throughput microsystems (e.g. cytometry systems) (6), a crucial step towards fully integrated and automated biomedicine.

Materials and Methods

Quantitative analysis of the numerical simulations. We use the solution for the velocity field from numerical simulations to quantitatively analyze the *net* secondary flow for different flow and system conditions. To do this, we first define the *net* lateral velocity field ($\vec{V}(y,z)$=(V_y, V_z)) where $V_y(y,z) = \frac{\int_{x1}^{x2}(U_y(x,y,z))_{fluid}\,.dx}{\Delta x}$ and $V_z(y,z) = \frac{\int_{x1}^{x2}(U_z(x,y,z))_{fluid}\,.dx}{\Delta x}$. The normalized transport σ is then defined as $\sigma \equiv V_{max}/U_{avg}$, which is a measure of the strength of the *net* secondary flow. Here $V_{max} = max\{|\vec{V}(y,z)|\}$ and U_{avg} is the average downstream velocity of the main flow.

Microfabrication. Microfluidic devices were fabricated using polydimethylsiloxane (PDMS) replica molding processes (39). Standard lithographic techniques were used to produce a mold from a silicon master spin-coated with SU-8 photoresist (MicroChem Corp.). PDMS chips were produced from this mold using Sylgard 184 Elastomer Kit (Dow Corning Corporation). Inlet and outlet holes were punched through PDMS using a pin vise (Technical Innovations, Inc.). PDMS and glass were activated by air plasma (Plasma Cleaner, Harrick Plasma) and bonded together to enclose the channels.

Beads, dyes, cells and blood. Fluorescent monodisperse (10 μm, 1.05 g/ml) and non fluorescent polydisperse particles (11 μm, 1.05 g/ml) were purchased from Duke Scientific. Particles were mixed to the desired length fraction by dilution in deionized water, from φ=0 to 55%, for wt/vol % varying between 0.1% and 2.5%. To help visualization, the fluid stream can be mixed with Fluorescein (1 mM in deionized water) or with blue food dye. Particle suspensions were pumped into the devices through PEEK tubing (Upchurch Scientific Product No. 1569) using a syringe pump (Harvard Apparatus PHD 2000), for flow rates ranging from 5 to 300 μL/min. Blood was collected from healthy volunteers by a trained phlebotomist, and white cells were extracted following the protocol in Figure S-2-2.

Cell suspensions and blood. HeLa cells cultured in RPMI medium 1640 with 10% FBS were trypsinized and resuspended in PBS before use, to achieve φ=4, 25 and 33% assuming an average diameter of 15 μm. Blood was collected from healthy volunteers in BD Vacutainer tubes by a trained phlebotomist and diluted with PBS with various factors of dilution (50 X, 20 X and 10 X). To facilitate white blood cell extraction, red cells were selectively lysed (eBiosciences, 1X RBC Lysis Buffer) and removed after serial centrifugations. White blood cells were resuspended in PBS before use, to φ=35% assuming an average diameter of 12 μm.

Imaging and transfer characterization. Fluorescent images were recorded using a Photometrics CoolSNAP HQ2 CCD camera mounted on a Nikon Eclipse Ti microscope. Images were captured with Nikon NIS-Elements AR 3.0 software. Based on the fluorescent images, the intensity profile of a given channel cross-section can be drawn. From this intensity profile, the extent of transverse transport can be characterized by calculating

Transport Factor *(TF)*, defined as $2\times(\Delta H/w-0.5)$, with $\Delta H/w$ the extent of the channel cross-section whose intensity is greater than Critical Intensity ($I_c=0.2(I_{max}-I_{min})+ I_{min}$) (Figure S-2-6). *TF* ranges from 0 to 1, where 0 and 1 respectively correspond to zero and full transfer (homogenous distribution of the fluorescent dye on the cross-section of the channel). Confocal imaging was performed at the California NanoSystems Institute (CNSI) using a Leica inverted SP1 confocal microscope. Confocal images are the average of 8 y-z scans. For high-precision observations and measurements, some sequences were also recorded using a Phantom v7.3 high-speed camera (Vision Research Inc.) and Phantom Camera Control software.

Integration of fluid switching and mixing around beads and cells. Particle/cell suspensions were co-flowed with a PBS washing buffer labeled with 250 µM fluorescein, respectively at the Q_P and Q_B flow rates. L cm downstream, particle-/cell-containing solution was collected in one of two or more outlets configured to take only a sub-fraction of the total liquid flow. The sub-fraction of solution without particles was also obtained (Figure S-2-10a). For each outlet and each flow rate, fluorescence intensity is measured with a Plate Reader (Tecan) and converted to a *Exchange Percentage* (Exchange %) defined by a calibration curve obtained with serial dilutions of the fluorescent washing buffer. This parameter represents the proportion of fluorescent buffer stream transferred into the particle-laden collected fraction. Similarly, we define the *Contamination %* as the concentration of particles contaminating the buffer outlet compared to the initial concentration of the particle suspension.

Acknowledgements

We thank Dr. Peter Tseng for his assistance with confocal microscopy, Dr. Soojung Claire Hur for her assistance with high-speed imaging, Eric Tsang for his helpful advice with the Tecan Plate Reader, and Andy Chao Hsuan Lee for his valuable time on cell passaging. We would like to thank Dr. M. Schibler and the California NanoSystems Institute Advanced Light Microscopy Core Facility for their assistance with the confocal studies. This material is based upon work supported by the National Science Foundation under Grant 0930501.

Figures

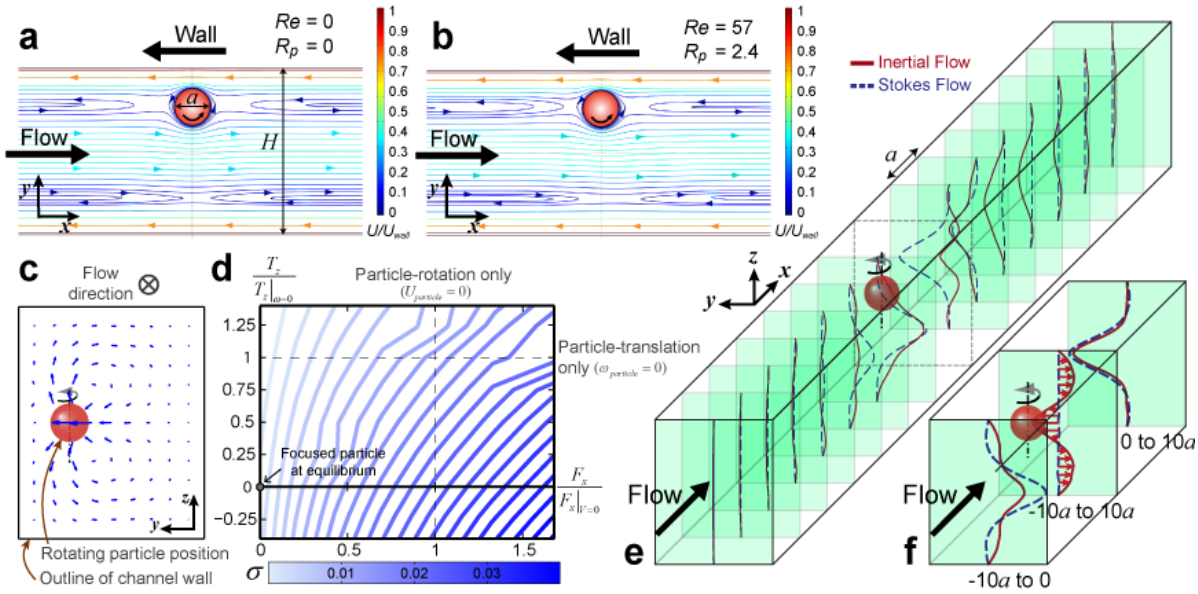

Figure 2-1. Particle-induced convection due to a combination of confinement and inertia. (a, b) Reversing streamlines in the particle frame of reference for Stokes and inertial flow, respectively. The reversing streamlines are present in confined flow, even when inertia is neglected. (c) Particle-induced convection, the *net* secondary flow created by the inertial effects of the fluid around a rotating particle, is observed by integrating the net lateral velocity (y- and z-components) along the x-axis for local y-z positions in the channel cross-section. (d) Scaling of net lateral fluid velocity (σ) with drag (F_x) and torque (T_z) imposed on the particle. Drag and torque are normalized by the drag on a stationary particle ($F_x|_{V=0}$) and torque on a non-rotating particle ($T_z|_{\omega=0}$). Numerical simulations suggest that increasing drag (i.e. a particle lagging the downstream flow) and decreasing torque (i.e. a faster rotating particle) lead to an increase in velocity of the net secondary flow. (e) Transport of the fluid across the channel is shown at different intervals along the channel, for Stokes and inertial flows. For Stokes flow (dashed blue lines) symmetric transport upstream and downstream is observed. For the inertial flow (solid red line) the transverse transport is asymmetric. Upstream of the particle, the transverse shift of the fluid is delayed compared to Stokes flow, while downstream the flow diverted around the particle again lags the Stokes flow situation. (f) Net transport upstream, downstream and over the total length of the channel is shown. Overall transport downstream is quite similar between Stokes and inertial flow. However, upstream transport results in the main overall difference. While there is no net transfer of fluid in Stokes flow, since the fluid is symmetrically diverted around the particle, significant transfer is observed in inertial flow.

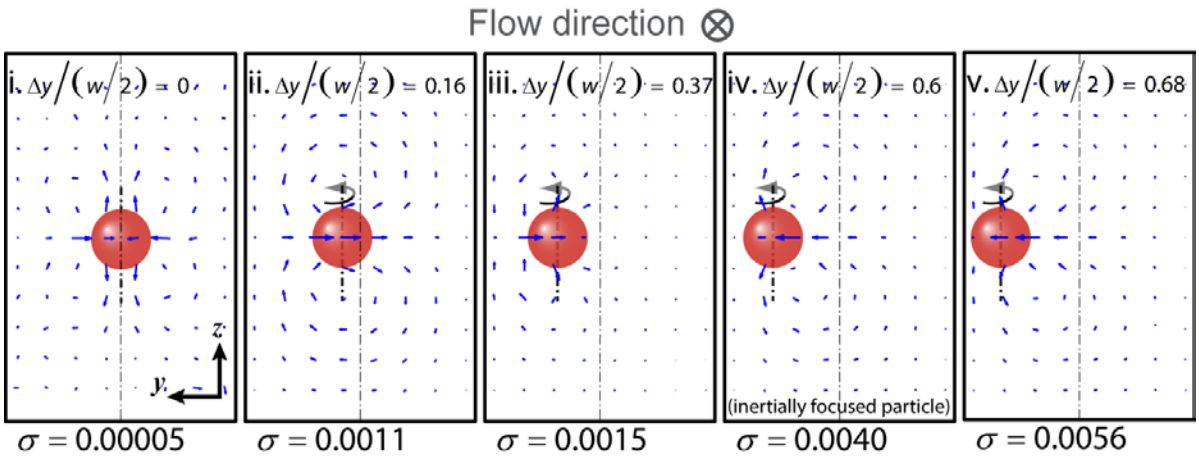

Figure 2-2. Inertial focusing leads to a consistent direction in the particle-induced convection. Both direction and intensity of the particle-induced *net* secondary flow depend on the lateral position of the drag- and torque-free particle. Even when the particle is at the channel center (completely symmetric conditions, therefore not rotating) there exists a set of net secondary flows in the channel (case i), which are nearly two orders of magnitude weaker than the normal case (i.e. inertially focused particle, case iv). When the particle is located off-center, the magnitude of the secondary flows increases (case ii), however, as the particle reaches its equilibrium position the secondary flow changes direction (compare cases iii and iv). Therefore, inertial focusing of the particle determines the lateral distance of the particle from the channel center (Δy), defining the direction of the secondary flow in experimental systems.

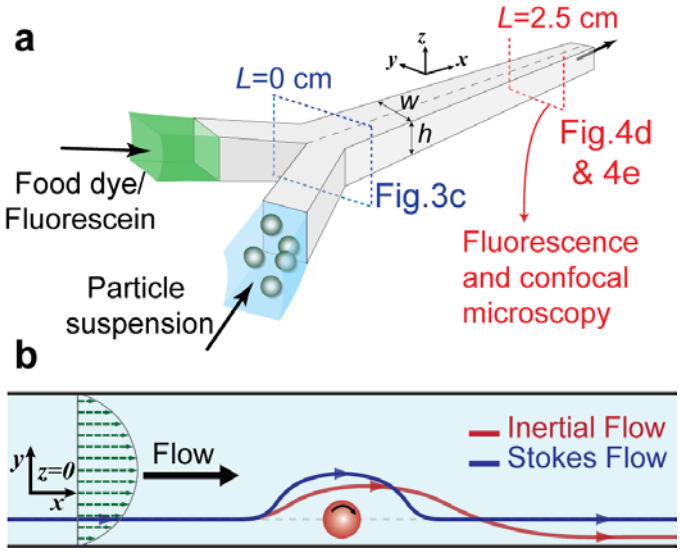

Figure 2-3. Schematic and high-speed observation of particle-induced convection. (a) Schematic of the device ($w \times h$ μm) used for microscopy. Particle suspensions are co-flowed with a fluid stream containing dyes. High-speed, fluorescence and confocal microscopy images are captured at different points along the channel to characterize the transverse transport. (b) Schematic of the motion of fluid around the rotating particle in Stokes and inertial flow at z=0. For Stokes flow the streamlines (blue line) behave symmetrically. However, for the inertial flow (red line), the path of the fluid is diverted towards the particle, resulting in a lag upstream and finally the return of the fluid elements closer to the particle than the Stokes-predicted (blue) path.

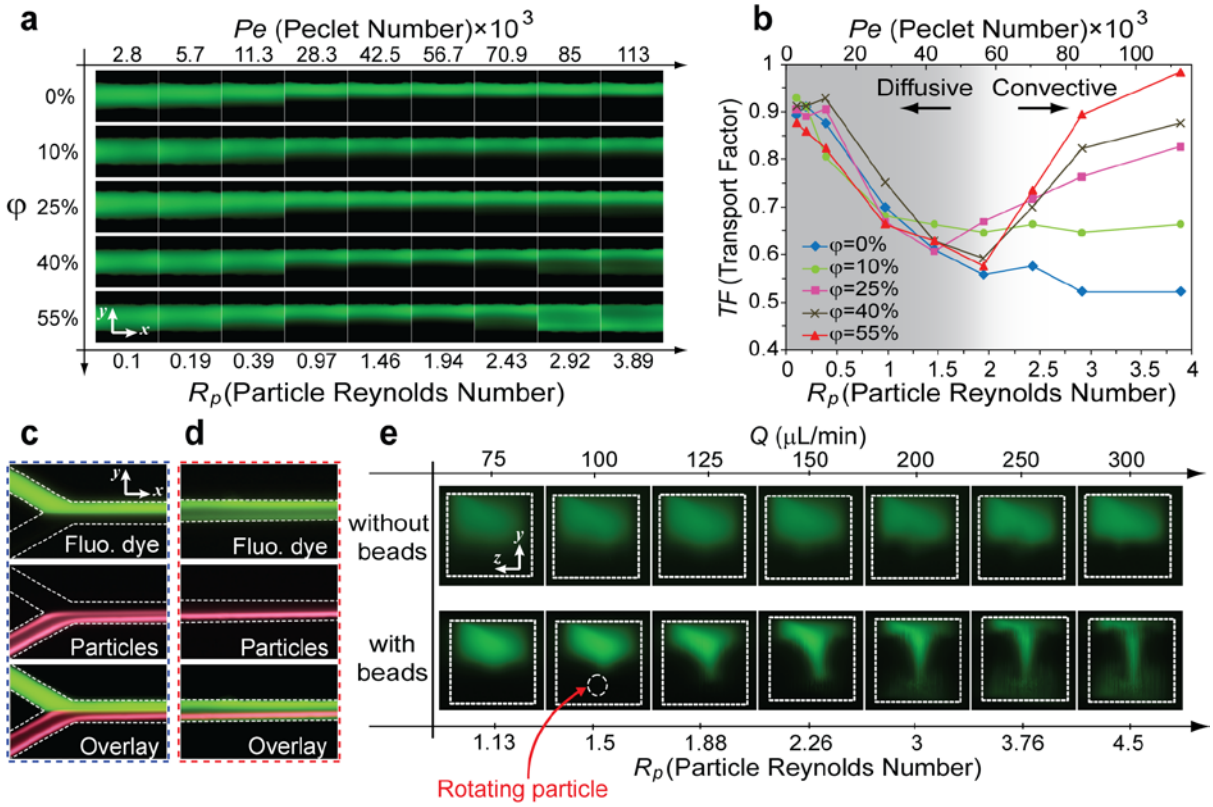

Figure 2-4. Experimental evidence confirms particle-induced convection. (a) Fluorescent images obtained 2.5 cm downstream for increasing particle Length Fractions (φ), particle Reynolds number (R_p) and Peclet number (Pe). At low Pe corresponding with low R_p, diffusion is dominant. Due to the lower flow rate, dye has enough time to diffuse across the channel, thus full transfer is observed for all φ. For φ=0%, diffusion is the only mechanism present, therefore increasing flow rate decreases the transfer. However, for higher φ as the flow rate increases, inertial effects start to become important, causing particle-induced disturbance flows that result in a net lateral transport. (b) Transport Factor measured from these experimental conditions confirms the presence of transverse stirring of the fluid at high flow rates when particles are present. The two modes of transport, diffusive and convective, are highlighted in the graph. Also, an increase in Transport Factor at high flow rates is observed with increasing Length Fraction. (c, d) Fluorescence images of both fluid and particle streams at the inlet (c) and 2.5 cm downstream (d). Particles remain focused in their equilibrium position whereas the fluid is laterally transferred. (e) Confocal images confirm the recirculating secondary flow induced by the particles. Without 10 μm beads, the fluorescent stream occupies only half of the channel at high flow rates. However, when beads are present, fluid in the center of the channel is shown to be dragged towards the particle while circulating away at the top and bottom of the channel.

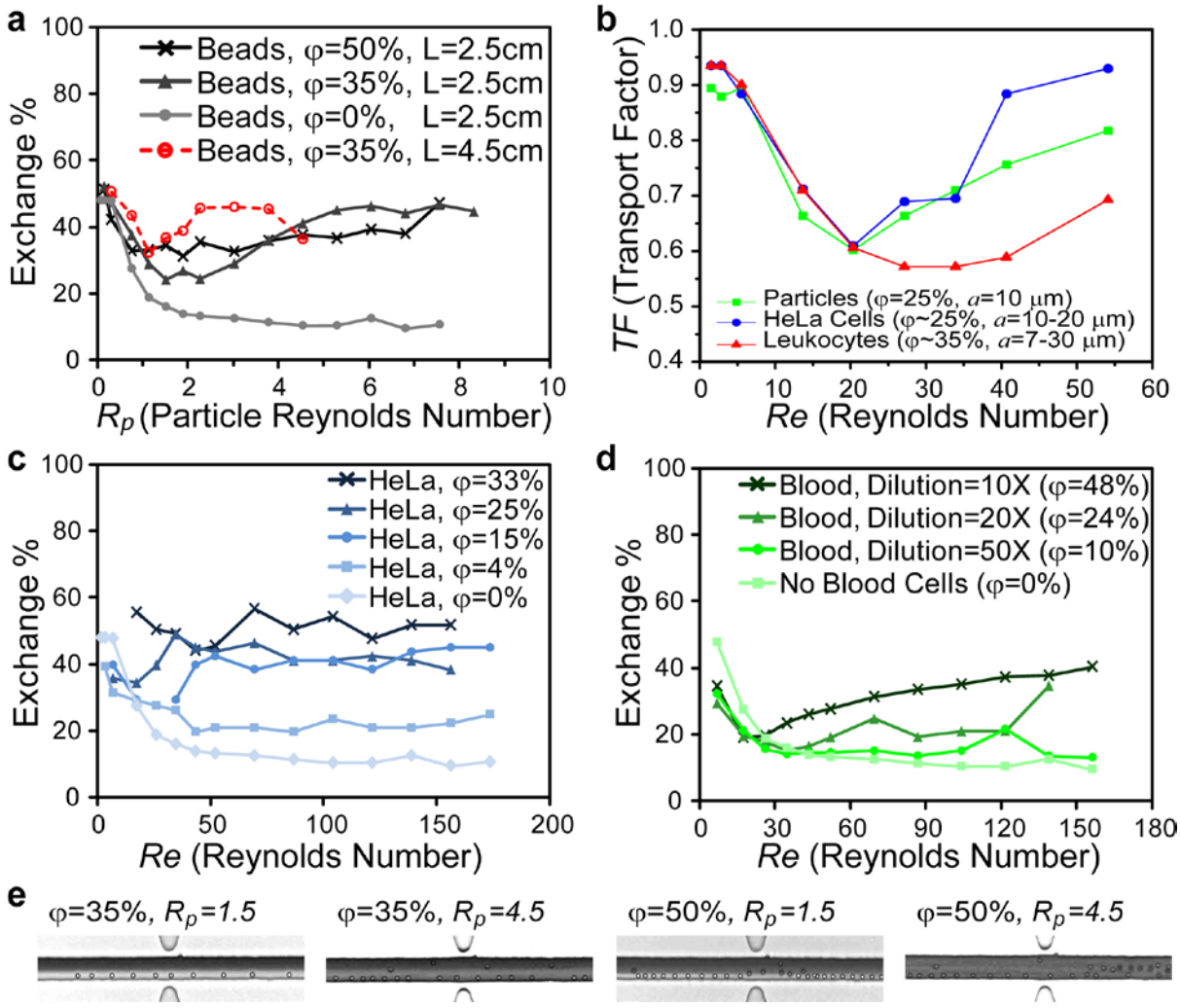

Figure 2-5. Application of particle-induced convection to fluid switching and mixing around beads and cells. (a) Demonstration of fluid exchange around 10 μm rigid beads using a 2-inlet, 2-outlet, 46×50 μm microchannel. φ=0% gives the lower limit for pure diffusive transport while the maximum limit, 50% of exchange, corresponds to complete mixing. The amount of fluid transferred into the particle stream (Exchange %), increases for increasing particle Reynolds number, with φ=35 and 50%, L=2.5 and 4.5 cm. Higher particle concentration (φ=35%) corresponds to additional transfer sites along the channel while for even higher concentrations (φ=50%), secondary effects defocus particles leading to destructive convective flows and reduced transfer. A longer channel (4.5 cm versus 2.5 cm) leads to a longer exposure time but does not necessarily increase exchange, since the fluid circulates back to the initial location in the cycle (at 200 μL/min). (b) Transport Factor increases with Reynolds number for HeLa cells (blue circles), leukocytes (red triangles) and 10 μm particles (green squares) as a comparison. (c) Exchange % increases for HeLa cells (15 μm average diameter), for increasing flow rates, with φ=4, 15, 25 and 33%. Increasing φ from 0% to 25% and 33% intensifies the extent of washing. At φ=4%, negligible fluid exchange (washing) occurs since there are not enough cells to create a strong disturbance in the flow. (d) Exchange % for blood cells decreases with dilution rate, 50X (φ=10%), 20X (φ=24%) and 10X (φ=48%), and increases with increasing flow rate. *Re* is calculated using the viscosity of water. We found a 0.9-3.6% error in Exchange % over nine experiments. (e) At increased particle concentrations, inter-particle interactions cause the particles to defocus.

For φ=35%, particles are still focused 2 cm downstream at R_p=1.5 while with intensified disturbance at R_p=4.5 a fraction of the particles leave the preferred equilibrium position. The defocusing effect is manifested at smaller R_p for higher particle concentration. For instance, for φ=50%, particles have already started defocusing at R_p=1.5, with a large fraction of particles defocused at R_p=4.5.

Supplemental Text and Figures

Inertial focusing of particles and the required channel length. In regards to the behavior of the particle itself, with a combination of confinement and inertia, it has been shown that a particle flowing downstream migrates across streamlines and focuses to a lateral dynamic equilibrium position that corresponds to channel symmetry. This inertial focusing is due to a balance between (i) a wall effect lift force, which acts to drive the particle towards the channel center, and (ii) inertial lift due to the shear gradient present in a Poiseuille flow that tends to drive the particle towards the channel wall. As a consequence, particles flowing in rectangular channels will focus to positions about half way between the center and wall of the channel. It is worth to note that at large H/a (>~10) particles are able to form trains at multiple locations across the channel. However, for the rectangular channels that we make use of here, particles normally focus to two streamlines centered on the long faces of the channel, which is further decreased to one focusing position by introducing particles from only one of the two inlets. An expression that gives the length required for particles to reach their focusing position (L_f) has been proposed which depends on fluid properties, flow velocity, particle size and channel geometry. For a flow containing 10 μm particles in a 40×60 μm channel at 100 μL/min, L_f is on the order of a few millimeters. Therefore, in a channel exceeding this length, we can assume that particles stably translate downstream at focusing positions, experiencing a steady rotational motion due to the velocity differences across them.

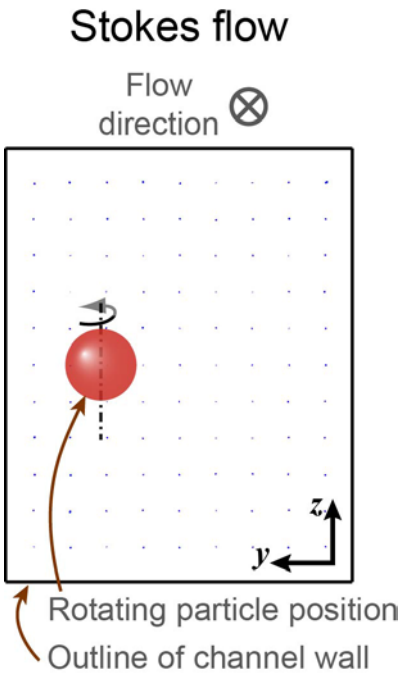

Figure S-2-1. Net lateral velocity field in Stokes flow. Due to the symmetry of the system lack of inertia (i.e. $\rho = 0$), the net transverse transfer for all points across the channel is equal to zero within numerical accuracy.

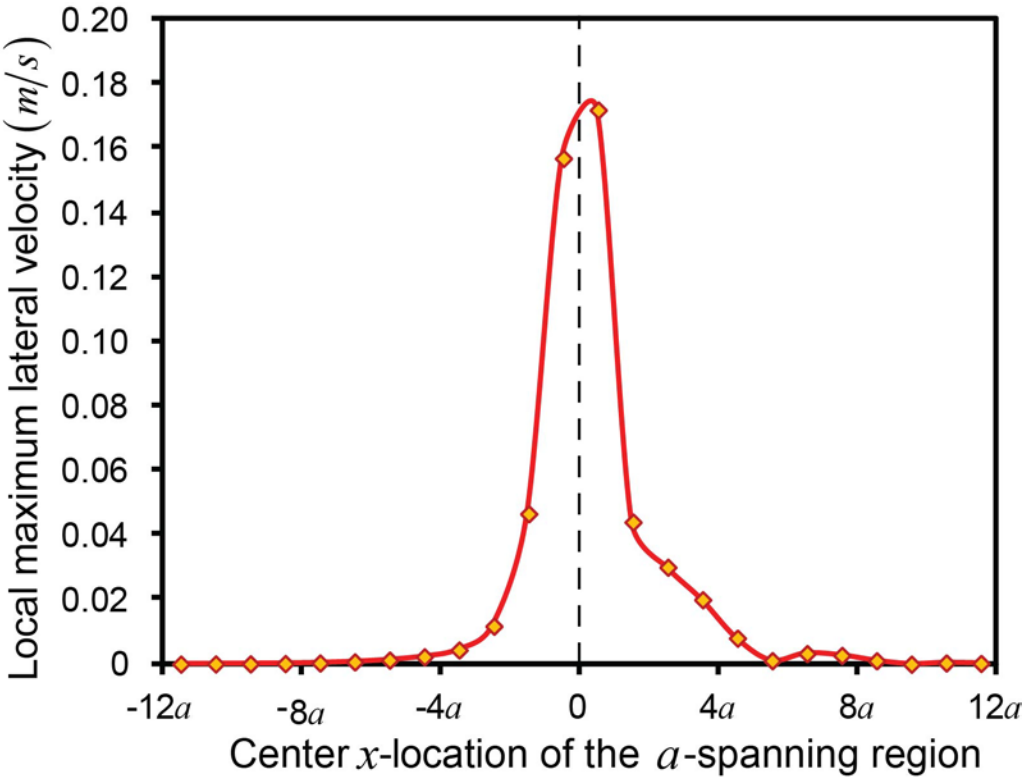

Figure S-2-2. Local net lateral motion of the fluid in channel sub-regions. The vertical axis represents the local V_{max} in channel sub-regions and the horizontal axis shows the x-position of an integrated sub-region of the channel relative to the x-position of the particle center. Each sub-region contains a portion of the channel length that spans a distance *a*. This shows that most of the lateral motion occurs near the particle and a distance of 10*a* up- and down-stream of the particle captures the majority of the fluid lateral motion. The amount of lateral motion outside of this region is smaller than our numerical precision. The length of this region could vary for different flow conditions (for instance it becomes larger for higher flow rates). We investigate each flow condition prior to applying our analysis method for each case.

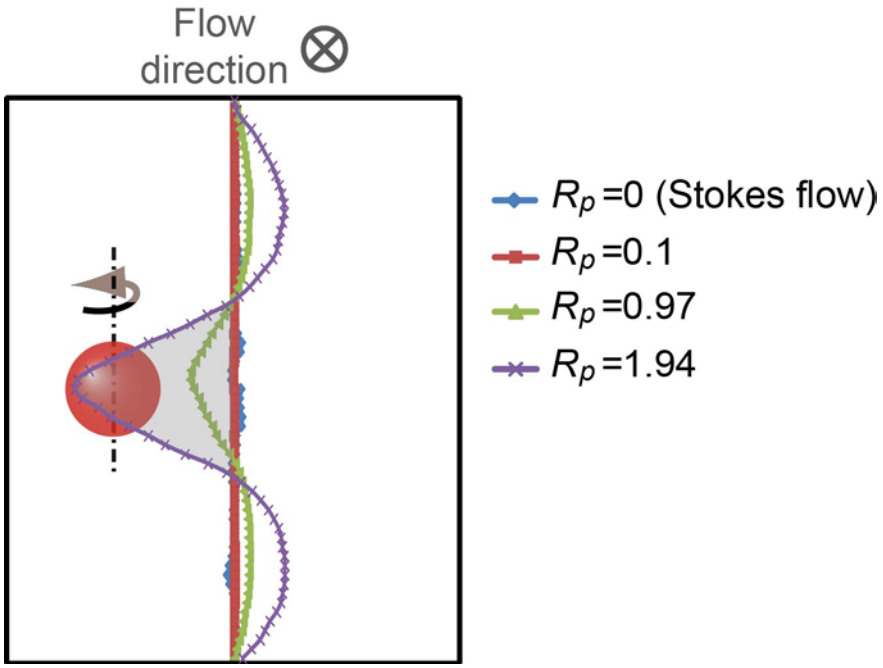

Figure S-2-3. Net y-direction mass transfer for different particle Reynolds numbers. While even at high flow rates, no net transfer is observed in the Stokes flow simulation (blue, corresponding to Q=200 μL/min), the transfer in inertial flow is strongly amplified with increasing R_p.

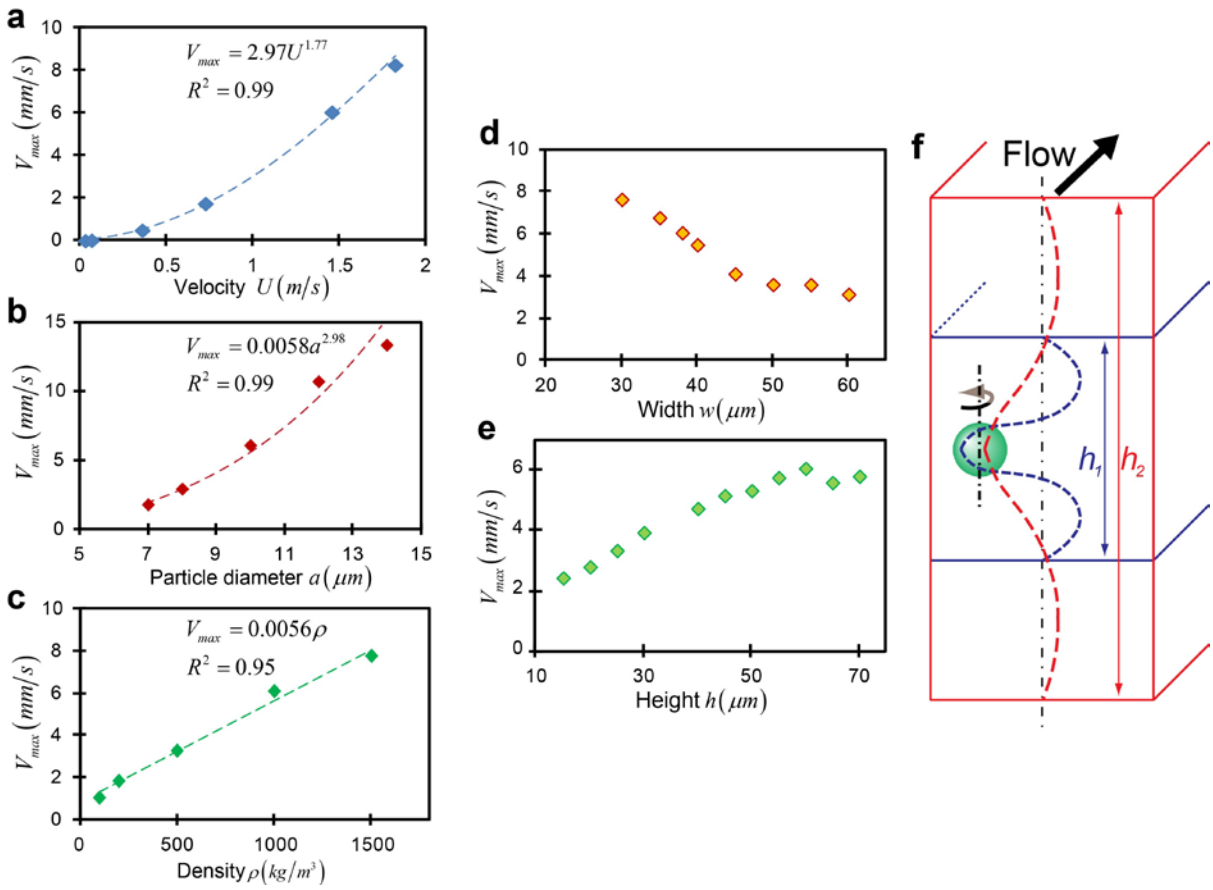

Figure S-2-4. Scaling of the transverse transport velocity (V_{max}) with dimensional parameters, and a schematic of transport for different channel heights. Particles are simulated occupying inertial focusing positions along the channel width. Except for one variable in each graph, the system parameters are as follows: *w=38 µm, h=60 µm, a=10 µm, Q=200 µL/min, ρ=1000 kg/m*^{3}*, µ=0.001 Pa.s*, and the particle is laterally located at its focusing position. (a) Transverse velocity has a best fit with $U^{1.77}$. This scaling is consistent with the importance of the inertia of the fluid around the particle. (b) There is a significant dependence on particle size, ~ a^3. The strong effect of the particle size is consistent with the amount of fluid transferred around the particle scaling with particle volume. (c) The relation between the transport and the density appears linear. (d) With increasing width and a channel height of 60 µm, the transfer decreases until it saturates for low aspect ratio channels. (e) With increasing height at a fixed channel width of 38 µm, the transfer increases until it saturates for high aspect ratios. (f) These results are consistent with the argument that when the system has a short height (h_1) compared to width it is constrained to have return flows, satisfying conservation of mass in close proximity to the generating flow around the particle. Thus, the return flow compresses the generating flow and eliminates a portion of the potential transfer. However, for taller heights (h_2), the return flows are able to extend in the z-direction, allowing for full transfer to occur. Note that confinement in the velocity gradient direction (width) leads to a stronger effect than channel height (V_{max} varies by a factor of 3 compared to 1.5 for a two-fold change in dimension).

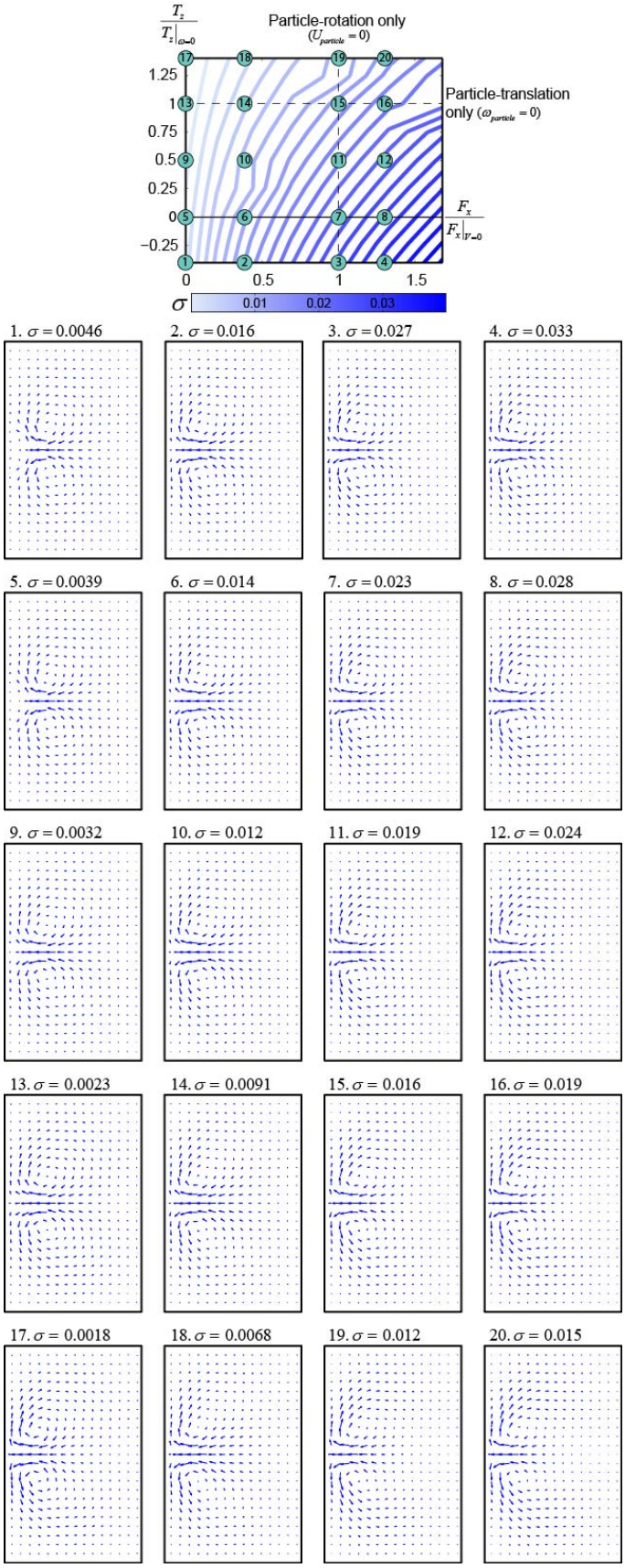

Figure S-2-5. Transverse transport velocity for various physical constraints on the particle. In order to obtain a better understanding of how different components of particle motion

contribute to the transport, we numerically solved for different conditions of pre-defined drag and torque on the particle. The results show that the velocity difference between the particle and the fluid and also particle rotation contribute to increased transport, with the former being the more significant factor. While the overall shape of the *net* secondary flow in the channel is quite similar for different drag and torque imposed on the particle, the intensity of the flow is heavily influenced by them. For instance, σ in the case of a over-rotating, backward-moving particle (case 4) is nearly 20 times larger than a counter-rotating particle moving faster than the background flow (case 17). These results also suggest that translational slip has a more significant effect on the secondary flow, compared to rotational slip.

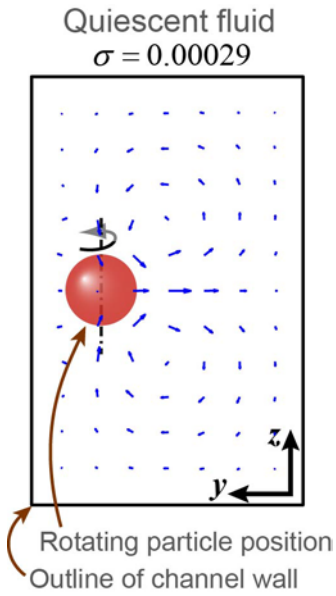

Figure S-2-6. Numerical simulations indicate that a rotating particle in quiescent fluid located in a channel also creates a *net* secondary flow. The direction of this flow is opposite to a particle similarly positioned in the presence of a bulk channel flow, and it is much weaker in magnitude. Although there is no downstream flow (thus U_{avg}=0), we obtain a normalized transport, σ, by dividing by U_{avg} that yields the same torque free rotation rate imposed on the particle in the current simulation.

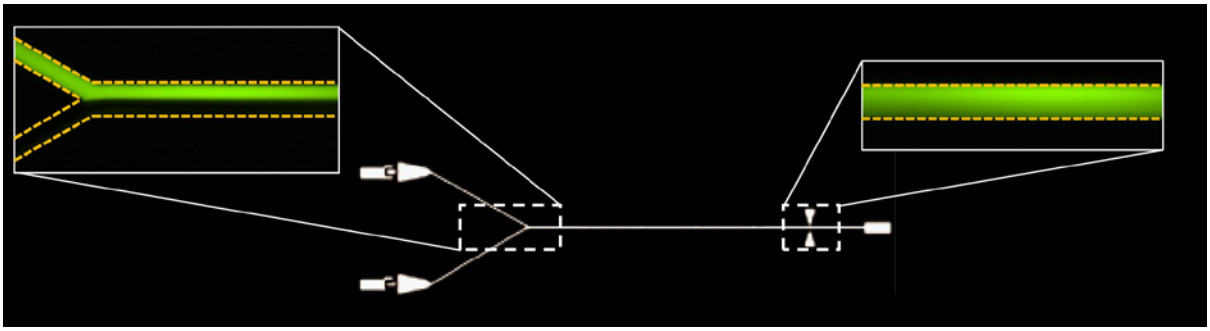

Figure S-2-7. Experimental device. A drawing of the mask used to make the device is shown. Example fluorescent images captured at the junction and 2.5 cm downstream are shown for reference. Only one inlet contains fluorescent dye, while the other solution is non-fluorescent.

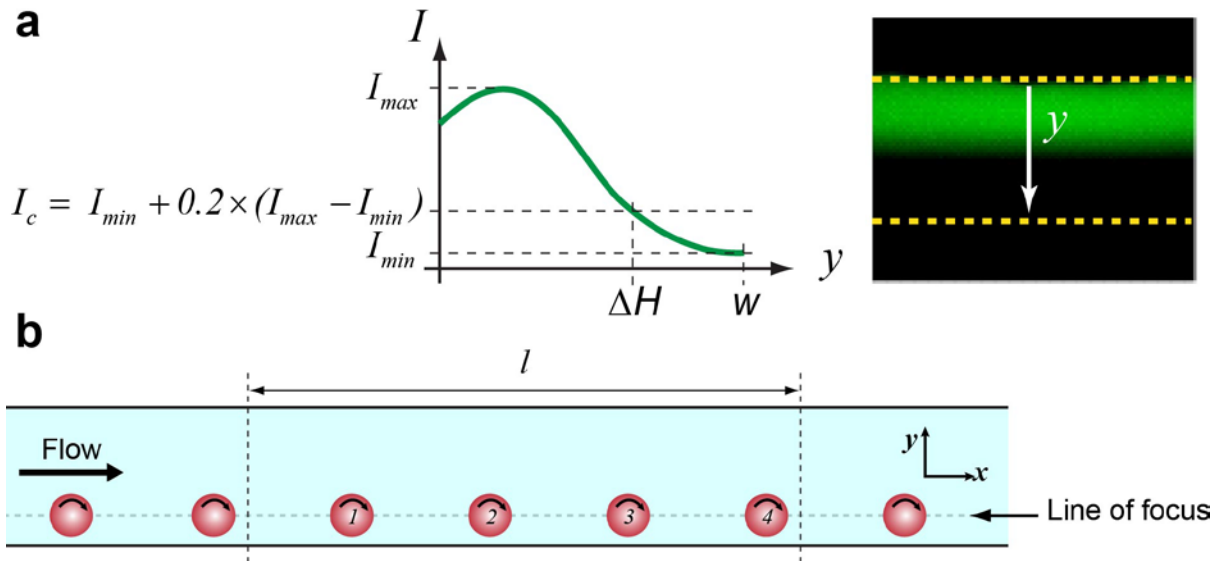

Figure S-2-8. Definition of Transport Factor (*TF*) and Length Fraction (φ). (a) The intensity profile at the point of interest along the channel is first extracted. Critical Intensity is calculated as $I_c = 0.2(I_{max}-I_{min}) + I_{min}$ and then used to define *TF* as $2\times(\Delta H/w-0.5)$, with $\Delta H/w$ being the extent of the channel cross-section in which the intensity is greater than I_c. (b) Length fraction φ is essentially a measure of particle concentration in the channel. It is defined as the fraction of the channel length that is occupied by particles, assuming that all particles are focused to a single stream. Equivalently, $\varphi = \sum a_i / l$. It is preferred to represent the concentration of the particles in channel flow as Length Fraction, rather than the conventional volumetric concentration V_f, since it provides a more comprehensive description of how many particles are positioned to disturb the flow. This parameter is more relevant than the volume fraction since, for the cases tested, particles over the whole channel volume are focused to a single focal stream. Therefore increasing the channel dimensions while maintaining the same volume fraction are expected to counterintuitively lead to different transport rates as the increased number of particles from the increased channel volume are focused to the same stream. The relationship between length fraction and volume fraction is $\varphi = 6whV_f / \pi a^2$. Note that due to the relative lengths of the system, a large φ might correspond to a moderate V_f. For instance $\varphi=25\%$ in our channels (w_{stream}=19 μm, h=60 μm, a=10 μm) corresponds to $V_f=1.148\%$.

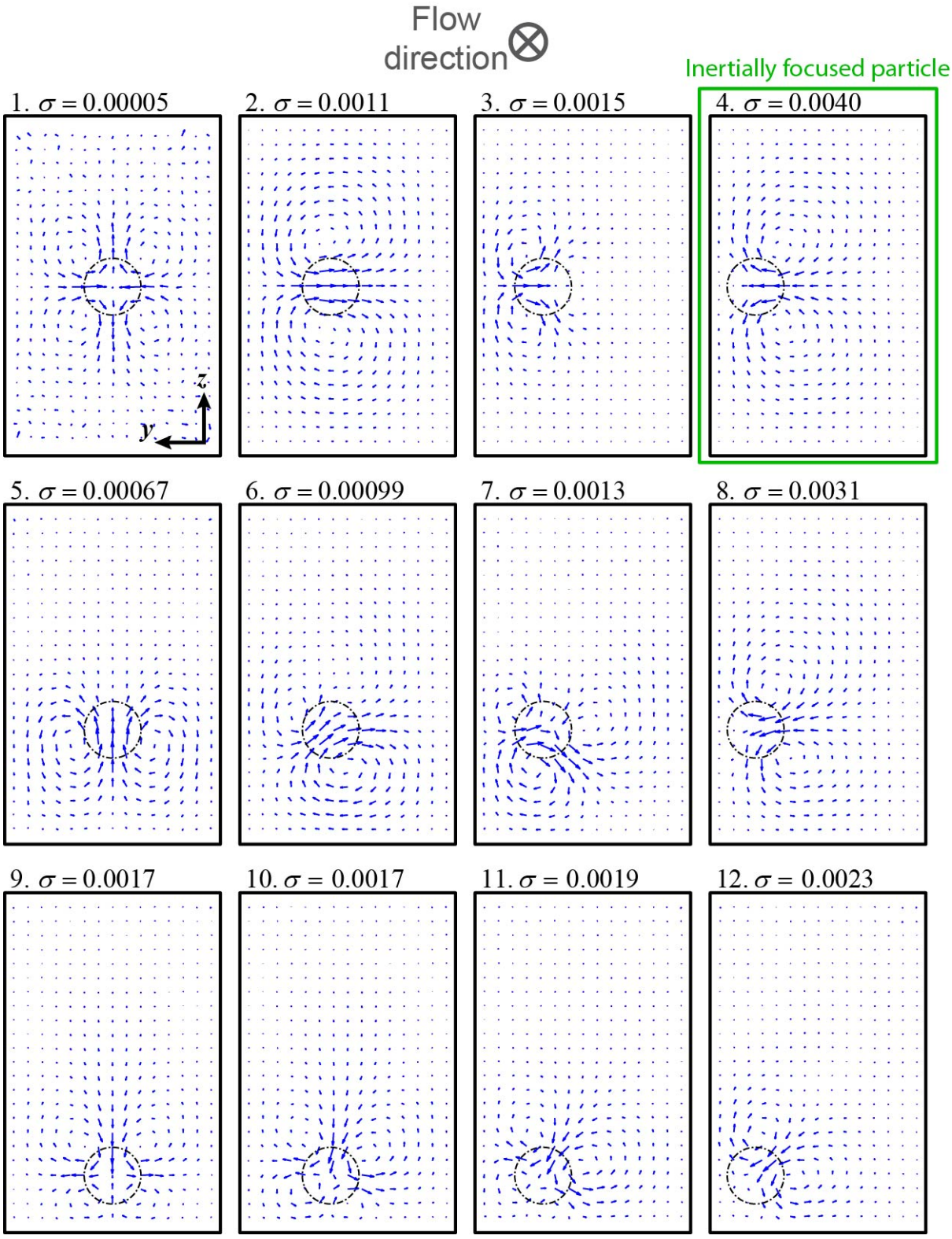

Figure S-2-9. The cross-sectional position of the drag- and torque-free particle in the channel affects the secondary flow created. A slight change in the position of the particle from its focusing position in the y-direction results in full reversal of the secondary flow (compare cases 3 and 4). Displacement in the z-direction creates additional complexity in the shape and direction of the secondary flows. For instance, three secondary flows exist in case 7. This shows that even when the particles are flowing on the same half of the channel, the secondary

flows they induce might not be in-phase and that slight displacement of the particle from its focusing position might result a set of secondary flows that are deconstructive (compared to inertially focused particles).

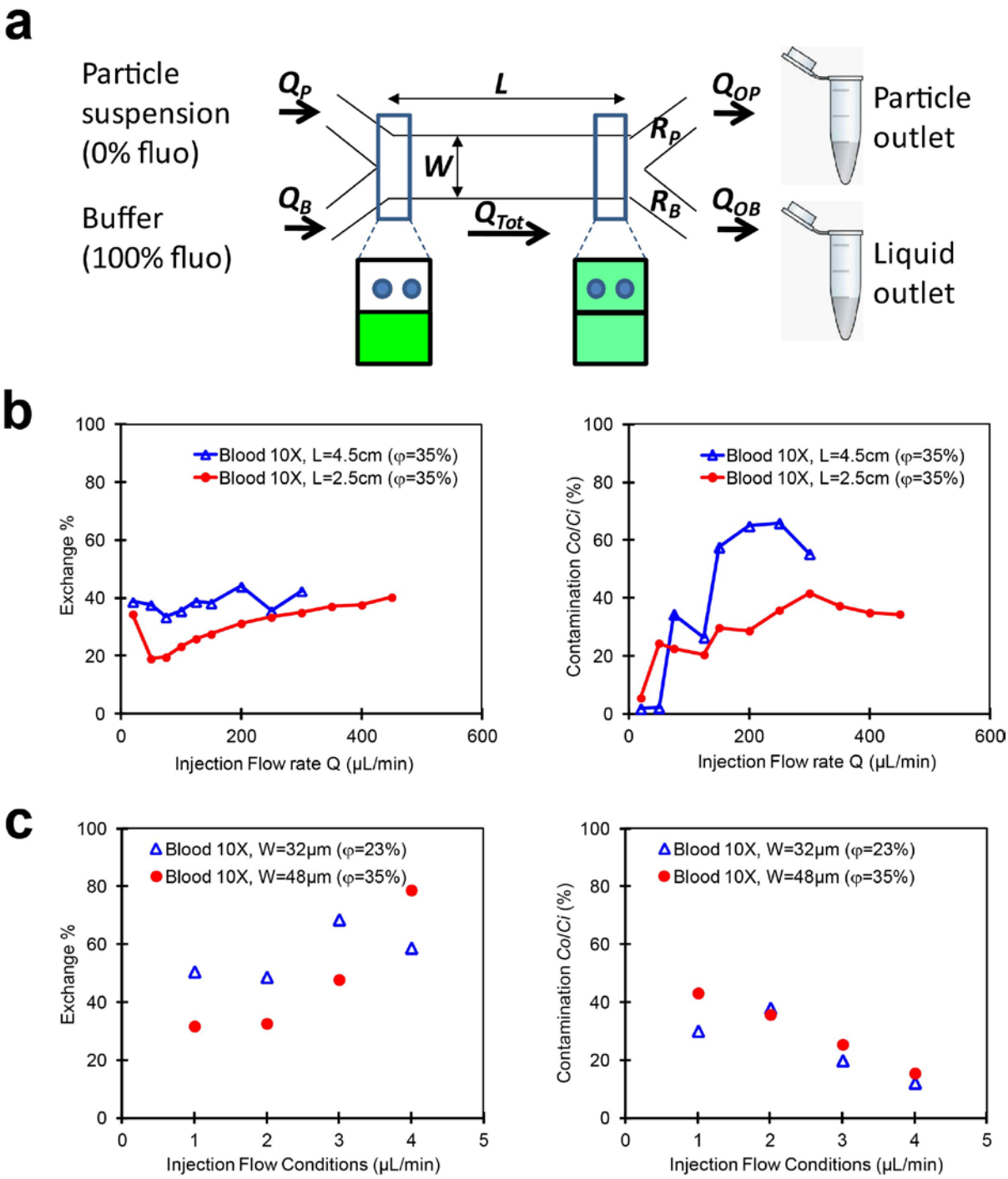

Figure S-2-10. Integration of fluid exchange or mixing around beads and cells in a microfluidic platform. (a) Schematic of the two-inlet / two-outlet device used for exchange and mixing experiments. Bead or cell suspensions are co-flowed with a washing buffer stream containing dyes, respectively at the Q_P and Q_B flow rates. L cm downstream, the two streams are extracted in two separate outlets and the exchange of fluid surrounding the particle stream is characterized for each outlet and each flow rate. The fluorescence intensity measured with a plate reader is converted to an Exchange Percentage (Exchange %) defined based on a calibration curve. Once again, the simplicity of the device is a key feature. (b) Representation of Exchange % and Contamination for 10X-diluted (φ=35%) blood injected

in two channel lengths, 2.5 and 4.5 cm, with w=48 µm. A transfer of fluid around the blood cells is observed (Exchange % up to 40% at higher flow rates). However, a significant contamination of the wash stream with red blood cells is measured for both channel lengths (>40%). Still longer channels lead to higher contamination, since red blood cells have more time to migrate across the channel. Such results demonstrate an efficient mixing function, i.e. the transfer of fluid around the blood cells but also the migration of concentrated red cells in all channel widths. (c) Representation of Exchange % and Contamination for 10X-diluted blood injected in two channel widths, 32 µm (φ=23%) and 48 µm (φ=35%), with L=2.5 cm. As observed for Flow Conditions 1 and 2 (equal inlet flow rates, Q_P=Q_B=100 and 150 µL/min for w=32 µm, Q_P=Q_B=150 and 200 µL/min for w=48 µm), the channel width significantly affects the amount of transfer since a narrower channel means a higher R_p, thus more fluid transfer, while contamination remains the same. To simultaneously increase the amount of fluid transferred in the cell stream and reduce contamination of cells in the buffer stream, the ratio of inlet flow rates can be adjusted with the cell stream being thinner than the liquid stream, such as for Flow Conditions 3 and 4 (different inlet flow rates, Q_P=80 / Q_B=120 µL/min and Q_P=100 / Q_B=200 µL/min for w=32 µm, Q_P=100 / Q_B=200 µL/min and Q_P=100 / Q_B=300 µL/min for w=48 µm).

Bibliography

1. Stroock A D et al. (2002) Chaotic mixer for microchannels. *Science* 295:647-651.

2. Segre G, Silberberg A (1961) Radial Particle Displacements in Poiseuille Flow of Suspensions. *Nature* 189:209-210.

3. Matas J P, Morris J F, Guazzelli E (2004) Inertial migration of rigid spherical particles in Poiseuille flow. *J. Fluid Mech.* 515:171-195.

4. Humphry K J, Kulkarni P M, Weitz D A, Morris J F, Stone H A (2010) Axial and lateral particle ordering in finite Reynolds number channel flows. *Phys. Fluids* 22:081703.

5. Di Carlo D, Irimia D, Tompkins R G, Toner M (2007) Continuous inertial focusing, ordering, and separation of particles in microchannels. *Proc. Natl. Acad. Sci.* 104(48):18892-18897.

6. Hur S C, Tse H T K, Di Carlo D (2010) Sheathless inertial cell ordering for extreme throughput flow cytometry. *Lab Chip* 10:274-280.

7. Di Carlo D (2009) Inertial microfluidics. *Lab Chip* 9:3038-3046.

8. Lee W, Amini H, Stone H A, Di Carlo, D (2010) Microfluidic crystals: Self-assembly and control of particle streams. *Proc. Natl. Acad. Sci.* 107(52):22413-22418.

9. Kulkarni P M, Morris J F (2008) Pair-sphere trajectories in finite-Reynolds number shear flow. *J. Fluid Mech.* 596:413-435.

10. Yan Y, Morris J F, Koplik J (2007) Hydrodynamic interaction of two particles in confined linear shear flow at finite Reynolds number. *Phys. Fluids* 19:113305.

11. Bretherton F P (1962) The motion of rigid particles in a shear flow at low Reynolds number. *Journal of Fluid Mechanics* 14:284-304.

12. Kossack C A, Acrivos A (1974) Steady simple shear flow past a circular cylinder at moderate Reynolds numbers: a numerical solution. *J. Fluid Mech.* 66(3):353-376.

13. Poe G G, Acrivos A (1975) Closed-streamlline flows past rotating single cylinders and spheres: inertia effects. *J. Fluid Mech.* 72(4): 605-623.

14. Mikulencak D R, Morris J F (2004) Stationary shear flow around fixed and free bodies at finite Reynolds number. *J. Fluid Mech.* 0:1-28.

15. Kulkarni P M, Morris J F (2008) Suspension properties at finite Reynolds number from simulated shear flow. *Phys. of Fluids* 20:040602-13.

16. Subramanian G, Koch D L (2006) Centrifugal forces alter streamline topology and greatly enhance the rate of heat and mass transfer from neutrally buoyant particles to a shear flow. *Phys. Rev. Lett.* 96:134503.

17. Singh R K, Sarkar K (2011) Inertial effects on the dynamics, streamline topology and interfacial stresses due to a drop in shear. *J. Fluid Mech.* 683:149-171.

18. Zurita-Gotor M, Lawzdziewicz J B, Wajnryb E (2007) Swapping trajectories: a new wall-induced cross-streamline particle migration mechanism in a dilute suspension of spheres. *J. Fluid. Mech.* 592:447-469.

19. Mach A J, Di Carlo D (2010) Continuous scalable blood filtration device using inertial microfluidics. *Biotechnology and Bioengineering* 107(2):302-311.

20. Bhagat A A S, Hou H W, Li L D, Lim C T, Han J (2011) Pinched flow coupled shear-modulated inertial microfluidics for high-throughput rare blood cell separation. *Lab Chip* 11:1870-1878.

21. Gossett D R, Tse H T K, Dudani J S, Goda K, Woods T A, Graves S W, Di Carlo D (2012). Inertial manipulation and transfer of microparticles across laminar fluid streams. *Small* accepted.

22. Oakey J, Applegate R W, Arellano E, Di Carlo D, Graves S W, Toner M (2010) Particle Focusing in Staged Inertial Microfluidic Devices for Flow Cytometry. *Anal Chem.* 82(9):3862-3867.

23. Squires T M, Quake S R (2005) Microfluidics: Fluid physics at the nanoliter scale. *Rev. Mod. Phys.* 77**(**3):977-1026.

24. Di Carlo D, Edd J F, Humphry K J, Stone H A, Toner M (2009) Particle segregation and dynamics in confined flows. *Phys. Rev. Lett.* 102:094503.

25. Shao X, Yu Z, Sun B (2008) Inertial migration of spherical particles in circular Poiseuille flow at moderately high Reynolds numbers. *Phys. Fluids* 20:103307.

26. Liu Q, Prosperetti A (2010) Wall effects on a rotating sphere. *J. Fluid. Mech.* 657:1-21.

27. Lee S H, van Noort D, Lee J Y, Zhang B T, Park T H (2009) Effective mixing in a microfluidic chip using magnetic particles. *Lab Chip* 9:479-482.

28. Gambin Y, VanDelinder V, Ferreon A C M, Lemke E A, Groisman A, Deniz A A (2011) Visualizing a one-way protein encounter complex by ultrafast single-molecule mixing. *Nature Methods* 8(3):239-241.

29. Peyman S A, Iles A, Pamme N (2009) Mobile magnetic particles as solid-supports for rapid surface-based bioanalysis in continuous flow. *Lab Chip* 9:3110-3117.

30. Hur S C, Henderson-MacLennan N K, McCabe E R B, Di Carlo D (2011) Deformability-based cell classification and enrichment using inertial microfluidics. *Lab Chip* 11:912-920.

31. Augustsson P, Åberg L B, Swärd-Nilsson A-M K, Laurell T (2009) Buffer medium exchange in continuous cell and particle streams using ultrasonic standing wave focusing. *Microchim Acta* 164:269-277.

32. Mata C, Longmire E, McKenna D, Glass K, Hubel A (2010) Cell motion and recovery in a two-stream microfluidic device. *Microfluid Nanofluid* 8:457-465.

33. De Mello A J, Beard N (2003) Dealing with real samples: sample pre-treatment in microfluidic systems. *Lab Chip* 3:11N-19N.

34. Toner M, Irimia D (2005) Blood on a chip. *Annu. Rev. Biomed. Eng.* 7:77-103.

35. Mariella R (2008) Sample preparation: the weak link in microfluidics-based biodetection. *Biomed. Microdevices* 10:777-784.

36. Nanne E E, Aucoin C P, Leonard E F (2010) Molecular movement of bovine albumin in flowing suspensions of bovine erythrocytes. *Chemical Engineering Science* 65(24):6389-6396.

37. Tokarev A A, Butylin A A, Ataullakhanov F I (2011) Platelet adhesion from shear blood flow is controlled by near-wall rebounding collisions with erythrocytes. *Biophys. J.* 100(4): 799-808.

38. Turitto V T, Baumgartner H R (1975) Platelet interaction with subendothelium in a perfusion system: physical role of red blood cells. *Microvascular Research* 9:335-344.

39. Sollier E, Murray C, Maoddi P, Di Carlo D (2011) Rapid prototyping polymers for microfluidic devices and high pressure injections. *Lab Chip* 11:3752-3765.

Chapter 3

Programming fluid flow using sequenced microstructures

Abstract

Control of fluid streams is useful in biological processing (1-3), chemical reaction control (4, 5), and creating structured materials (6-8), however, general strategies to engineer the cross-sectional form and motion of fluid streams have been limited. Strategies to mix fluid (1, 9, 20) and control particles (11, 12) using engineered systems exist, often relying on chaotic fluid transformations as an effective tool (13, 14) to disrupt sustained regions of order in the flow (10, 15). Rather than apply flow transformations to prevent order, here we develop a hierarchical approach to engineer fluid streams into a broad class of complex configurations. We make use of the inertial flow deformations associated with the flow around a library of single cylindrical pillars at eight positions within a microfluidic channel as our fundamental operations. Since these transformations provide a deterministic mapping of fluid elements from upstream to downstream of a pillar, we can sequentially arrange pillars to apply the associated nested maps and therefore program complex fluid structures without additional numerical simulation. Consequently, functions composed of multiple pillars such as 'rotate stream to centerline', or 'move stream right', can be hierarchically assembled to execute practical programs. To show the range of capabilities we demonstrate programs to sculpt the cross-sectional shape of a stream into complex geometries (such as various concavity polygons, closed rings, and inclined lines), move and split a fluid stream, transfer particles from a stream, and separate particles by size. The introduction of a general strategy to program fluid streams in which the complexity of the nonlinear equations of fluid motion are abstracted from the user can impact biological, chemical and materials automation in the

same way that abstraction of semiconductor physics from computer programmers enabled a revolution in computation.

We use cylinders placed at various cross-stream locations of a channel as the fundamental operators for our programming scheme (Figure 3-1A).These geometric obstacles can be used to induce significant deformations in flow, creating useful *net* rotational secondary flows that locally move and deform fluid parcels. Notably, this net twisting of fluid around a pillar has been neglected in microfluidic systems because fluid inertia is often not considered important (16). Flow around a pillar in a straight channel without inertia (i.e. Stokes flow) requires fore-aft symmetry because of the mirror symmetry of the flow upon time-reversal of the linear equations of motion (17).Therefore, any secondary fluid motion directed within the channel cross-section (18) is completely reversed after passing the cylinder midplane.

Unlike the fluid motion that completely reverses upon passing a micro-pillar for Stokes flow, flow with finite inertia is accompanied by a net deformation of fluid streams. Numerical simulations predict that as fluid passes centrally positioned pillars in a straight microchannel, the flow deforms in such a way that the fluid parcels near the channel centerline move outwards towards the side walls, while fluid parcels near the top and bottom walls move towards the channel center (Figure S-3-1). This phenomenon, validated experimentally (Figure S-3-2), effectively creates a set of *net* rotational secondary flows within the microchannel (Figure 3-1A, SI Text). As a result, the flow is irreversibly twisted, losing its fore-aft symmetry near the pillar and causing a significant final deformation of the flow stream (Figure 3-1B). The phenomenon has features in common with the secondary flow created in curved channels with finite inertia (Dean flow) (1, 19, 20). Both phenomena are inertially induced and require high velocity gradients provided by confined 3D channels, such that regions of the curving flow have differing levels of momentum.

In contrast with Dean flow, the lateral position of the pillar can be used to tune where the net recirculating flows are created across the channel (Figure 3-1C). By moving the sequence of pillars across the channel (in the y-direction) the center of motion follows. This positioning enables spatial control over the induced deformation, for instance by replacing the central pillars (Figure 3-1C.i) with pairs of side half-pillars (Figure 3-1C.v) the direction of the inertial flow deformation is reversed.

The majority of the induced deformation occurs within four pillar diameters of the pillar for our flow conditions, proscribing an effective spacing between pillars for which the transformation from each individual pillar of a sequence behaves independently. Numerical comparison of Stokes and inertial flow development along the channel near the pillar indicates that the presence of the pillars leads to deformation of streamlines and while this deformation possesses fore-aft symmetry in Stokes flow, in agreement with the mirror-symmetry time-reversal theorem (17), the symmetry is broken in the presence of inertia (Figure 3-2A). Upstream, the inertial flow does not diverge greatly compared to Stokes flow. The two flows nearly match at x=0 (i.e. the position of the pillar center), while downstream of the pillar the inertial flow diverges greatly from Stokes flow creating a large deformation compared to the initial fluid topology. This turning motion saturates approximately 3-4 pillar diameters downstream, such that we set an inter-pillar spacing of ten pillar diameters to ensure that when placed in a sequence the downstream flow profile of a previous pillar did not interact with the upstream profile of the next pillar. In this way the transformations performed by each pillar could be sequentially applied, without cross-talk between the independent operations which would require fluid dynamic simulation of the combined sequence.

The relatively uniform behavior of inertial flow deformation over a range of flow rates in finite-Reynolds number laminar flows is an important feature for programming. The Reynolds number is a ratio of inertial to viscous forces in the flow ($Re = \rho UH/\mu$; here, H is the hydraulic diameter of the channel, U is the mean downstream velocity of a fluid with density ρ and viscosity μ). We define σ to measure the magnitude of flow deformation away from the middle of the channel at z=0 (Materials and Methods). σ remains uniform over an order of magnitude of conditions (for Re ~ 6-60 (Figure 3-2B), varying only by a factor of 2-3. Furthermore, while the *net* secondary flows behave consistently over a wide range of flow rates with a single pillar diameter, σ was found to be tunable by adjusting the pillar diameter (Figure S-3-3). A closer examination of flow as a function of Re (Figure 3-2C) reveals that for small channel Reynolds numbers, the flow behaves similar to Stokes flow, with no discernible flow deformation (i. Re=0.08). Other methods to deform flow using structured channels[9] may be complementary for these conditions, however these approaches operate less effectively as Re increases. In contrast, for the cylinders used here, as Re increases significant inertial flow deformation is observed (ii. Re=12). Increasing Re further leads to boundary layer separation along the downstream surface of the pillar and creation of post-pillar wake regions (iii. Re=40) in which the inertial flow deformation starts to manifest more complex behavior (iv. Re=100). In this case, we observe that the fluid parcels near the top of the channel move towards the channel center and that the flow starts to deform away from the channel center further towards the z-midplane. Unexpectedly, the deformation is again directed towards the center at z=0 (Figure 3-2C.iv). These results identify a range of flow conditions required to operate in a single mode but also suggest the ability to make use of separate modes of operation with more complex fundamental transformations over different flow conditions.

Following the identification of this unexpected complexity in the single pillar system, we systematically classified the range of possible flow deformations over the set of practically achievable controlling geometric and flow parameters. Dimensional analysis predicts that the behavior of the system is described using three non-dimensional groups: *Re*, channel aspect ratio *h/w*, and normalized pillar diameter *D/w* (Figure 3-3A). For the case when the flow deformation-inducing obstacle is a cylinder at the center of a straight channel, we uncover four dominant modes of operation for inertial flow deformation (Figure 3-3). The modes are defined based on the number of induced *net* secondary flows in a quarter of the channel (i.e. one or two), as well as the direction of the *net* vorticity axis for each of these flows (Figure 3-3B). Based on our numerical simulations we predict that four additional transitional modes of operation also exist, especially when pillar diameter is small (Figure S-3-4). However, for small *D/w* the *net* rotational flow remains weak (Figure S-3-3), such that these modes are not practically useful.

Inertial flow deformation depends on gradients in fluid momentum and pressure across the channel cross-section that do not identically reverse fore and aft of the pillar. When there are no eddies present behind a pillar the flow deformation occurring in this region dominates over the opposite-directed deformation occurring upstream of the pillar (Figure 3-2A). We observe regions of lower pressure in the middle of the channel (due to the higher velocity fluid in this region) (Figure S-3-5), between two regions of high pressure on the top and bottom of the channel (near y=0). This leads to center-directed motion of fluid parcels from the top and bottom of the channel, which is accompanied by movement of fluid parcels in the middle region to the sides, conserving mass (mode 1). However, increasing *Re* or changes in system geometry (e.g. increasing channel aspect ratio) leads to creation of post-pillar eddies, which form a three-dimensionally complex closed region of recirculation behind the pillar

(Figure S-3-6). This wake causes a reduction in the curvature for fluid streams transiting behind the cylinder and accompanying changes in the pressure field. The combination of these effects reduces the dominance of the deformation occurring downstream of the pillar, shifting the balance to the upstream deformation with net fluid rotation in the opposite direction, which corresponds to alternate modes of operation. Therefore, the motion is further complicated, in ways that we document with experiments and simulations useful for programming, by characteristics of flow past a bluff object which includes the influence of boundary layer separation.

The flow deformation operations we have demonstrated can be integrated to execute sophisticated programs and render complex flow shapes. We can numerically predict the inertial flow deformation near a single pillar with high precision (Figure 3-1C). As discussed, if a set of pillars are appropriately spaced and sequentially placed along a channel, the output of each pillar can be taken as the input for the following pillar and the net deformation produced by the pillars can be combined sequentially. Therefore, by having the transformation function for a limited set of pillar configurations (i.e. pillar size, lateral position), we can predict the total transformation function of any potential program, of which there are an infinite number (Figure 3-4A). Consequently, a user can use a library of pre-simulated motions and place these in series to engineer a flow shape of interest quickly, at a low cost, and with high accuracy without any knowledge of fluid mechanics or numerical simulations. Systematic discretization of the pillar positions, similar to discretization of musical notes, allows abstraction and hierarchical assembly of programs, increasing the ability to engineer complex fluid systems (Figure 3-4B). Therefore, each program is simply communicated using the inlet condition and the sequence of pillar positions (Figure 3-4C). For example, in Figure 3-4A.i an initially straight stream is transformed into a V-shape using

the simple program: *c a b a c.* The variety of attainable shapes include shapes with biconcave and biconvex areas (Figure 3-4C.vii), as well as closed loops (Figure 3-4A.ii), sharp bends (Figure 3-4A.i, iii, iv), added vertices compared to the initial stream, and multiple changes in curvature (Figure 3-4C.i, iii, vi). As a result, analogous to software programming, a user can build upon previously demonstrated functions and integrate them in new ways to create more complex and useful outcomes.

Taking advantage of the programming capabilities, we apply inertial flow deformation to several example applications where lateral migration and manipulation of fluid streams or particles is required. We demonstrate fast and simple extraction of neutrally buoyant particles from a fluid stream (Figure 3-4D) as well as particle separation and sorting by size (Figure 3-4E) which are both useful operations to prepare cellular samples for downstream analysis. In these applications we also simultaneously make use of inertial manipulation of particle streams (11, 16, 21). In this case while 10 μm particles maintain their preferred inertial focusing position, smaller 1 μm particles or dye molecules, which experience weaker inertial lift forces, follow the flow streamlines away from the channel center. More sophisticated programs enable cross-stream translation of a fluid stream and solution exchange around particles in which both the particles and fluid stream stay focused (Figure 3-4F). Inertial flow deformation can also be used to split a single stream at the inlet into two or three streams across the channel, which can be useful in parallelization of screening applications such as flow cytometry (Figure 3-4G). In the previous example, channel expansion allows multiple pillars to simultaneously perform operations on different pieces of the flow stream. Finally, the strong deformations create a semi-helical motion in the flow (for the simplest case of centrally located pillars), which can be used to enhance mixing at high Peclet numbers (Figure 3-4H). In this case full mixing is achieved at high flow rate ($Pe = O(10^5)$) in less than

3 cm. Overall, many of the presented applications are best performed at either high rates to increase throughput, high Reynolds numbers to allow compatibility with inertial control of particles, or high Peclet numbers to prevent diffusive blurring of a sculpted material shape, such that the current approach that operates effectively outside of a Stokes flow regime is ideal.

The ability to program fluid flows in channels – particularly controlling cross-sectional shape and rotating and moving fluid streams – introduces a fundamental new capability potentially useful in a variety of other applications. (i) Controlling the cross-sectional shape of a monomer stream enables manufacture of new classes of polymerized fibers with engineered interactions (e.g. interlocking or self-assembling fiber materials) (8, 22-26). By combining this cross-sectional shape control of a polymer pre-cursor stream with optical patterning transverse to the flow direction (6,7) fabrication of an infinite set of truly 3D particle shapes would be possible. Additionally, programming a variety of cross-sectional lens shapes with a fluid of separate index of refraction (27) can be of use for opto-fluidic control and sensing (28). (ii) Rotating or moving fluid streams to be analyzed away from walls to regions of uniform downstream velocity at the channel center can minimize Taylor dispersion[9], bring fluid into a small focal spot for optical interrogation (29, 30) or reduce fouling and adhesion to channel surfaces. Conversely, bringing fluid to narrow slow moving regions near channel walls can enhance surface reactions (e.g. immunoassays (31), or aid in affinity capture of cells (32) or molecules. Additionally, utilizing this platform to deterministically guide liquid in microchannels can enhance heat transfer, especially in electronic cooling, by maximizing the efficiency of coolant usage near hot spots and enabling the usage of larger channels with lower pressure drops and power consumption in these systems (33-35). We anticipate these future applications will be enabled as the complexity of available functions increases. An

exponential growth in program complexity with time could be expected, as for computational programming, because no expert knowledge of hardware is needed and operations are abstracted and hierarchically assembled in an easily communicated form.

Materials and Methods

Microfabrication. Microfluidic devices were fabricated using polydimethylsiloxane (PDMS) replica molding processes (36). Briefly, standard lithographic techniques were used to produce a mold from a silicon master spin-coated with SU-8 photoresist (MicroChem Corp.). PDMS chips were produced from this mold using Sylgard 184 Elastomer Kit (Dow Corning Corporation). Inlet and outlet holes were punched through PDMS using a pin vise (Technical Innovations, Inc.). PDMS and glass were activated by air plasma (Plasma Cleaner, Harrick Plasma) and bonded together to enclose the channels. In order to see the PDMS walls of the channel (Figure 3-1B) Rhodamine B red dye, which permeates PDMS, was infused into the channel and washed prior to the experiments.

Dye and bead suspensions. To help visualization, the fluid stream was mixed with FITC Dextran 500kDa (4 μM in deionized water) or with blue food dye. Fluorescent monodisperse particles (1 μm and 10 μm, 1.05 g/ml) were purchased from Duke Scientific. Particles were mixed in deionized water. Fluid streams and particle suspensions were pumped into the devices through PEEK tubing (Upchurch Scientific Product No. 1569) using a syringe pump (Harvard Apparatus PHD 2000).

Imaging. Confocal imaging was performed at the California NanoSystems Institute (CNSI) using a Leica inverted SP1 confocal microscope. Confocal images are the average of 8 y-z scans. Fluorescent images were recorded using a Photometrics CoolSNAP HQ2 CCD camera mounted on a Nikon Eclipse Ti microscope. Images were captured with Nikon NIS-Elements AR 3.0 software. For high-precision observations and measurements, high-speed images were also recorded using a Phantom v7.3 high-speed camera (Vision Research Inc.) and Phantom Camera Control software.

Numerical simulations for phase diagram. The numerical simulations were performed using an in-house, parallel framework based on stabilized finite element (FEM) methods. The phase-diagram was built by performing more than 2200 of these numerical simulations with different configurations. This was automated using a novel fault tolerant strategy that deployed the FEM framework across high performance computing clusters (NSF XSEDE: Ranger system and Iowa State: Cystorm system).

Definition of σ. In order to quantitatively compare the amount of lateral fluid motion for different flow and geometric conditions we define a normalized value, σ. It is defined as the mean of the net lateral velocities (SI Text 1) at z=0 (middle-height of the channel), normalized by the average downstream velocity of the main flow, in other words $\sigma \equiv \left(\left(V_y\right)_{mean}\right)_{z=0} \Big/ \left(V_x\right)_{avg}$. This is essentially a measure of the distance fluid has moved laterally (on average and at the channel mid-plane) per unit of length it travels downstream.

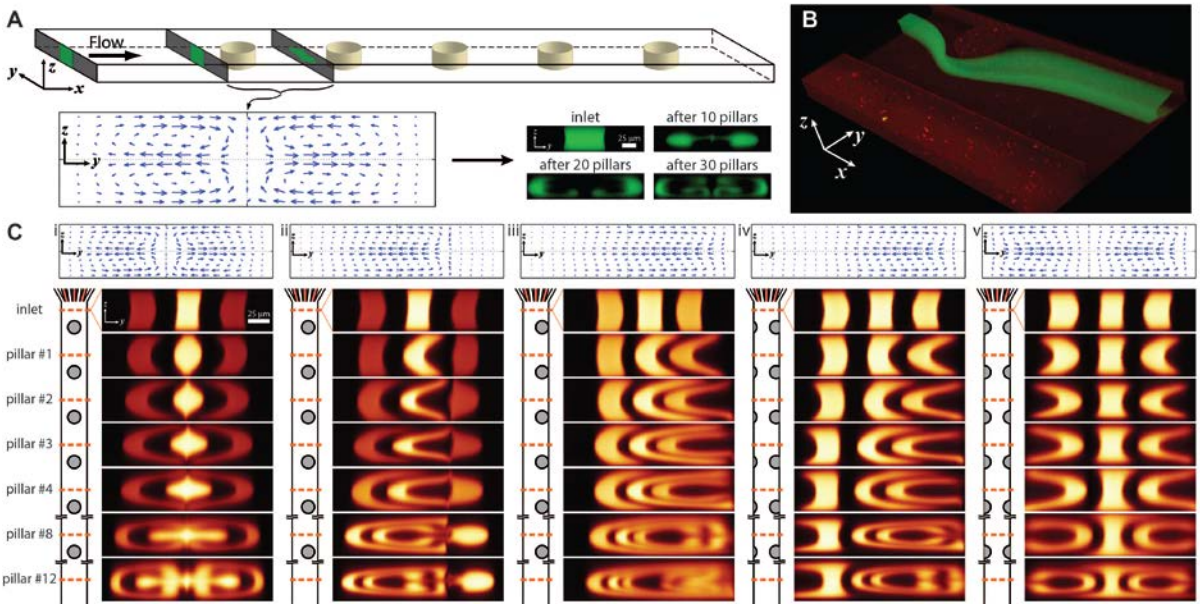

Figure 3-1. Local inertial flow deformation induced by microstructures. A. Flow passing a microstructure deforms significantly creating a *net* recirculating secondary flow in the channel. The arrow plot shows the average lateral velocity field as fluid parcels travel from input cross-section (upstream) to output cross-section (downstream). The numerical prediction is confirmed experimentally. B. A 3D confocal microscopy image of a fluorescent stream deforming around a single pillar in the channel clearly shows how the stream of fluid (sandwiched between two streams of unlabeled fluid) is irreversibly twisted losing fore-aft symmetry around the pillar. The PDMS surface of the channel is labeled red for a more vivid observation. C. Position of the net circulation is controlled by pillar location. The top row shows the net deformation arrow plots for different pillar locations as predicted by numerical simulations. Below are the confocal images of channel cross-sections for each of the sequenced configurations. The lateral placement of pillar sequences is shown in the schematic. Three labeled streams are tracked for a more detailed observation. By displacing the pillar center from the middle to the side of the channel (from i to v), the lateral position of the net recirculating flow is similarly displaced.

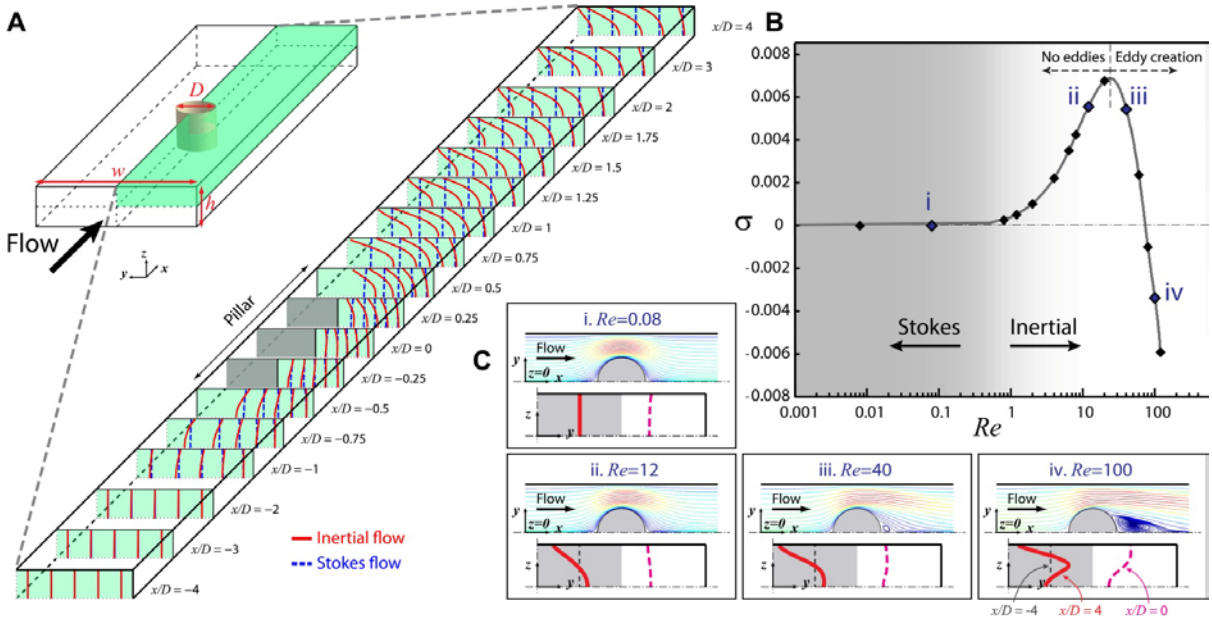

Figure 3-2. Development of inertial flow deformation and operating regime. A. Comparison of Stokes and inertial flow development along the channel near the pillar (shown in the top-right quarter of the channel). In each cross-section, using numerical simulations, we follow five vertical lines of tracer fluid parcels as they move past the obstacle and reach a stable state. The fore-aft symmetry of deformation that exists in Stokes flow is broken in the presence of inertia. B. The graph shows σ, a measure of flow deformation away from the middle of the channel at z=0 over a wide range of *Re*. C. A more detailed simulation of a vertical set of inlet streamlines and their deformation in a quarter of the channel is provided for four different *Re*. The top-view of streamlines at z=0 reveals the creation of post-pillar eddies with increasing *Re* which corresponds to the shift from increasing to decreasing σ with *Re*. The front view illustrates the outline of an initially vertical line of fluid parcels at the inlet (dashed grey line), traced at x=0 (dashed pink line) and the outlet (solid red line). Solid black lines show channel walls and the dash-dot black lines indicate channel symmetry. The grey area shows the outline of a quarter of the pillar in the respective channel quarter.

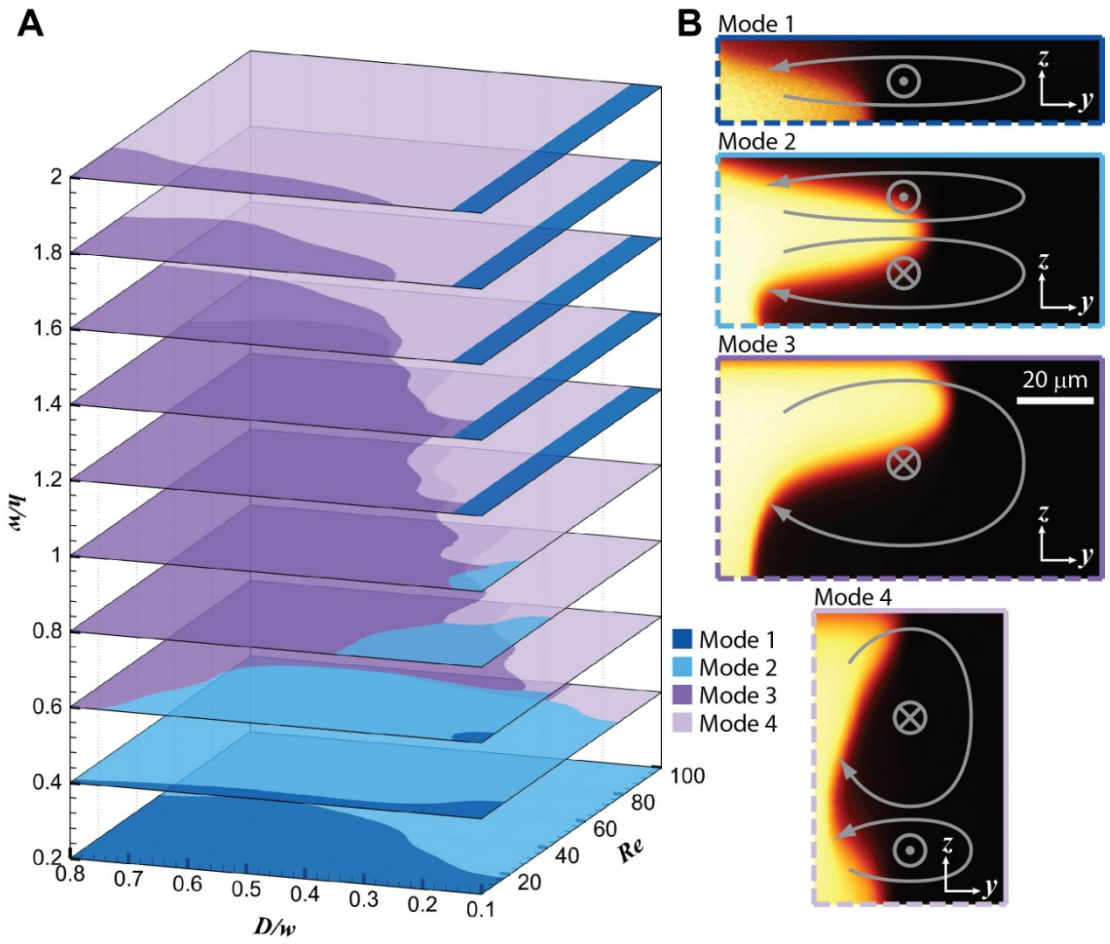

Figure 3-3. Phase diagram for inertial flow deformation. A. For the simplified case when the deformation-inducing obstacle is a cylindrical pillar at the center of a straight channel, there are four dominant modes of operation. This phase diagram shows which mode is in effect at any given set of flow conditions and geometric parameters. B. The four modes of operation achieved experimentally are shown with confocal cross-sections of the asymmetric quadrant of the flow (same scale bar is used for all four images). The images are overlaid with arrows indicating the direction of motion for that mode of operation.

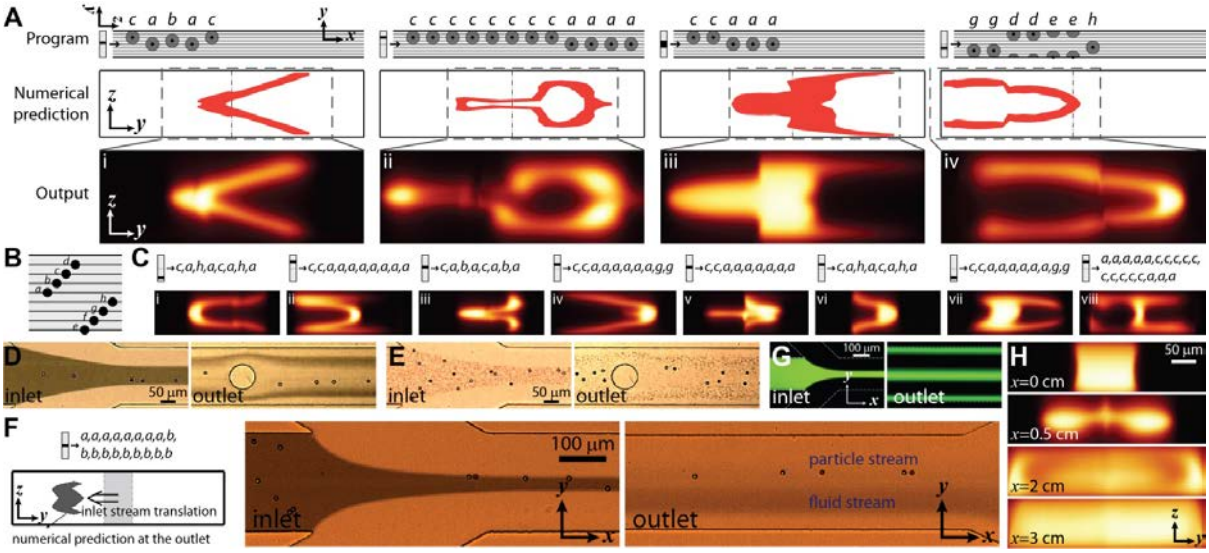

Figure 3-4. Engineering fluid flow using programmed sequences of pillars and enabled applications. A. Accurate numerical prediction of inertial flow deformation allows programming the cross-section of the flow. Each program consists of 1) a sequence of pillars positioned at different locations across the channel, and 2) an initial condition, i.e. inlet position and width of the fluid stream. The numerical predictions based on sequencing operations from a library of single-pillar flow transformation maps match very well with the experimental results. A user can use a library of pre-simulated motions and place these in series to engineer a flow shape of interest. B. The systematic discretization of the pillar positions, similar to discretization of musical notes, facilitates the communication and reproducibility of different designs. C. Demonstration of a variety of cross-sectional flow patterns created using simple programs. The images show the wide range of interesting shapes that can be created using the simplest form of programming, using only different pillar positions while maintaining the channel geometry, pillar shape and size, and flow conditions. D. Extraction of particles from a fluid stream. While the fluid moves away from the channel center due to inertial effects, particles are maintained at the channel centerline due to inertial focusing. E. Separation of particles by size using a similar geometry (10 μm particles remain focused while 1 μm particles follow fluid streams). F. Moving fluid streams and solution exchange. G. Stream splitting. H. Microfluidic mixing.

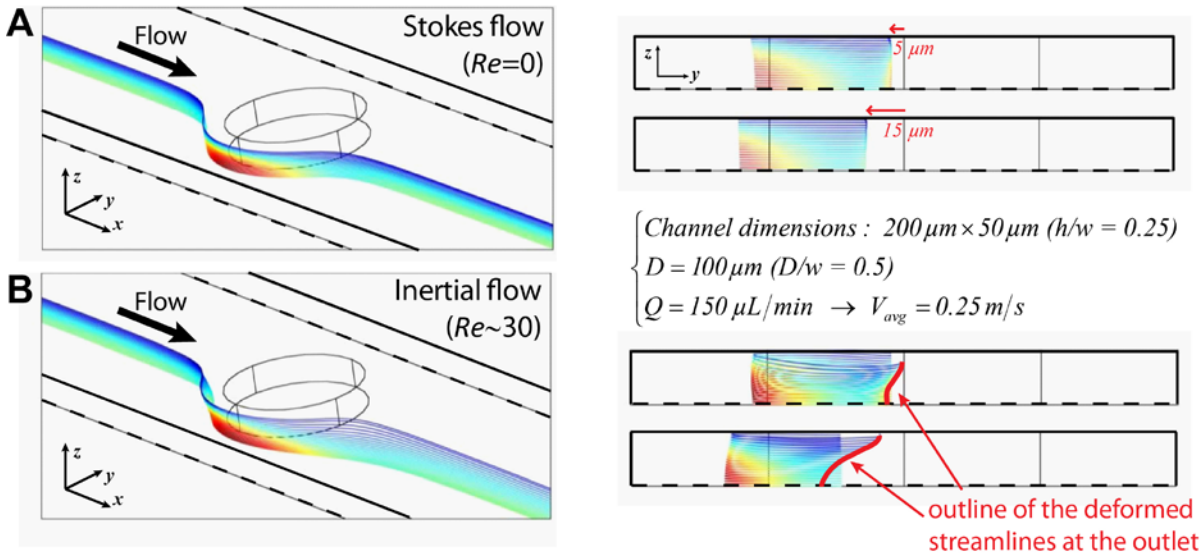

Figure S-3-1. Qualitative differences between Stokes and inertial flow around an obstacle. (A) In Stokes flow the set of streamlines (starting at the same y-position at the inlet) is diverted around the obstacle (left). The fore-aft symmetry of this curved motion requires the streamlines to return to their initial lateral position near the outlet, as can be observed in the front view for two sets of streamlines that are 5 μm and 15 μm offset from the channel centerline (right). (B) The inertial flow, however, acts noticeably different (left). In this case, the streamlines do not return symmetrically downstream but relocate to a new stable position in the y-z plane (right). These simulations are conducted in the top-half of the channel due to symmetry (channel symmetry lines are dashed).

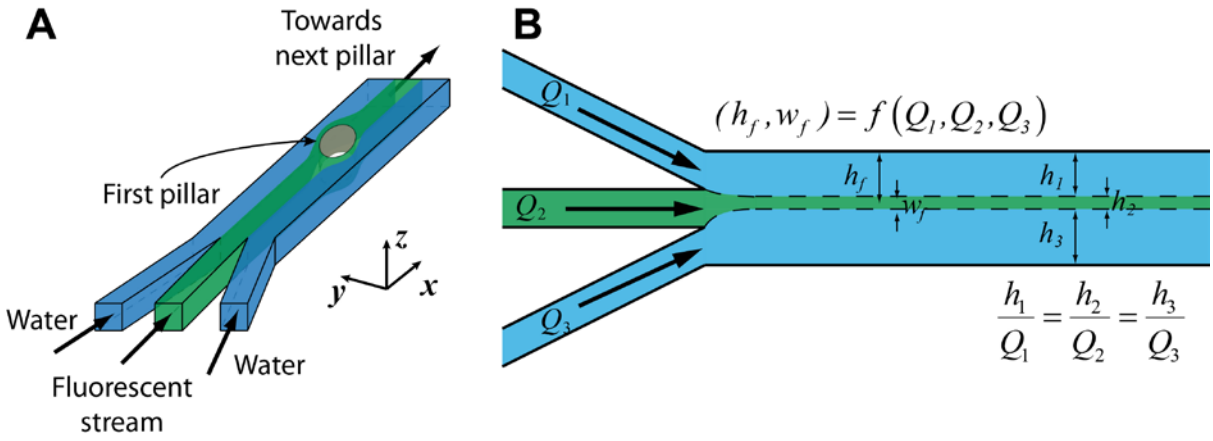

Figure S-3-2. Simplified schematic of the experimental device. (A) Fluorescent and non-fluorescent streams of water are injected through multiple inlets into a straight channel that contains a sequence of obstacles. The cross-sectional shape of the fluorescent stream is imaged after each pillar using confocal microscopy. (B) The width and position of the fluorescent stream at the inlet can be determined by adjusting the inlet flow rates.

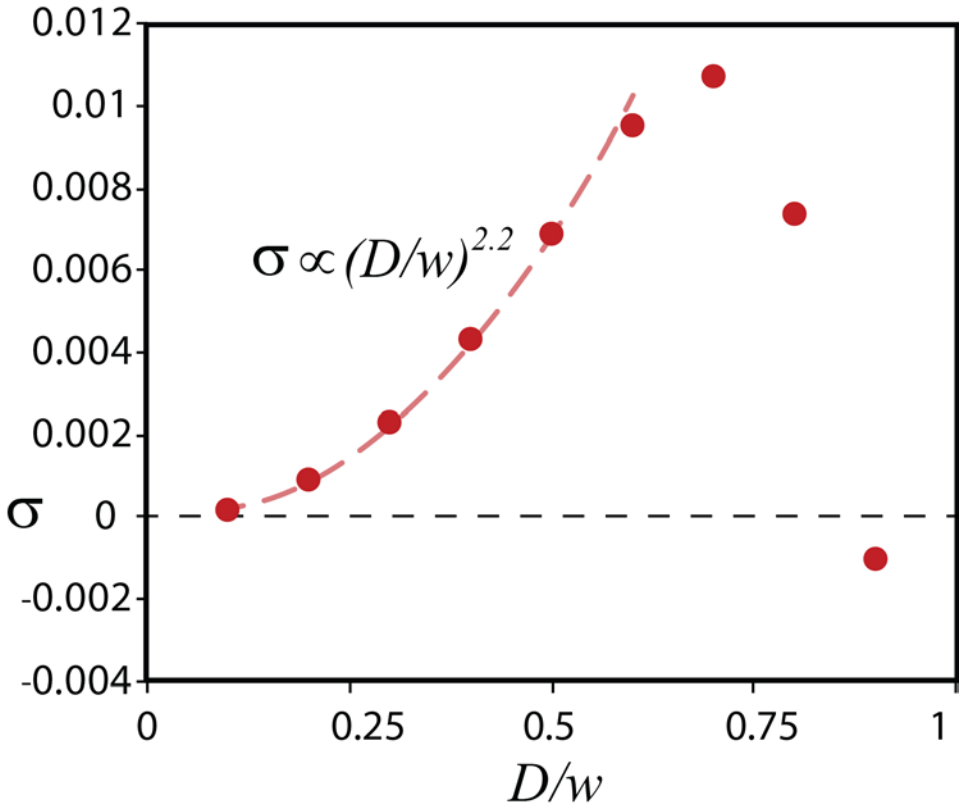

Figure S-3-3. Dependence of σ on *D/w*. When the normalized pillar diameter is smaller than 0.75 and no post-pillar eddies are created, σ can be directly interpreted as the amount of normalized fluid motion in the channel. *Re* for the flow is ~30. It is clear in this range that σ has a very strong dependence on pillar diameter such that by changing *D/w* from 0.25 to 0.75, σ increases by more than an order of magnitude. This means that pillar diameter can be used as an effective tool in tuning the strength of the secondary flow created. However, it should be noted that at the same flow conditions and by only using larger pillars (e.g. *D/w* > 0.8 in this case) we can also introduce new modes of operation into the system.

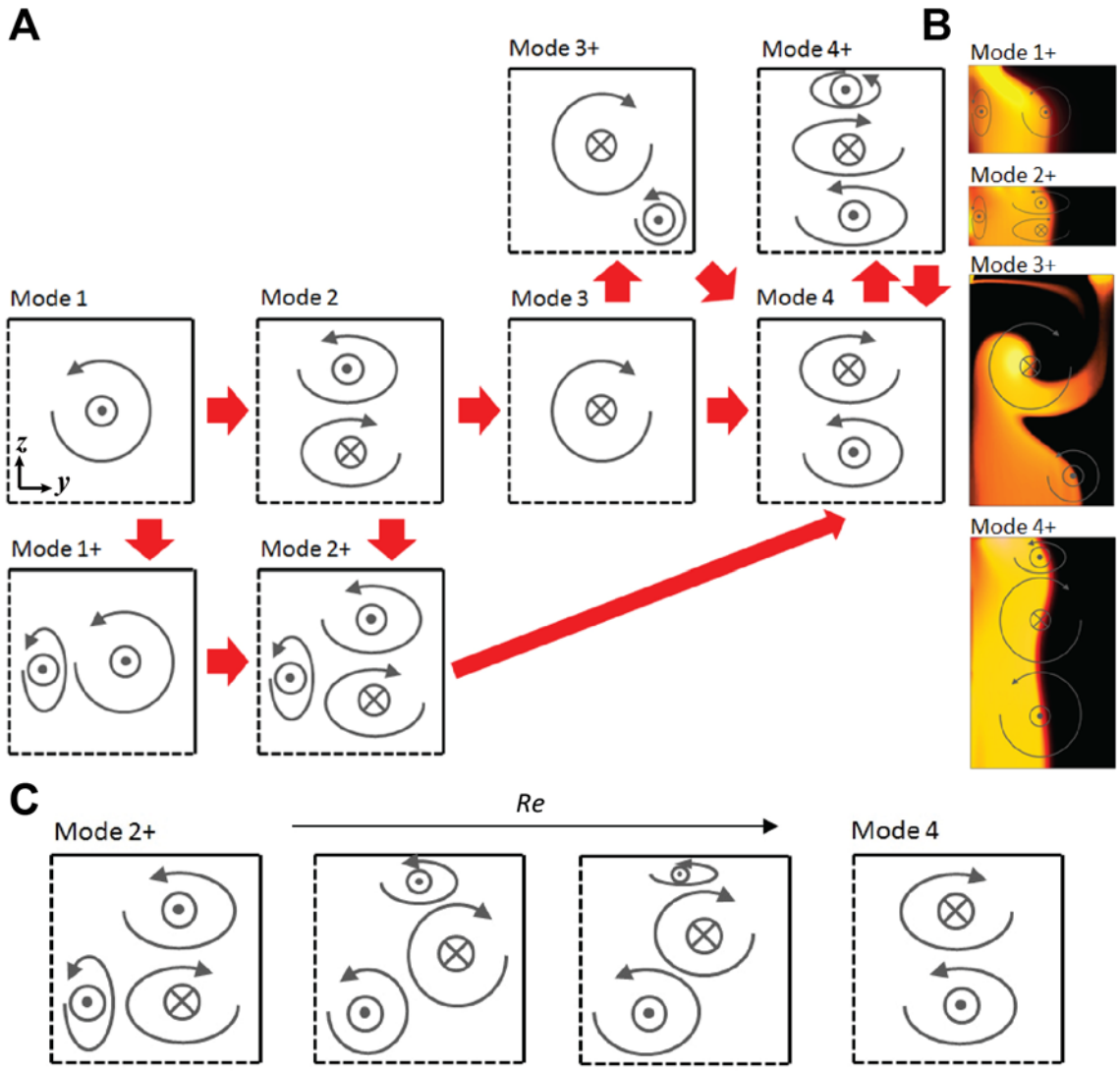

Figure S-3-4. Dominant and auxiliary modes of operation showcasing the transition between modes (A) Schematic of all of the possible modes of operation with transition pathways between them are depicted in red. Modes 1-4 are the dominant modes which have also been experimentally observed. It is possible to transition from one dominant mode to the next dominant mode by only increasing the Reynolds number while the geometry of the channel is fixed (i.e. fixed diameter *D/w* and channel height *h/w* while increasing flow velocity). Numerical simulations suggest that there exist four additional modes of operation. These additional modes are characterized by the appearance of an additional, auxiliary rotational flow deformation within each of the main modes (and are consequently named as "+ modes"). However, these "+ modes" either exist in a narrow range of configurations (small *D/w* or narrow extent of *Re*) bridging main modes, or have an auxiliary deformation with significantly smaller magnitude (compared to the main deformations) resulting in a limited effect on the tracing of fluid parcels. Consequently, we merge the "+ modes" with their corresponding dominant modes in representing the phase diagram in Figure 3-3. In all of these cases the obstacle is a cylindrical pillar, located at the center of the channel. Note that the two axes of symmetry allow us to show all deformations in the first quadrant. The channel sizes and aspect ratios are not to scale in the schematic drawings. (B) Depiction of the numerical realizations of dye evolution under the auxiliary modes of operation in the first

quadrant of the channel. Numerical simulations are used to regenerate the evolution of a dye stream in flow conditions of "+ modes", replicating the confocal images of Figure 3-3.B which were experimentally obtained for the dominant modes. (C) We illustrate a detailed transition process between mode 2+ and mode 4 to showcase how one mode transitions to another with increasing Reynolds number. For an initial increase in *Re*, the strength and range of the auxiliary deformation in mode 2+ extends, which weakens the rotational region on top of the channel at the same time. With further increase in *Re*, this auxiliary deformation region grows larger and tends to dominate the lower half (of the first quadrant) of the channel. This process continues until the top rotational flow dissipates and the flow mode turns from mode 2+ to mode 4. Moreover, this transition occurs over a very narrow change of *Re*, emphasizing the transitional nature of the + modes.

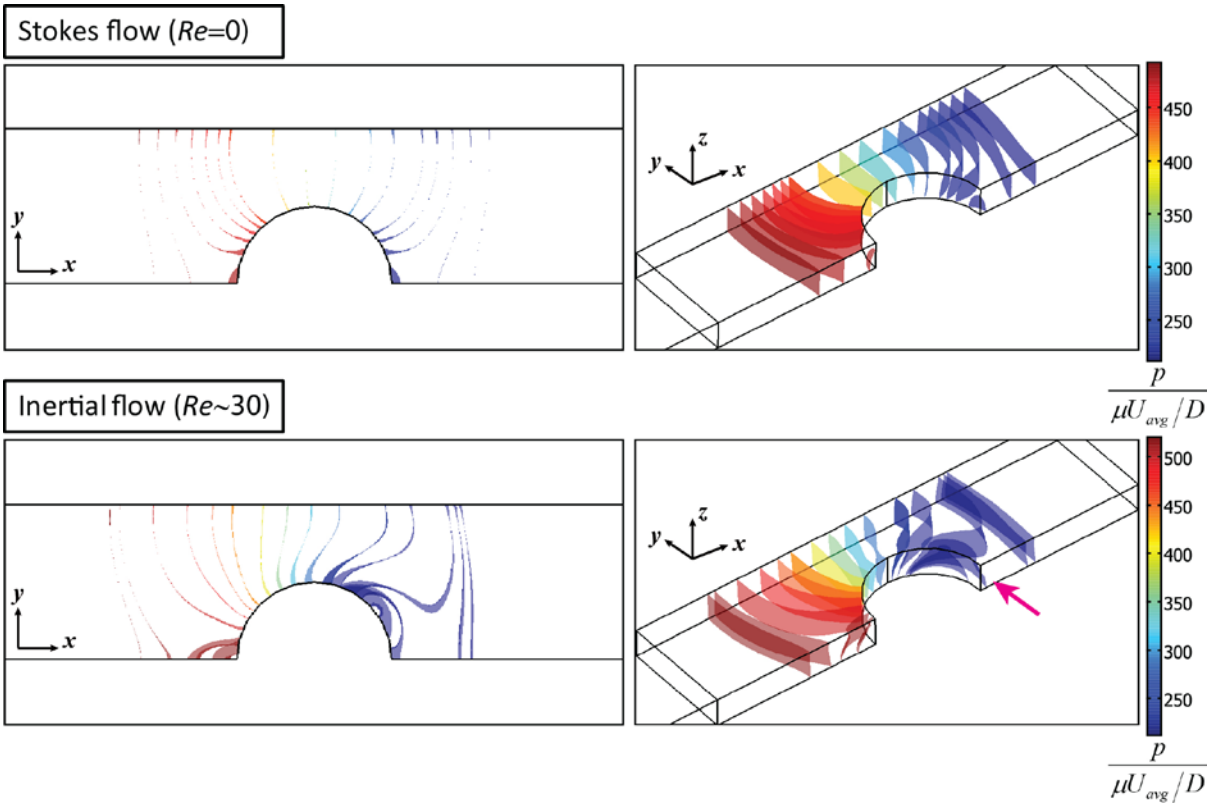

Figure S-3-5. Normalized pressure distribution in Stokes and inertial flow around an obstacle (shown in the top-half of the channel). The shape and form of isobaric surfaces around the pillar shows that the pressure distribution is symmetric near the pillar in Stokes flow, as expected. However, the presence of inertia deforms these surfaces significantly due to convection of vorticity downstream. This generates a complex pressure distribution in the channel such that a low pressure region is created near the channel center behind the pillar which allows fluid to move towards the center from the higher-pressure regions near the top and bottom of the channel (arrows). Consequently, and to conserve mass, fluid parcels move outward from the middle of the channel producing the *net* rotational flow.

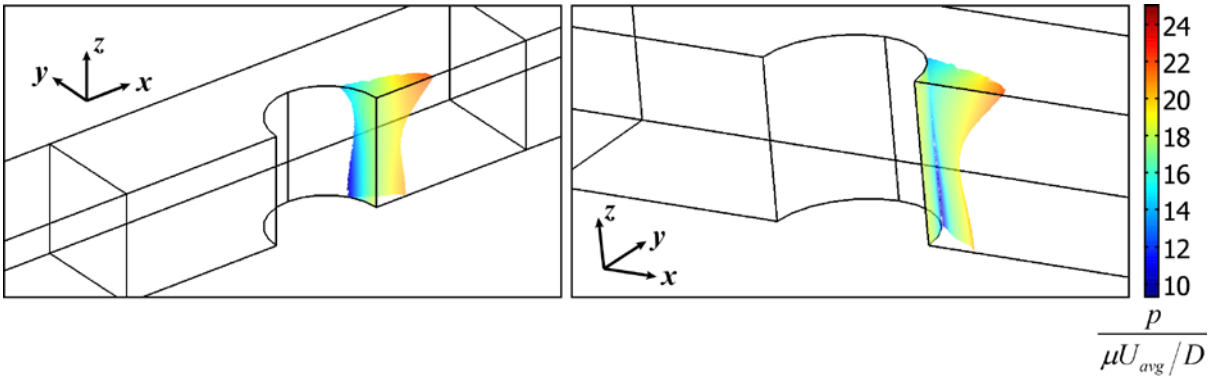

Figure S-3-6. Morphology of the separatrix that is formed by eddies behind the pillar (shown in a quarter of the channel). The creation of a complex surface behind the pillar that is impermeable to the streamlines passing the pillar modifies the region that streamlines can effectively occupy and the accompanying pressure field. *Re* for the flow is ~80. These variations greatly affect the flow deformation process such that the creation of these complex surfaces, driven by boundary layer separation in a confined channel, is expected to be a main cause of different operational modes.

SI Text 1. Lateral velocity field arrow plot creation. The arrow plots show the *net* rotational flow that is occurring near a pillar, which means that it is extracted by the comparison of the lateral position of fluid parcels between inlet and outlet. Each arrow indicates the *net lateral velocity* at that position in the channel cross-section. “Net lateral velocity” is defined for each fluid parcel as the average lateral velocity of the fluid parcel as it travels downstream, from the inlet to the outlet. It is numerically calculated by dividing the total lateral displacement of a fluid parcel (that has traveled from inlet to the outlet) by the total time taken for this motion to occur.

Bibliography

1. Sudarsan, A P, Ugaz, V M (2006) Multivortex micromixing. *Proc. Natl. Acad. Sci.* 103 (19): 7228-7233.

2. Wang J, Zhan Y, Ugaz V M, Lu C (2010) Vortex-assisted DNA delivery. *Lab Chip* 10: 2057-2061.

3. Toner M, Irimia, D (2005) Blood-on-a-chip. *Annu. Rev. Biomed. Eng.* 7: 77-103.

4. Gambin Y et al. (2011) Visualizing a one-way protein encounter complex by ultrafast single-molecule mixing. *Nature Methods* 8 (3): 239-244.

5. Günther A, Jensen K (2006) Multiphase microfluidics: from flow characteristics to chemical and materials synthesis. *Lab Chip* 6: 1487-1503.

6. Pregibon D C, Toner M, Doyle P S (2007) Multifunctional encoded particles for high-throughput biomolecule analysis. *Science* 315: 1393-1396.

7. Lee H, Kim J, Kim H., Kim J, Kwon S (2010) Colour-barcoded magnetic microparticles for multiplexed bioassays. *Nature Materials* 9: 745-749.

8. Thangawang A L, Howell P B, Spillmann C M, Naciri J, Ligler F S (2011) UV polymerization of hydrodynamically shaped fibers. *Lab Chip* 11: 1157-1160.

9. Stroock A D et al. (2002) Chaotic mixer for microchannels. *Science* 295: 647-651.

10. Ottino J M, Wiggins S (2004) Designing optimal micromixers. *Science* 305: 485-486.

11. Di Carlo D, Irimia D, Tompkins R G, Toner M (2007) Continuous inertial focusing, ordering, and separation of particles in micrrochannels. *Proc. Natl. Acad. Sci.* 104(48): 18892-18897.

12. Lee W, Amini H, Stone H A, Di Carlo D (2010) Dynamic self-assembly and control of microfluidic particle crystals. *Proc. Natl. Acad. Sci.* 107(52): 22413-22418.

13. Ottino J M et al. (1992) Chaos, symmetry, and self-similarity: exploiting order and disorder in mixing processes. *Science* 257: 754-760.

14. Stremler M A, Haselton F R, Aref H (2004) Designing for chaos: applications of chaotic advection at the microscale. *Phil. Trans. R. Soc. Lond. A* 362: 1019-1036.

15. Liu R H et al. (2000) Passive mixing in a three-dimensional serpentine microchannel. *Journal of Microelectromech. Syst.* 9: 2, 190-197.

16. Di Carlo D (2009) Inertial microfluidics. *Lab Chip* 9: 3038-3046.

17. Bretherton F P (1962) The motion of rigid particles in a shear flow at low Reynolds number. *Journal of Fluid Mech.* 14: 284-304.

18. Lauga E, Stroock A D, Stone H A (2004) Three-dimensional flows in slowly varying planar geometries. *Phys. Fluids* 16: 8, 3051-3062.

19. Dean W R (1928) Fluid motion in a curved channel. *Proc. of the Royal Society of London Series A* 121(787): 402-420.

20. Berger S A, Talbot L (1983) Flow in curved pipes. *Ann. Rev. Fluid Mech.* 15: 461-512.

21. Hur S C, Tse H T K, Di Carlo D (2010) Sheathless inertial cell ordering for extreme throughput flow cytometry. *Lab Chip* 10: 274-280.

22. Jeong W et al. (2004) Hydrodynamic microfabrication via "on the fly" photopolymerisation of microscale fibers and tubes. *Lab Chip* 4: 576-580.

23. Hwang C M, Khademhosseini A, Park Y, Sun K, Lee S H (2008) Microfluidic chip-based fabrication of PLGA microfiber scaffolds for tissue engineering. *Langmuir* 24: 6845-6851.

24. Chung B G, Lee K H, Khademhosseini A, Lee S H (2012) Microfluidic fabrication of microengineered hydrogels and their application in tissue engineering. *Lab Chip* 12: 45-59.

25. Choi C H, Yi H, Hwang S, Weitz D A, Lee C S (2011) Microfluidic fabrication of complex-shaped microfibers by liquid template-aided multiphase microflow. *Lab Chip* 11: 1477-1483.

26. Nunes J K, Sadlej K, Tam J I, Stone H A (2012) Control of the length of microfibers. *Lab Chip* 12: 2301-2304.

27. Mao X, Waldeisen J R, Juluri B K, Huang T J (2007) Hydrodynamically tunable optofluidic cylindrical microlens. *Lab Chip* 7: 1303-1308.

28. Erickson D, Mandal S, Yang A H J, Cordovez B (2008) Nanobiosensors: optofluidic, electrical and mechanical approaches to biomolecular detection at the nanoscale. *Microfluid Nanofluid* 4: 33-52.

29. Howell P B et al. (2008) Two simple and rugged designs for creating microfluidic sheath flow. *Lab Chip* 8: 1097-1103.

30. Golden J P et al. (2009) Multi-wavelength microflow cytometer using groove-generated sheath flow. *Lab Chip* 9: 1942-1950.

31. Squires T M, Messinger R J, Manalis S R (2008) Making it stick: convection, reaction and diffusion in surface-based biosensors. *Nature Biotech.* 26: 417-426.

32. Stott S L et al. (2010) Isolation of circulating tumor cells using a microvortex-generating herringbone-chip. *Proc. Natl. Acad. Sci.* 107(43): 18392-18397.

33. Agostini B et al. (2007) State of the art of high heat flux cooling technologies. *Heat Transfer Engineering* 28(4): 258-281.

34. Ebadian M A, Lin C X (2011) A review of high-heat-flux heat removal technologies. *Journal of Heat Transfer* 133: 110801-11.

35. Kandlikar S G (2012) History, advances, and challenges in liquid flow and flow boiling heat transfer in microchannels: a critical review. *Journal of Heat Transfer* 134: 034001-15.

36. Sollier E, Murray C, Maoddi P, Di Carlo D (2011) Rapid prototyping polymers for microfluidic devices and high pressure injections. *Lab Chip* 11: 3752-3765.